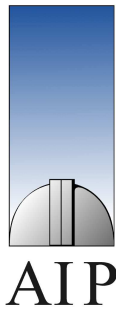


*Analysis of multi-wavelength Hubble Space Telescope
observations of circumstellar disks in the Orion Nebula*



Artist's depiction of a circumstellar disk. Thousands of planetesimals roam around a new-born star. A few objects have already grown to much larger sizes—they are planets in the making. (Image credit: Pat Rawlings, Jet Propulsion Laboratory)



Analysis of multi-wavelength Hubble Space Telescope observations of circumstellar disks in the Orion Nebula

A Diploma thesis presented to
the Institute of Physics at the University of Potsdam

Written at the
Astrophysikalisches Institut Potsdam

by

Jens Rodmann

Contents

Introduction	1
1 From disks to planets	3
1.1 A case study: the solar system	3
1.1.1 Planetary orbits	4
1.1.2 Mass and angular momentum distribution	7
1.1.3 Element abundances	9
1.2 Star formation: an overview	12
1.2.1 The physics towards a star	12
1.2.2 Spectral energy distribution classification	16
1.3 Circumstellar disks	21
1.3.1 Disk accretion and angular momentum transport	21
1.3.2 Detection and observation	23
1.3.3 Physical properties	24
1.4 Planetesimal and planet formation	27
1.4.1 Assembly of large aggregates from dust grains	28
1.4.2 Planet formation	29
2 The Hubble Space Telescope	31
2.1 Wide Field and Planetary Camera 2	32
2.2 Space Telescope Imaging Spectrograph	33
2.3 Near Infrared Camera and Multi-Object Spectrograph	34
2.4 Filter elements used	35
3 Data: reduction and analysis	37
3.1 Data stock	37
3.2 Data reduction	38
3.2.1 Cosmic ray removal	38
3.2.2 Image dithering	39
3.2.3 PSF deconvolution	40
3.3 Data analysis	43
3.3.1 Search for new silhouette disks	43
3.3.2 Measurement of disk sizes	45
3.3.3 Intensity profiles at different wavelengths	45
3.3.4 <i>JHK</i> photometry	53

4 Results	55
4.1 Disk size distributions	55
4.2 Wavelength-dependence of disk size	59
Bibliography	63
List of figures	69
List of tables	71

Introduction

Circumstellar disks are believed to be the birthplaces of planets. Being remnants of the formation of stars, they are composed of gas and dust. The latter constitutes the pristine material out of which planetary bodies are made. Theory depicts a two-stage process: In the first, submicrometre-sized dust grains frequently collide in a turbulent disk. Depending on their relative velocity, they might stick to one another by cohesive forces to form larger aggregates. This process continues to build up kilometre-sized planetesimals—the building blocks of (rocky) planets. In the second stage, larger objects are formed by gravitational attraction between the planetesimals. Eventually planetary bodies come into existence.

Unfortunately, observational vindications of this picture are still missing. As one part of this thesis we will try to answer the question whether or not dust grains are growing in circumstellar disks. For this purpose, *Hubble Space Telescope* observations of circumstellar disks in the Trapezium Cluster, the dense core of the Orion Nebula, are analysed. Measurements of disk diameters at different wavelengths (from near-ultraviolet to near-infrared) can give constraints on the size of circumstellar dust grains. For submicrometre dust particles, the apparent size of a disk will be smaller at longer wavelengths because of reduced extinction. A wavelength-independent size, on the other hand, suggests the presence of significantly larger aggregates.

A second focal point of this thesis are the impacts environmental conditions in young stellar clusters have on circumstellar disks. The fact that most stars are born in clusters exposes circumstellar disks to many unfavourable conditions. Several ambient processes remove gas and dust from circumstellar disks, thereby counteracting planetesimal growth. Neighbouring OB stars are powerful sources for ultraviolet radiation which can ionise and evaporate disks of other nearby stars. Close encounters with other cluster members and subsequent tidal interactions distort, truncate, or even disrupt circumstellar disks. Disk size distributions can help to understand the harsh conditions in young, dense clusters, and to assess their influences on the evolution of circumstellar disks.

To summarise, the aim of this thesis is to find first answers to the prime question whether *circumstellar* disks in young stellar clusters can be rightfully assigned to be *protoplanetary*, i. e. “cradles” of growing planets.

Chapter 1

From disks to planets

*Do there exist many worlds, or is there but a single world?
This is one of the most noble and exalted questions in the study of Nature.*

ALBERTUS MAGNUS, 13th century

1.1 A case study: the solar system

While it is always hazardous—some may argue futile—to ground theories on only one specimen, a great many insights can still be gained in examining that very example. Any generalisation, however, requires due caution. Bearing that caveat in mind, we embark on a description of planet formation by investigating the global properties and characteristics of the solar system. Some of these are prototypical in nature. Just a short while ago, the sample of known planetary systems was extremely small. Only one was known to exist—our own solar system. Its confines may be defined differently, either as the region dominated gravitationally by the Sun or as the volume filled by its magnetic field. At any rate, the solar system is governed by the Sun, an ordinary main sequence star of spectral class G2V, and extends to approximately 10^5 AU, or roughly half a parsec*. Besides the central star, many other celestial bodies populate the solar system; the most relevant of them within the innermost 50 AU radius. They differ strongly in mass, size and chemical composition; hence they are classified distinctly from one another. The largest and most massive of these bodies are the planets orbiting the Sun: four giant, gaseous bodies, four smaller, Earth-like ones and one which cannot be assigned to either group. With the exception of the two innermost planets (Mercury and Venus), all planets possess satellites or moons, as they are generally called; some of which are comparable in size to the smaller planets. Furthermore, thousands of asteroids roam between the orbits of Mars and Jupiter. Their diameters range from a few tens to some hundreds of kilometres. Dark and icy, we find the Kuiper Belt objects (KBOs) beyond Neptune's orbit. The Oort Cloud, a vast reservoir of cometary nuclei, limits the solar system gravitationally.

*Proxima Centauri, the faintest member of the α Cen triple system and the nearest star from the Sun, lies at a distance of 1.32 pc.

We will not attempt to treat all the facts and details of the solar system comprehensively. Rather, we limit ourselves to a small subset of them, chosen in view of depicting the grand picture. As a beginning, let us have a closer look at the orbital parameters and physical characteristics of the solar system planets as gathered in Table 1.1.

Table 1.1. Orbital parameters and physical characteristics of the planets

Planet	Semi-major axis [AU]	Eccentricity	Inclination to the ecliptic	Mass [M_E] ^a	Equatorial diameter [km]	Mean density [g cm^{-3}]
Mercury	0.3871	0.206	7°00′	0.055	4878	5.44
Venus	0.7233	0.007	3°24′	0.815	12 104	5.25
Earth	1	0.017	0°	1	12 756	5.52
Mars	1.5237	0.093	1°51′	0.107	6794	3.94
Jupiter	5.2026	0.048	1°19′	317.80	142 800	1.24
Saturn	9.5547	0.056	2°30′	95.1	120 000	0.63
Uranus	19.2181	0.046	0°46′	14.6	50 800	1.21
Neptune	30.1096	0.009	1°47′	17.2	48 600	1.67
Pluto	39.4387	0.246	17°10′	0.002	2300	1.1 ^b

(a) $1 M_E \simeq 1/330\,000 M_\odot$, (b) Taken from Tholen & Buie (1997)
SOURCE: Data compiled from Encrenaz et al. (1995)

1.1.1 Planetary orbits

Spacings Proceeding columnwise, we start with the distances of the planets to the Sun. The numbers cover two orders of magnitude; from approximately 0.4 AU for Mercury to around 40 AU in the case of Pluto. The planets are well isolated, that is to say, that from a planet of given distance to the Sun any neighbouring planets are separated by distances of the same order of magnitude, not significantly closer. In the 18th century, Titius (1729–1796) discovered that the heliocentric distances of the then known planets (Mercury to Saturn) follow a geometric progression, provided a missing planet is placed between the orbits of Mars and Jupiter. Propagated by Bode (1747–1826), this empirical relation is known as the Titius-Bode law and reads as $r_n = 0.4 + 0.3 \times 2^n$, where the planet’s distance to the Sun r_n is expressed in astronomical units (AU). The exponent n takes values from $n = -\infty$ for Mercury, $n = 0$ for Venus, $n = 1$ for the Earth, and so on in integer steps. The arcane missing planet is assigned $n = 3$, and indeed one finds the asteroid belt around the predicted position. The “law” yields good approximations up to Uranus ($n = 6$), the corresponding errors being below 5%. For Neptune and Pluto, however, the deviations become significant, reaching 29% and 96%, respectively (cf. Figure 1.1).

This clearly shows the limitations of the Titius-Bode relation. Hénon (1969) and Lecar (1973) have demonstrated that any random set of orbits easily satisfies a Titius-Bode type relation if the only constraint holds that adjacent planets should not be too close. This “excluded volume” principle gives a first hint that during their formation the planets were engaged in a sort of “sibling rivalry”. The commodity they competed for was matter from a circumstellar disk.

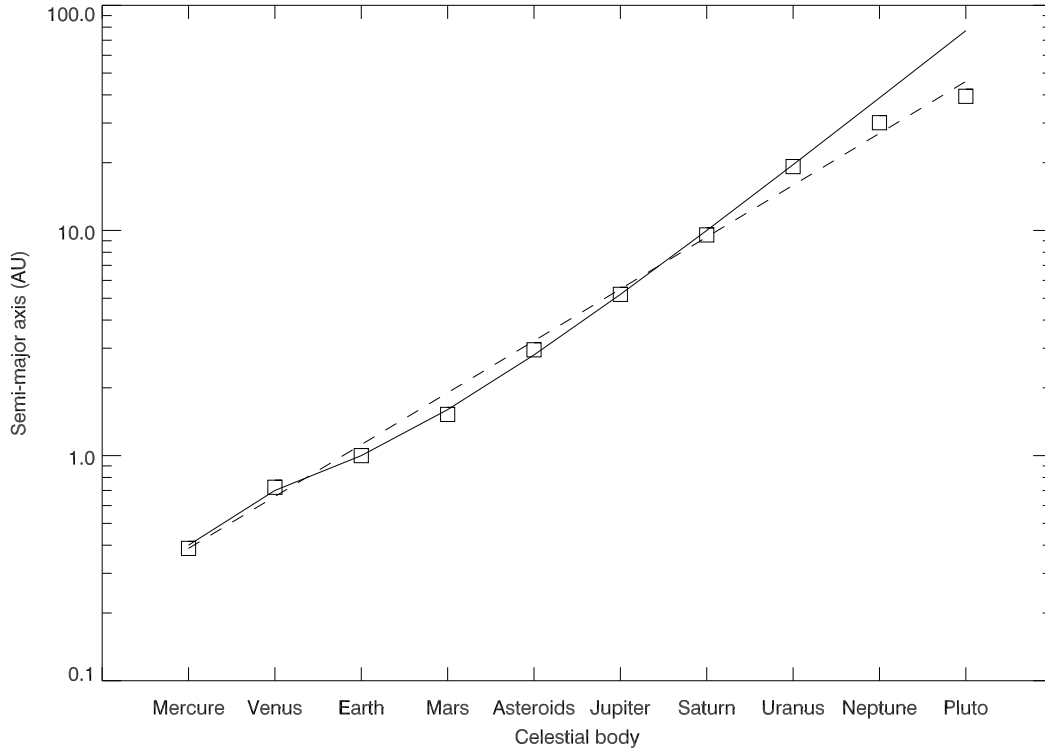


Figure 1.1. Actual semi-major axes of the planets (denoted by squares) in comparison to those calculated by the Titius-Bode law (solid line). A pure power-law fit of the form $r_n = r_0 K^n$ is also drawn (dashed line). For the solar system $K = 1.7$, while r_0 was set to match r_1 to Mercury's semi-major axis.

For any two-dimensional, axisymmetric system characterised by scale invariance in the plane perpendicular to the symmetry axis, Graner & Dubrulle (1994a) have shown that linear instabilities will lead necessarily to periodic perturbations in $x = \ln(r/r_0)$. Since equidistant spacings in x correspond to a geometric progression in r , power-laws are the natural results of such systems. In a subsequent paper, Graner & Dubrulle (1994b) applied their theoretical tools to real-world physics and performed linear stability analysis of the equations describing a cold, self-gravitating disk. They found that gravitational instabilities lead to density maxima consistent with Titius-Bode laws of the form $r_n = r_0 K^n$. The authors concluded with:

In conclusion, linear or nonlinear Titius-Bode laws can now be firmly considered as at worst numerology, at best an outcome of some simple symmetries; but even the value of the constant K does not set any relevant constraint on cosmogonic models of the solar system formation.

Eccentricities and inclinations According to Kepler's first law, all planets move on ellipses around the Sun, which sits in one of the focal points. The geometrical shape of an ellipse is parametrised by its eccentricity e , defined by $e \equiv \sqrt{1 - b^2/a^2}$, where a and b are the semi-major and semi-minor axis, respectively. A circle, being a special case of an ellipse with $a = b$, has

zero eccentricity. An inspection of the eccentricities listed in Table 1.1 makes obvious that, if we exclude Mercury and Pluto, all planets revolve the Sun on nearly circular orbits.

As for inclinations, we get a similar picture. The inclination angle i is defined as the angle of the orbital plane to the ecliptic, a hypothetical plane outlined by Earth's motion through space. We have $0 \leq i < 180^\circ$; the motion of a planet is said to be prograde if $i < 90^\circ$, otherwise retrograde. By definition, the Earth has zero inclination. Almost all planetary orbits lie close to the ecliptic and all planets revolve prograde, that is anti-clockwise when viewed from the north, which is also the sense of rotation of the Sun. Once again, Mercury and Pluto misbehave, having considerable inclinations of 7° and 17° , respectively.

We may note in passing that it is no coincidence that just the innermost and outermost planets are the outliers and abstain from the general rule. Mercury owes its perturbed orbit to the collective gravitational influence of all other planets. Being a comparably lightweight planet, the continuous push and pull results in significant alterations of Mercury's orbital parameters. Laskar (1996) treated the dynamical evolution of the solar system on Gyr time scales. While the orbital parameters of the giant planets change little, the inner solar system planets undergo large and irregular variations. Especially Mercury suffers greatly, experiencing variations in eccentricity from 0.1 up to 0.5; at the same time the inclination angle varies from 7° to 21° . The high eccentricity and steep inclination of Pluto, on the other hand, are due to its suspected Kuiper Belt provenance.²

Historical conclusion To summarise, the solar system consists of a number of planets which revolve the Sun on almost coplanar and nearly circular orbits. Conjoining these facts, able savants ventured to explain the origin of the solar system and its planets. The merit of conceiving the first scientific cosmogony is allocated to the French philosopher and geometer Descartes (1596–1650). According to him, the Universe was entirely filled with three substances of different subtleties and endowed with diverse qualities: a luminous substance the Sun and the stars are made of, a transparent aether and, finally, the coarser matter of the Earth, the planets and the rest. These fluid-like substances are in incessant turbulent and vertiginous motion; at the centres of the vortices material accumulates to form the various celestial bodies. The Earth, for example, was carried by a vortex that whirled around the Sun; a similar maelstrom around the Earth bore the Moon. Descartes's ideas were discarded after Newton's theory of universal gravitation was firmly grounded. His hydrodynamical view, however, has not been altogether forgotten; today's accretion disk theories involve concepts like turbulence and frictional dissipation of energy and angular momentum.

In view of the Newtonian revolution and its subsequent success, cosmogonic theories changed in perspective to make gravity the driving force. Most famous in this regard are the deliberations of Kant (1724–1804) and, independently, Laplace (1749–1827) who both envisaged that the solar system originally began as an enormous cloud of primordial material (cf. Figure 1.2). This "Urnebel" contracted under its own gravity to form a central concentration—the proto-Sun in modern parlance (a). Conservation of angular momentum required that during contraction any initial rotation was strongly amplified, i. e. the rotation velocity was steadily increasing. Then, the combination of gravitation (pointing towards the central body) and centrifugal forces (perpendicular to the rotation axis) eventually led to a distribution of matter in a rotating disk with the early Sun in the centre (b). Finally, the disk fragmented into rings of gas (c) that subsequently condensed to build the planets (d). This so-called "Kant-Laplace nebular hypothesis" was able to satisfy all the aforementioned observational facts in a self-consistent way. Yet no theory escapes criticism when the time is ripe. One flaw was underlined by Maxwell (1831–1879) who pointed out that the formation of planets from an annular distribution of matter is difficult to explain. A second, even

²There is a whole sub-group of the KBO family resembling Pluto in this regard, suggestively named 'Plutinos'. All bodies are caught in a 3:2 orbital period resonance with Neptune, have large eccentricities ($0.1 \leq e \leq 0.34$), and inclinations up to $\sim 20^\circ$ (Jewitt & Luu, 2000).

graver objection to the nebular theory of Kant and Laplace made clear that their ideas, however inspiring, were too simplistic. The problem of the angular momentum distribution of the solar system will become obvious in the following section.

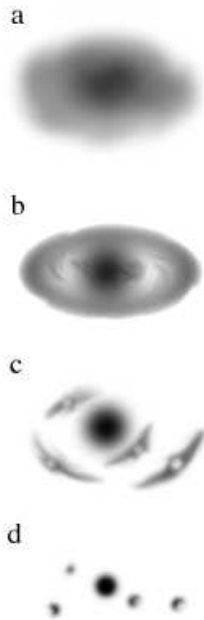


Figure 1.2. Illustration of the Kant-Laplace nebular hypothesis.

To complete our account on the different types of solar system formation models, we briefly name one other. Encounter theories that involve the close passage of an extraneous celestial body near the Sun, or even a collision between the two of them³, had been in vogue from time to time. Buffon (1707–1788) held it possible that solar material ejected after a collision with a straying comet formed the planets. After the true nature and mass of the comets became known, the comet was replaced by a star. In such a scenario, a star passes close to the Sun and material from both objects is stripped by tidal forces. The sheared off material fragments into smaller lumps which then form the planets. The major drawback of these theories is simple physics: hot filaments drawn out from either object, target or projectile, would expand rapidly rather than condense into planetary bodies.

We may anticipate that the nebular hypothesis is the “winner”. Its essential predictions have been vindicated by many observational evidence and theoretical, cf. Sections 1.2 and 1.3. The Kant-Laplace nebular hypothesis plus its crucial improvements, constitutes the most appropriate basis we have at present to understand the formation of solar systems, both our own and remote ones.

1.1.2 Mass and angular momentum distribution

After dealing with the orbital parameters of planets, we now shift attention to their physical parameters. Although they are only relics of the formation process, they can still tell something about the physical conditions prevailing at that time.

Distribution of mass The most obvious fact is that the total mass of the planets only represents a negligible fraction of the total solar system mass. More than 99.8% of the matter of the solar system is concentrated in the Sun. All the other bodies (planets, moons, asteroids etc.) account for but a trifle. This is in perfect agreement with the nebular hypothesis which predicts that matter piles up in a central object. Initially, the disk surrounding the proto-Sun was much more massive. It was cleared of matter by two processes: First, accretion onto the central object removed most of the disk material. Second, the remaining mass was blown away by the intense wind a young star develops in its early evolutionary phases. At the same time, planetesimals and planets started to grow.

Planetary two class society There is an evident dichotomy in the physical parameters of the planets in mass, size and density. Accordingly, two principal families of planets can be distinguished. First, the terrestrial planets (Mercury, Venus, Earth, Mars): they lie close to the Sun, have comparably low masses, and are small in size. Their mean density is high, suggesting a rocky composition of silicates and the presence of a dense, metallic core. The giant planets (Jupiter,

³Therefore sometimes called catastrophic theories.

Saturn, Uranus, Neptune) constitute the second group. More distant from the Sun, they are significantly larger and more massive than the terrestrial planets. Their mean density is low due to their composition which is mainly of molecular hydrogen, helium and trace amounts of methane and ammonia. The enormous pressure towards their interiors compresses the gaseous atmospheres into unusual states of matter, for instance metallic hydrogen. Down at the very bottom, rocky cores with masses of the order of $10 M_E$ are believed to exist. As already stated, Pluto does not belong to either group. The existence of this dichotomy hints at fundamental differences in the way terrestrial and giant planets formed, respectively, cf. Section 1.4.

Distribution of angular momentum Another physical quantity, angular momentum, is less obvious—some simple algebra will reveal it, though. In order to make life easier and not to overload the derivations, we restrict ourselves to rough order of magnitude estimates. The angular momentum⁴ \mathbf{J} is related to the moment of inertia I and the angular velocity $\boldsymbol{\omega}$ by

$$\mathbf{J} = I\boldsymbol{\omega}. \quad (1.1)$$

The moment of inertia is defined by $I = \int r_{\perp}^2 dm$, where r_{\perp}^2 is the perpendicular distance of a mass element dm from the axis of rotation. The planets of the solar system constitute a set of discrete masses, hence the integral changes into a sum. For the sake of simplicity we assume furthermore, that all planetary orbits are circular and coplanar; thus we drop the vector notation altogether. Accordingly, we write for the moment of inertia $I = \sum m_i r_i^2$. Introducing this into 1.1 and writing the Keplerian angular velocity of a planet with orbital radius r_i as $\omega_i = \sqrt{GM_{\odot}/r_i^3}$ yields

$$J_{\text{pl}} = \sum_{\text{planets}} m_i r_i^2 \omega_i = \sum_{\text{planets}} m_i (GM_{\odot} r_i)^{1/2} \quad (1.2)$$

for the total angular momentum of the planets; G and M_{\odot} are the gravitational constant and the solar mass, respectively. Substituting the masses and orbital radii listed in Table 1.1 one obtains $J_{\text{pl}} = 3 \times 10^{43} \text{ kg m}^2 \text{ s}^{-1}$, in perfect agreement with available reference values (see for example Cox, 2000). The calculation of the solar angular momentum is more difficult and fills one page alone. We use the value given by Pijpers (1998), $J_{\odot} = 2 \times 10^{41} \text{ kg m}^2 \text{ s}^{-1}$, as determined from *SOHO* and *GONG* observations.

Comparison between the total angular momentum retained by the planets and that of the Sun yields that most of the angular momentum of the solar system lies in the planets—the ratio J_{\odot}/J_{pl} being less than one hundredth. This result is in stark contrast to the distribution of mass in the solar system. While almost all of the matter is concentrated in the Sun ($\geq 99.8\%$), its contribution to the angular momentum budget of the solar system is negligible. In the model of Kant and Laplace, however, the central body ought to have kept most of the angular momentum whilst collapsing from a molecular cloud. Had it done so, the present Sun would rotate in just a few hours, instead of the laggardly ~ 25 days it actually takes to complete one rotation.

Therefore, angular momentum must have been transferred from the central object to the surrounding planetary system. As the angular momentum of any mechanical system is conserved for

⁴Contrary to common practice in physics, we denote the angular momentum by \mathbf{J} rather than \mathbf{L} simply to eliminate a possible confusion between angular momentum and luminosity.

purely central forces $\mathbf{F}(\mathbf{r}) = f(\mathbf{r})\mathbf{r}$,

$$\frac{d}{dt}\mathbf{J} = \sum \mathbf{r}_i \times \mathbf{F}_i = \mathbf{0}, \quad (1.3)$$

this cannot be achieved by gravitation. Necessarily, non-central forces and dissipative processes come into play; see Section 1.3.1 for a short description.

1.1.3 Element abundances

The clues one can draw from the information contained in Table 1.1 are exhausted by now. To substantiate the picture of the solar system formation, one has to include the chemical composition of the solar system bodies.

The determination of the solar system abundances is based on two distinct types of measurements. One is a precise quantitative analysis of spectral lines as seen in solar photospheric light, resulting in a relative abundance $n(X)$ for every element X present in the photosphere. It is common practice to use a logarithmic scale $\log n(X)$; the accuracy reached is approximately $|\Delta \log n(X)| \lesssim 0.1$. As the solar atmosphere is chemically decoupled from the hydrogen burning in the core, it still retains the initial mixture of elements at the time of the formation of the Sun.

The other type of measurement consists of laboratory studies of appropriate solar system solids. However, not all samples are equally useful for this purpose. The larger rocky bodies have been modified by gravity-driven fragmentation (sedimentation) and by the loss of volatile elements. Accordingly, measurements of specimen from the Earth's or lunar crust are biased. Besides the remote cometary nuclei, the most primitive bodies we find in the solar system are meteorites. Of them, a particular class of stony meteorites, the so-called carbonaceous chondrites, are preferred because among all known meteorite classes they exhibit evidence of the least thermal processing (melting) and chemical alteration. Carbonaceous chondrites are composed of a fine-grained, carbon-rich silicate matrix and, interspersed therein, millimetre-sized spherical inclusions—the chondrules⁵—of mainly silicate composition (cf. Figure 1.3). As a whole, they are considered to be the best representatives of the primordial solar nebula. Analysis of their chemical composition yields accuracies of the order of $\Delta \log n(X) \simeq 0.05$ for most elements, i. e. by a factor of two more sensitive than those of the solar atmosphere.



Figure 1.3. Cut of a carbonaceous chondrite found on the Dar al Gani plateau, Libya. The specimen is some centimetres across.

Comparison of solar and meteoritic element abundances When comparing the measurements of solar and meteoritic element abundances, respectively, one obtains an almost exact agreement, see Figure 1.4. The correspondence is perfect for most of the elements, which underpins the general picture that meteorites, as well as other bodies, condensed from a gaseous nebula of solar composition. There are, however, some notable outliers, such as the noble gases (helium, neon, argon) and other volatile elements (nitrogen, hydrogen, carbon and oxygen). All these elements

⁵Derived from the Greek word $\chi\omicron\nu\delta\rho\varsigma$, meaning “grain”.

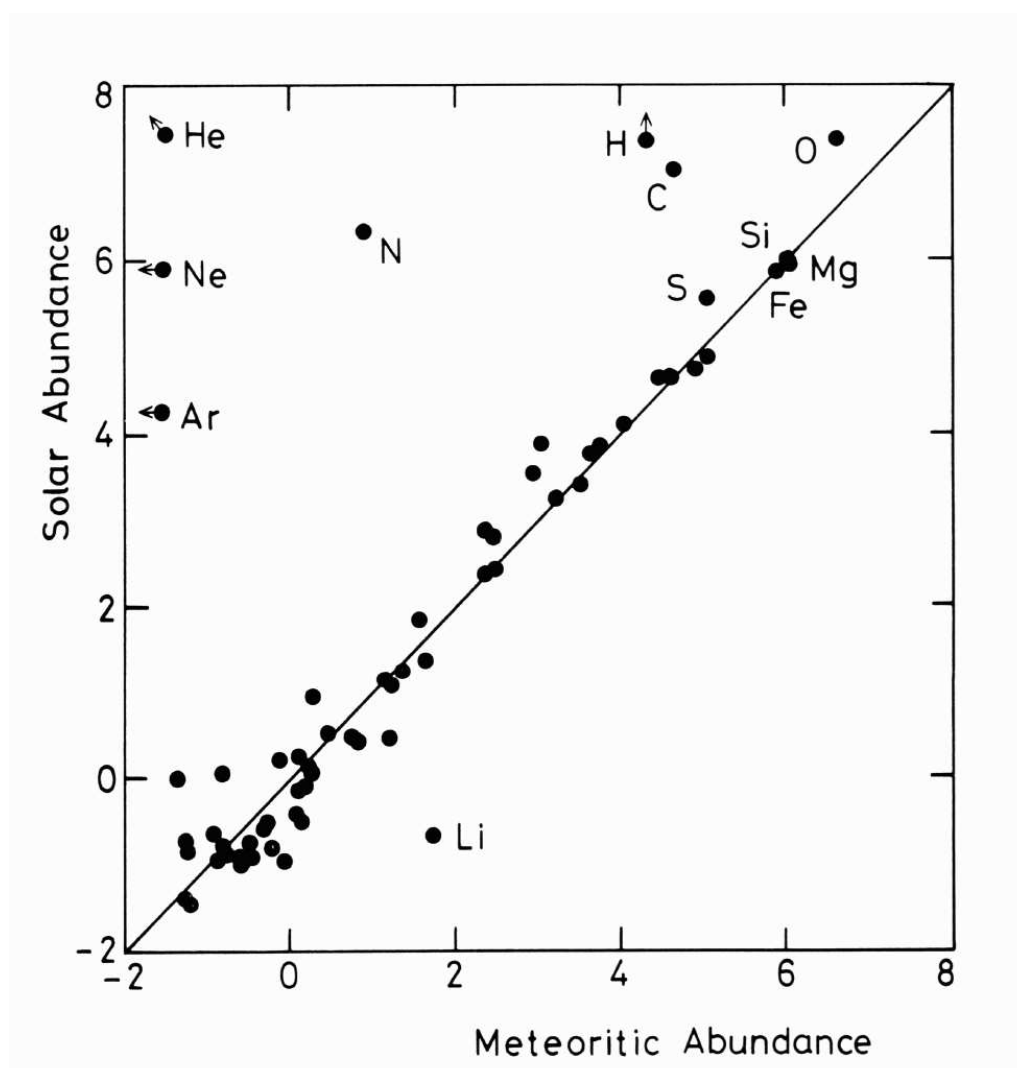


Figure 1.4. The correlation of the chemical abundance of elements in the solar atmosphere and those of a typical carbonaceous chondrite. Abundances are given by number of atoms on a logarithmic scale, normalised to that of silicon (Si) being equal to 6. Plot taken from Whittet (1992).

lie above the line representing exact agreement, thus being overabundant in the solar atmosphere, or underabundant in meteorites. Nobel gases are chemically inert and cannot be built into compounds; they remain in the primordial nebula and do not condense into meteorites. The elements of the second group condense partially. In the solar atmosphere, only one element is significantly underabundant, namely lithium. The temperatures at the lower boundary of the convection zone suffice to burn lithium via the nuclear reactions ${}^7\text{Li} + \text{p} \rightarrow {}^4\text{He} + {}^4\text{He}$ and ${}^6\text{Li} + \text{p} \rightarrow {}^4\text{He} + {}^3\text{He}$. By degrees, the photospheric lithium abundance is diminished. In this case, the meteoritic lithium abundance is more likely to represent the true initial value.

Radioisotope dating One very important number cannot be determined other than by measuring specific element abundances—the age of the solar system. The method applied is based on the principle of radioisotope dating and uses the fact that some isotopes incorporated into minerals and

grains are unstable and decay radioactively into other isotopes. The excess of these end products can, in principle, serve as a measure of the time elapsed since the condensation of the grain.

From the multitude of radioactive decays, only some isotope pairs are used. For example: ^{87}Rb and its daughter isotope ^{87}Sr with ^{86}Sr serving as the stable reference isotope; ^{40}K and ^{40}Ar , ^{36}Ar being the gauge; the pair ^{238}U and ^{206}Pb . These and other decays used for radioisotope dating are summarised in Table 1.2. All of them are characterised by Gyr half-lives, thereby enabling sensitive abundance measurements and an accurate dating of the samples.

Table 1.2. Radioactive decays used for radioisotope dating

Parent isotope	Daughter isotope	Decay products	Half-life $T_{1/2}$ [yr]
^{147}Sm	^{143}Nd	α	$(1.06 \pm 0.02) \times 10^{11}$
^{87}Rb	^{87}Sr	β	$(4.75 \pm 0.04) \times 10^{10}$
^{187}Re	^{187}Os	β	$(4.35 \pm 0.13) \times 10^{10}$
^{232}Th	^{208}Pb	$6\alpha + 4\beta$	$(1.405 \pm 0.006) \times 10^{10}$
^{238}U	^{206}Pb	$8\alpha + 6\beta$	$(4.468 \pm 0.003) \times 10^9$
^{235}U	^{207}Pb	$7\alpha + 4\beta$	$(7.038 \pm 0.005) \times 10^8$
^{40}K	^{40}Ca	β	} $(1.277 \pm 0.008) \times 10^9$
	^{40}Ar	Electron capture	

SOURCE: Half-lives taken from the *Table of Radioactive Isotopes*, a nuclear decay database in collaboration of the LBNL, Berkeley, USA, and the Division of Nuclear Physics at Lund University, Sweden.

Precise measurements for a wealth of meteoritic specimens as well as fragments of near-earth asteroids indicate a common formation date approximately 4.57 Gyr ago (Allègre et al., 1995). Crystallisation took place rapidly within ten million years, very fast on astronomical time scales. The planets and their moons formed somewhat later after planetesimals accretion had built up larger bodies. Determinations of the age of the Sun using helioseismology are consistent with the value determined from meteoritic data, see Dziembowski et al. (1999), for example, who specified the solar age as (4.66 ± 0.11) Gyr.

Isotopic studies of meteorites also reveal evidence for the presence of short-lived nuclei in the primordial nebula through the excess of their corresponding daughter isotopes. Analytical tools are, for example, the decays $^{129}\text{I} \rightarrow ^{129}\text{Xe} + \beta$ and $^{26}\text{Al} \rightarrow ^{26}\text{Mg} + \beta^+$, with half-lives of 1.6×10^7 yr and 7.2×10^5 yr, respectively. The parent nuclei probably issue from nucleosynthetic processes connected with supernovae, AGB stars or Wolf-Rayet stars, and become subsequently incorporated into the solar nebula. These facts argue for a triggered collapse scenario where shock waves coming from one of these stellar events caused a sudden compression which initiated the infall of the pre-solar cloud (Goswami & Vanhala, 2000).

1.2 Star formation: an overview

After focusing on our own solar system and the lessons it can reveal, we can start looking at the formation of planets. Planets form in circumstellar disks, remnants of the star formation proper. Hence the question of the formation of planets is inevitably intertwined with the formation of the central star. As we have already seen for the case of our solar system, the planets were born out of the same natal material as the Sun. Isotopic evidence suggests that this condensation process from the gaseous primordial nebula into crystallised solids must have happened on comparatively short time scale. It is therefore vital to start our considerations with a concise overview of the formation of stars and their circumstellar disks.

1.2.1 The physics towards a star

Molecular clouds Stars form in the densest parts of molecular clouds, vast and cold accumulations of interstellar matter. Molecular clouds differ in their physical properties such as size, density, mass, and temperature; Cernicharo (1991) presented a possible bimodal classification scheme that we adopt here. Giant molecular clouds measuring 20–60 pc in size and enclosing 10^5 – $10^6 M_{\odot}$ are located in the spiral arms of the Galaxy. The smaller dark clouds, containing 10^3 – $10^4 M_{\odot}$, are not always linked to spiral arms. These larger units fragment into smaller regions of enhanced density. Inside these cloud cores, star formation proper begins. Figure 1.5 shows a millimetre continuum observation of a part of the ρ Oph molecular cloud.

Gravitational instability and collapse A molecular cloud is a gravitationally bound object. Contraction under its own gravity is counteracted by the thermal pressure of the cold gas ($T \approx 10$ – 100 K), the existence of magnetic fields, and large-scale turbulent motions within the cloud (a few km s^{-1}). Successful early star formation must, somehow, overcome these opposing forces to yield increasingly compact condensations, some of which reach stellar sizes at last.

The question arises under which circumstances and conditions a gaseous mass is liable to gravitational collapse. This problem was first addressed by Jeans (e. g. Jeans, 1928). He considered a virialised gaseous sphere of radius R and mass M with a homogeneous density ρ . For a bound gravitational system, the virial theorem states that twice the kinetic energy $\langle K \rangle$ and the gravitational potential energy $\langle U \rangle$ add to zero,

$$2 \langle K \rangle + \langle U \rangle = 0. \quad (1.4)$$

(The brackets denote a statistical mean obtained by averaging over a sufficiently long time). Dividing Equation 1.4 by $-\langle U \rangle$ one may rewrite it as

$$-\frac{2 \langle K \rangle}{\langle U \rangle} = 1. \quad (1.5)$$

Fulfilment of this condition ensures gravitational stability. If the kinetic energy is too small, i. e. the inner thermal pressure too low, or else the gravitational field too strong, gravitational instability sets in and the cloud collapses. Mathematically this corresponds to transforming Equation 1.5 into an inequality where the ratio $-2 \langle K \rangle / \langle U \rangle$ is smaller than unity.

Introducing the proper expressions for the kinetic energy $\langle K \rangle$ of a di-atomic gas and the gravitational potential energy $\langle U \rangle$ of a homogeneous sphere, respectively, yields the following insta-

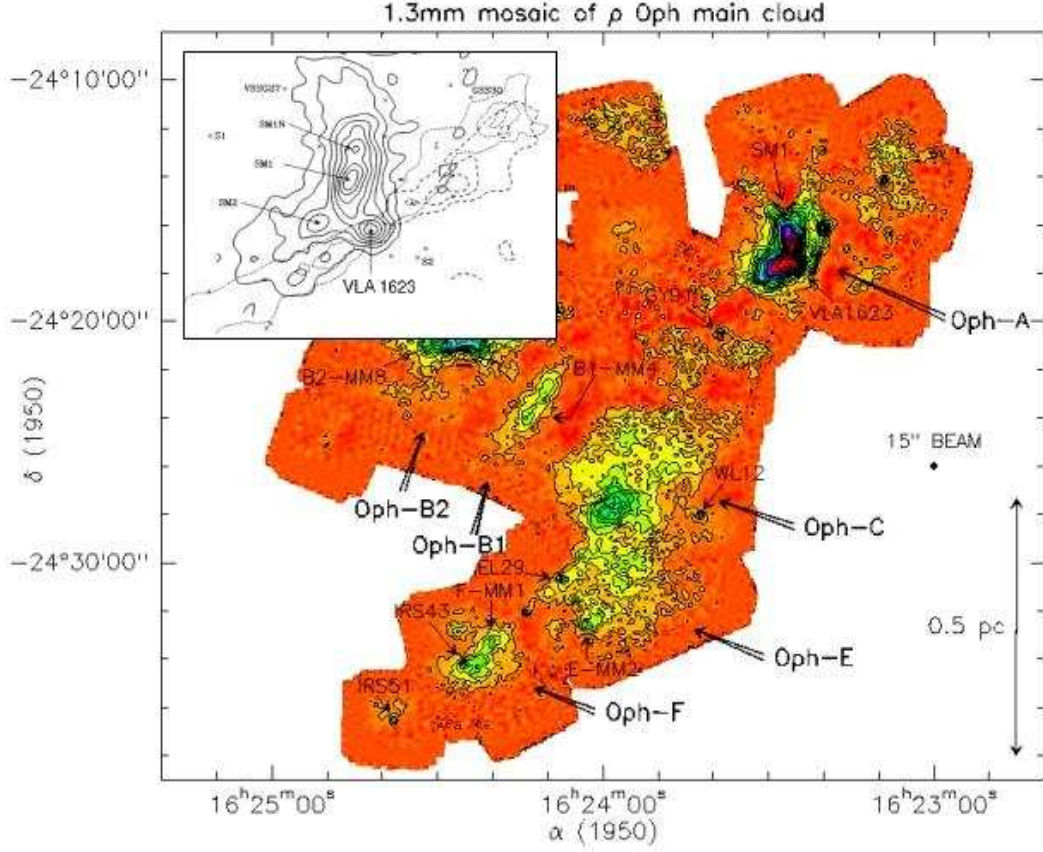


Figure 1.5. Dust continuum mosaic of the ρ Oph cloud taken at 1.3 mm with the Plateau de Bure (IRAM) 30-m telescope. Reddish colour tones show low density, while the sequence green-blue-violet codes increasing density. The inset shows an enlargement of the dense Oph-A cloud core (upper right corner). The compact clump VLA 1623 at the centre of Oph-A is a prototypical Class 0 protostellar object (see 1.2.2) and shows presence of a bipolar outflow. Modified after André et al. (1993, 2000).

bility criterion

$$-\frac{2\langle K \rangle}{\langle U \rangle} = \left(\frac{5k_B T M}{\mu u} \right) \left/ \frac{3}{5} \frac{GM^2}{R} \right. < 1, \quad (1.6)$$

where k_B is Boltzmann's constant, T the temperature of the gas, μ its mean molecular weight, u the atomic mass unit, and G the gravitational constant. The introduction of turbulence is straightforward and amounts to replacing the thermal kinetic energy of one gas particle $(5k_B T)/(2\mu u)$ by the velocity dispersion $\frac{1}{2}\langle v^2 \rangle$ of the gas. Observationally, velocity dispersions can be measured by Doppler mapping techniques. Furthermore, if we were to start with a non-homogeneous density distribution $\rho = \rho(r)$, the factor in the denominator of 1.6 would change moderately. For the sake of simplicity we leave 1.6 as it is.

Solving for R , one finds that a gaseous sphere can only collapse if its radius is smaller than a critical radius R_J , the so-called Jeans radius,

$$R_J = \frac{3}{25} GM \frac{\mu u}{k_B T}. \quad (1.7)$$

The corresponding Jeans mass M_J contained in a sphere of radius R_J is easily obtained by setting $M = (4\pi/3)R^3\rho$ and solving Equation 1.7 for M . One arrives at

$$M_J = \sqrt{\frac{125}{36\pi}} \left(\frac{k_B T}{G\mu u} \right)^{3/2} \rho^{-1/2} \approx \left(\frac{k_B T}{G\mu u} \right)^{3/2} \rho^{-1/2}, \quad (1.8)$$

since the root in the first expression is nearly one. Any gaseous sphere mass more massive than this critical mass will collapse. In order to have a more handy expression, we insert the physical constants and set the mean molecular weight to $\mu = 2$, corresponding to a pure molecular hydrogen gas. Equation 1.8 becomes

$$\frac{M_J}{M_\odot} \approx 2.6 \times 10^{-10} \left(\frac{T}{\text{K}} \right)^{3/2} \left(\frac{\rho}{\text{kg m}^{-3}} \right)^{-1/2}. \quad (1.9)$$

It is important to observe the dependencies of the Jeans mass on the two free parameters, gas temperature and density. While the collapsing mass M_J is inversely proportional to the square root of the density ρ , it increases with the temperature T raised to the power of 3/2. Now, starting from a cold and tenuous cloud of gas, large masses become gravitationally unstable at first, leading to an infall of matter and increasing the density of the nebula. Smaller pockets of matter are only capable of collapsing after the gas has been sufficiently compressed to higher densities. Through successive compactification, a top-down scenario is initiated, where condensation starts on large scales and fragments down to small-scale objects. The crucial prerequisite, of course, is to prevent the temperature from rising, which would otherwise thwart the formation of increasingly smaller, compact objects.

Cooling processes in protostellar clouds Thermal energy has to be removed from a contracting protostellar cloud to ensure further contraction. In principle, there are two different processes that transform the kinetic energy of the gas particles into heat which then is radiated away. The first such agent is an essential part of the interstellar medium—submicrometre-sized, solid dust grains. The mass proportion of dust in relation to that of the gaseous component of the interstellar medium (mainly hydrogen) is of the order of one part in 100. Despite of this scarcity, dust nevertheless dominates optical extinction due to its enormous cross section when compared to atomic or molecular scattering cross sections. The second process involves the mutual collisions of molecules or atoms that constitute the nebular material. Both processes are sketched in Figure 1.6 and discussed ensuingly.

An atom or molecule of velocity v has a kinetic energy of $\frac{1}{2}mv^2$, where m is its mass. Whenever such a gas particle hits a dust grain (a), the grain becomes slightly heated and radiates away the absorbed energy as heat (b). The impinging particle loses some of its kinetic energy and remains with a reduced velocity $v' < v$. Thus, part of the kinetic energy of the gas is transformed into electromagnetic radiation. As a consequence, the gas is accelerated towards the centre of the cloud. During the fall, the velocity grows, and part of the energy is again transferred to dust grains—hence the cycle of collision and cooling starts anew. By degrees, the cloud's total kinetic

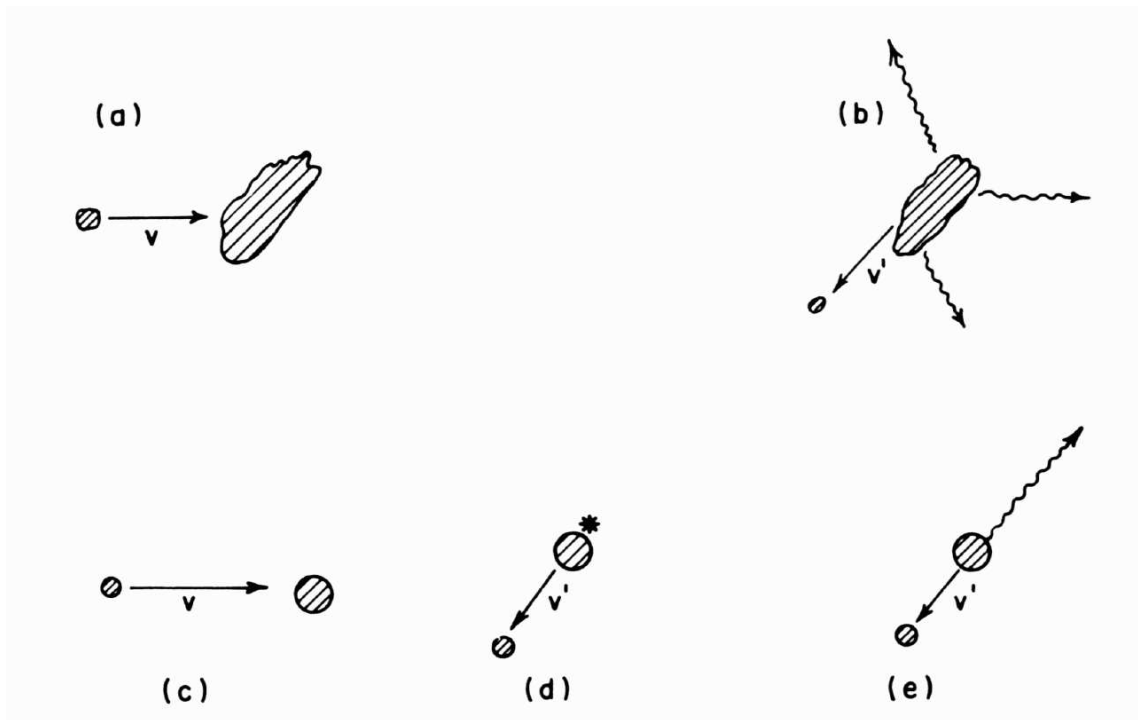


Figure 1.6. Cooling processes in protostellar clouds. The graphic is supposed to be read from left to right. A gas particle with velocity v impinge upon a dust grain (upper part) or collides with another atom or molecule (lower part), respectively. For a detailed description see accompanying text. Taken from Harwit (1998).

energy is reduced, leading to further contraction.

Mutual collisions between atoms and molecules represent another effective way of detracting kinetic energy from a protostellar cloud. The setting is similar to the situation above: A gas particle with a relative velocity v hits a fellow particle (c). Thereby, the stricken atom or molecule is excited into a higher energy level, symbolised by an asterisk in (d). From there it decays via one or more transitions (electronic, vibrational or rotational) through photon emission into the ground state (e). Again the first particle loses kinetic energy. Radiation with infrared or longer wavelength easily escapes, and the loss of kinetic energy cools the protostellar cloud.

Ambipolar diffusion Besides thermal pressure, magnetic fields provide support against self-gravitation and subsequent collapse of a molecular cloud. A magnetic field configuration resists compression traverse to the field lines; it exerts a magnetic pressure proportional to the square of the field strength, $P \propto B^2$. Furthermore, the net magnetic flux out of any closed surface is zero, $\oint_S \mathbf{B} \cdot d\mathbf{A} = 0$. The latter fact implies that the magnetic field increases as $B \propto r^{-2}$ when compressing a cloud of size r . The magnetic pressure opposing the collapse rises tremendously as $P \propto r^{-4}$. To give an instructive example, consider the case of a subparsec-sized protostellar cloud possessing an initial magnetic field of, say, some 10^{-9} T (cf. Crutcher, 1999). A collapse down to solar dimensions spans six orders of magnitude in size. The corresponding magnetic field would be amplified by twelve orders of magnitude, reaching a field strength up to 1000 T. Observed magnetic field strengths in the quiet solar photosphere, however, are smaller than 0.05 T (Keller

et al., 1994). We conclude that protostars must have shed this excessive magnetic field in order to contract to stellar sizes—the process in hand is ambipolar diffusion.

Dust not only facilitates kinetic energy removal from a collapsing molecular cloud. It is also a powerful blocker against ionising ultraviolet radiation emanating from nearby massive stars. Most of the hydrogen gas in the cloud is neutral. Only a negligible fraction is ionised by cosmic rays. Regions of stronger magnetic fields, produced by squeezed or flexed field lines, tend to relax into regions where magnetic field strength and the associated pressure is lower. Ions and electrons that gyrate around the field lines and are fixed to them, therefore, drift into areas of reduced field strength. This process is called ambipolar diffusion, or ion-neutral drift. The situation is depicted in Figure 1.7.

Through successive collisions with uncharged, resting particles, the charged particles gain a relative velocity v against the non-moving background of neutral particles. For a typical molecular clump of subparsec dimension, a magnetic field strength of a few 10^{-10} T, and an ionisation fraction of 10^{-6} , Harwit (1998) estimated the drift velocity v to be of the order of some ten cm s^{-1} (The corresponding thermal velocity is of the order of km s^{-1} .) At that rate, field diffusion would last 5×10^8 yr—a very slow process indeed. However, ambipolar diffusion might work efficiently during the initial phases of star formation; there the molecular cloud is still tenuous, which would downscale the characteristic diffusion times to some 10^6 yr. In addition to magnetic field expulsion, repetitive collisions of ions with dust particles partially align the grains, changing their light scattering behaviour and leading to net polarisation (Roberge et al., 1995).

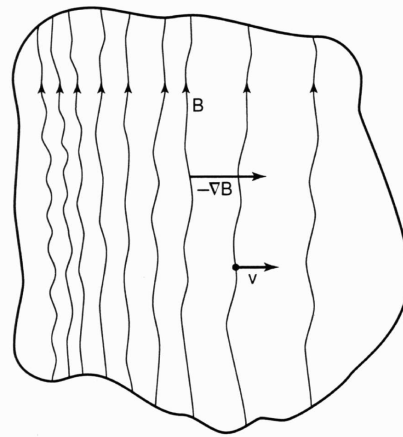


Figure 1.7. Magnetic field gradients and resulting ion drift (ambipolar diffusion). Taken from Harwit (1998).

1.2.2 Spectral energy distribution classification

After it has been demonstrated how a molecular cloud core principally sheds thermal kinetic energy and magnetic field to reach increasingly compact condensations, we proceed to tell the rest of stellar infancy—finally arriving on the zero-age main sequence.

The evolutionary sequence from a cloud core down to a hydrogen-burning star leaves its footprints in the spectral energy distributions of young stellar objects. Their shapes can reveal important insight into the physical parameters of the contracting star and the surrounding disk. Moreover, they contain valuable information about the mineralogical components and particle size distribution of dust (Chiang et al., 2001). Spectral energy distributions have been used to devise a classification system that covers the whole evolutionary sequence of objects and events—from the dense cloud cores to the T Tauri stars (Lada & Wilking, 1984; Adams et al., 1987; André et al., 2000). The slope of the spectral energy distribution in the near- to mid-infrared $\alpha \equiv d \log(\lambda F_\lambda) / d \log \lambda$ is used as the class-dividing criterion. Sources with $\alpha > 0$ are called Class I objects; those with $-2 < \alpha \leq 0$ are classified as Class II; and young stellar objects with a spectral index $\alpha < -2$ belong to the Class III. Very young protostars with peak emission in

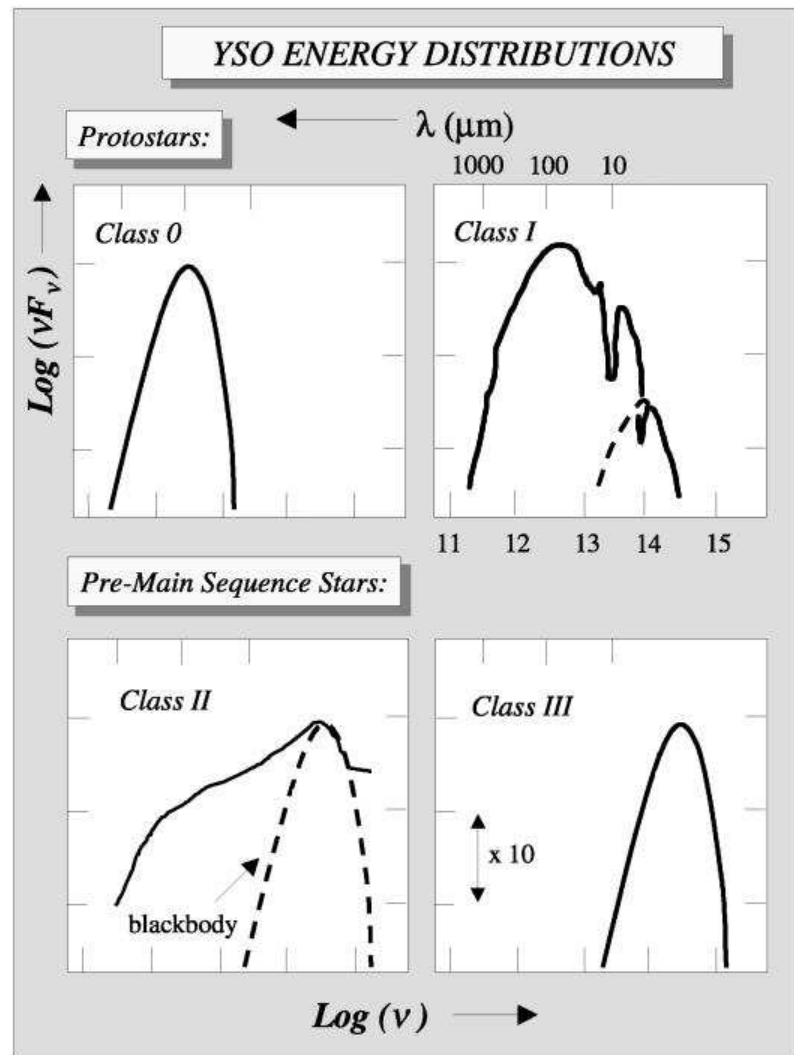


Figure 1.8. Spectral energy distributions and corresponding classification of young stellar objects. The dashed line fits a blackbody radiation law to the high-frequency wing of the given energy distributions. See text for discussion. Taken from Lada & Kylafis (1999).

the submillimetre range are assigned to be Class 0. Figure 1.8 depicts this classification scheme of young stellar objects. For each class the prototypical spectral energy distribution is drawn into a νF_ν over ν diagram. This particular way of plotting an SED shows in which frequency range most of the flux is emitted by the source. Before discussing each class on its own, one may notice that both Class 0 and Class III are perfect blackbodies, that means the sources are in a state of thermodynamical equilibrium.

Class 0 A protostar has come into existence; most of its to-be mass, however, is still surrounding the central condensation (André et al., 2000). Therefore, the object is cold and emits most of its radiation in the far-infrared and submillimetre wavelength regions. Often a molecular outflow, a bipolar stream of highly diluted but fast moving gas (Richer et al., 2000), is present. The

prototypical example is the compact radio source VLA 1623 in the ρ Oph molecular cloud (see Figure 1.5 and inset therein). The compact clump has a size of roughly 1000 AU and a mass of $0.6 M_{\odot}$. The temperature of the surrounding envelope has been found to be approximately 20 K. The age of the protostar is ~ 6000 yr roughly (André et al., 1993).

Class I The spectral energy distribution for a Class I object is less dull than for the previous class. There is evidently a large infrared excess which cannot be fitted by a single temperature blackbody. Furthermore, we find two prominent absorption features; one at $10 \mu\text{m}$ corresponding to solid silicate grains (Whittet, 1992), the other at $3 \mu\text{m}$ due to water ice (Léger et al., 1983) adsorbed on the dust grains. In this evolutionary phase the dusty envelope is rapidly collapsing onto the central object; the gain in mass results in a rise in temperature. However, it is still enshrouded in an optically opaque veil, therefore invisible at near-infrared or optical wavelengths. Again molecular outflows are present, however, less powerful than with Class 0 objects (Bachiller & Tafalla, 1999). Figure 1.9 captured a collimated, jet-like outflow of a protostar in stunning symmetry.

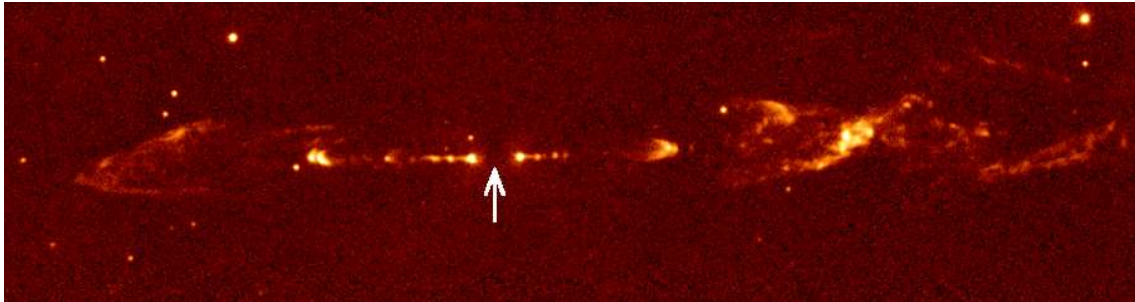


Figure 1.9. A pulsated jet emanating from an embedded protostar (arrow); the whole complex is known as HH 212. This 2.5×1.0 arcmin² image taken in the $v=1 \rightarrow 0$ $S(1)$ line of molecular hydrogen at $2.122 \mu\text{m}$ shows a pulsated, bipolar outstream of matter. As the jet rams into the ambient medium it is shocked and heated, leading to the evenly spaced knots on either side of the driving source. From Zinnecker et al. (1998).

Class II At this stage, the flux peaks in the optical, i. e. the object becomes detectable for telescopes operating in the near-infrared or optical; the infrared excess is still large. In addition, there is an ultraviolet excess shortward of around 300 nm. The infall of the surrounding gas and dust envelope as described for the Class I object, left the circumstellar material in a flat, rotating disk. This comes about as gravitational attraction and centrifugal force are not co-aligned; the resultant net force accelerates the circumstellar material towards a plane perpendicular to the rotation axis of the protostar. Irradiation of the disk by the central star warms the disk which then, in turn, represents a distended infrared radiation source (Kenyon & Hartmann, 1987). After the infall has petered out, the light of the central object is no longer obstructed from our view and the star emerges. Figure 1.10 shows four pre-main-sequence stars and their corresponding circumstellar disks, imaged directly against the bright nebulosity background of the Orion Nebula.

Feeding of the central star through disk accretion causes the optical and ultraviolet continuum excess emission (Lynden-Bell & Pringle, 1974). Stars combining these characteristics along with strong emission lines ($H\alpha$, for example) are called T Tauri stars. In fact, Class II protostars are identical to the so-called classical T Tauri stars. At this very point we come across the topic in hand for this work, viz. the early stages of planet formation in circumstellar disks. It is believed that circumstellar disks as those shown in Figure 1.10 are the birthplaces of future planetary systems.

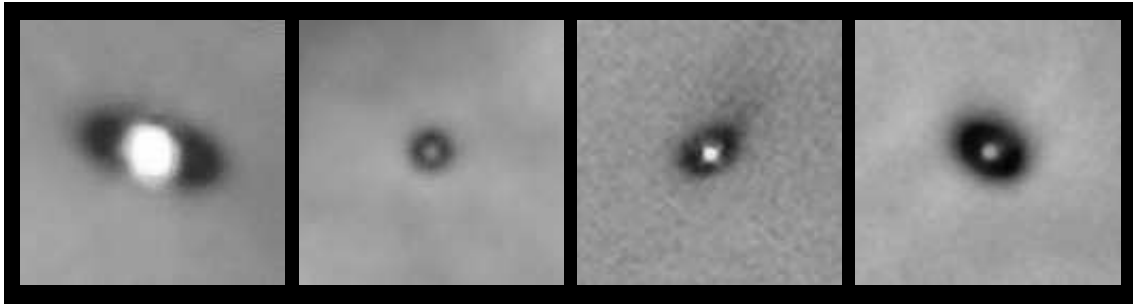


Figure 1.10. Four $H\alpha$ images of circumstellar disks in the Orion Nebula taken with the WFPC2 camera on-board the *Hubble Space Telescope*. The disks appear as dark silhouettes against the bright background nebulosity as provided by H II regions. Each panel is 2.0×2.0 arcsec², corresponding to 900 AU at 450 pc. From McCaughrean & O’Dell (1996).

Class III The spectral energy distributions of Class III objects are nearly perfect blackbodies. There is no infrared excess, i. e. the surrounding disk has been cleared of almost all its gas and dust. Possibly, dust grains have agglomerated to form planetesimals and planets. There is a weak optical excess emission; for that reason these objects are dubbed weak-emission T Tauri stars.

It remains for the star to approach the zero-age main sequence and start hydrogen burning. Before that, the only energy source the star has at its disposal is slow gravitational contraction. The time for which conversion of gravitational energy E_{grav} can maintain an object’s luminosity L is the so-called Kelvin-Helmholtz time scale. It is defined by

$$\tau_{\text{KH}} \equiv \frac{|E_{\text{grav}}|}{L}. \quad (1.10)$$

We put in the rough estimate GM^2/R for the usable gravitational energy, apply the virial theorem (Equation 1.4), and write

$$\tau_{\text{KH}} \simeq \frac{GM^2}{RL} \simeq \frac{E_{\text{therm}}}{L} \propto \frac{M}{L}, \quad (1.11)$$

since the thermal energy is proportional to the stellar mass M . Zinnecker et al. (1993) derived an empirical, time-dependent mass-luminosity relation for pre-main-sequence stars of the form $L \propto M^{8/5} \times t^{-2/3}$. The Kelvin-Helmholtz time scale is hence much smaller for more massive stars; Figure 1.11 reflects this fact plotting theoretical evolutionary tracks for pre-main-sequence stars with different masses. While stars with masses $\lesssim 0.5 M_{\odot}$ need more than 10^8 yr to arrive on the main sequence, those having $\gtrsim 4.0 M_{\odot}$ attain stardom in less than 1 Myr. The evolutionary picture drawn is, strictly speaking, only valid for pre-main-sequence stars with $\lesssim 10 M_{\odot}$. Massive stars may form in the very centres of dense clusters through mergers of low-mass stars (see Stahler et al., 2000).

The similarity of pre-main-sequence stars to those on the main sequence demands special “youth” indicators to distinguish the two of them. One secure way to identify a pre-main-sequence star as such involves the spectroscopic analysis of the 6707 Å lithium line. Lithium is readily burned at the lower bottom of the stellar convection zone once the temperature there exceeds 2.5×10^6 K (Bodenheimer, 1965). Measurements of the lithium abundance aided by stellar evolution models and nuclear reaction rates can therefore be employed to, first, identify young stars and,

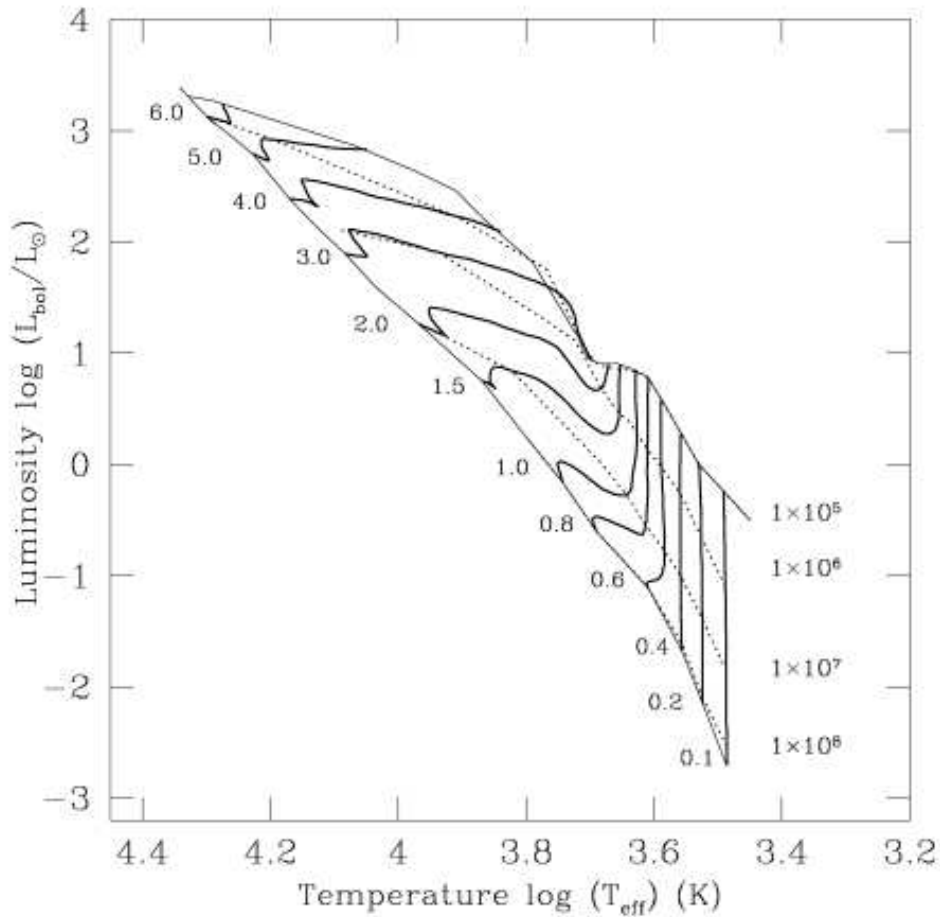


Figure 1.11. Theoretical evolutionary tracks for pre-main-sequence stars with masses from 0.1 to $6.0 M_{\odot}$ (solid lines). All tracks start at 10^5 yr and end on the zero-age main sequence where hydrogen burning is ignited. Isochrones are drawn as dotted lines for 10^6 , 10^7 and 10^8 yr to indicate the speed of the contraction. Note how the birth-line converges towards the main sequence for increasing mass; it intersects the latter at approximately $10 M_{\odot}$. protostars exceeding this weight class have no pre-main-sequence phase as such and are already burning hydrogen. After Palla & Stahler (1999).

second, determine their age. The other method employs the fact that low-mass pre-main-sequence stars are luminous X-ray emitters (Walter, 1986; Montmerle et al., 2000). Responsible for this is a strong magnetic activity due to fast rotation and the coiling up of magnetic fields in a differential velocity field. X-ray satellite surveys can therefore reveal complementary information to complete the picture of young stars.

1.3 Circumstellar disks

It has been demonstrated in the preceding section that disk formation is an integral and inevitable part of star formation. The following section will discuss relevant issues of circumstellar disks in more detail. At first, a brief overview of the process of disk accretion will be given. Of course, this cannot be done without accounting for possible mechanisms of angular momentum transport. Then we focus on the observational evidence for circumstellar disks, both indirect (e. g. infrared excess) and direct (imaging). After that, the physical properties inferable are discussed briefly.

1.3.1 Disk accretion and angular momentum transport

A collapsing cloud core has not only to lose thermal energy and to diffuse magnetic field to form a protostar. It must also rid itself of angular momentum. One source of angular momentum is the galactic differential rotation; its velocity field $\mathbf{v}(r)$ issues an angular velocity of $\omega = \frac{1}{2} |\nabla \times \mathbf{v}|$ to a molecular cloud. The other source involves a turbulent galactic velocity field, possibly maintained by feedback mechanisms like supernovae explosion or powerful stellar winds emanating from OB stars. A gravitationally unstable cloud core is then imparted its due share of the angular momentum budget through fragmentation and turbulence in the parental molecular cloud. Collapse to stellar size will most likely lead to further fragmentation into a multiple star system. Finally, angular momentum conservation obliges the infalling envelope to pile up gas and dust in a circumstellar disk (Bodenheimer, 1995; Bodenheimer et al., 2000). After disk formation, the process of disk accretion sets in: dissipative, viscous processes in the circumstellar disk transfer angular momentum outwards while most of the matter is transported onto the central object (Lynden-Bell & Pringle, 1974). In the course of this scenario, from the molecular cloud core down to stellar dimensions, the initial angular momentum is reduced by six orders of magnitude (cf. Table 1.3).

Table 1.3. Characteristic values of specific angular momentum

Object	J/M [$\text{m}^2 \text{s}^{-1}$]
Giant molecular cloud (scale 45 pc) ^a	5×10^{22}
Molecular cloud (scale 1 pc)	10^{21}
Molecular cloud core (scale 0.1 pc)	10^{19}
Binary (10^4 yr period)	4×10^{18} – 10^{19}
Binary (10 yr period)	4×10^{17} – 10^{18}
Binary (3 day period)	4×10^{16} – 10^{17}
100 AU disk ($1 M_{\odot}$ central star)	4.5×10^{18}
T Tauri star (spin)	5×10^{15}
Jupiter (orbit)	10^{18}
Present Sun	10^{13}

SOURCE: Table adapted from (Bodenheimer, 1995),
(a) Value taken from Blitz (1993)

The mass input of the collapsing envelope into the circumstellar disk is of the order of $\sim 10^{-5} M_{\odot} \text{ yr}^{-1}$; the accretion rate from the disk on the young, central star on the other hand is typically $\sim 10^{-7} M_{\odot} \text{ yr}^{-1}$ (Hartmann, 1998). This apparent disproportion might be an explanation for the enigmatic behaviour of the so-called FU Orionis variables, a rare subclass of young stellar objects showing brightness variations up to 5 mag in the optical (Herbig, 1977). As more and more material is amassed, the circumstellar disks might become gravitationally unstable, in the wake of which the accretion rate would increase rapidly (Lin & Papaloizou, 1985). Given the fact that masses up to $10^{-2} M_{\odot}$ are believed to be dumped at once on the central object (corresponding to $\sim 10^{-4} M_{\odot} \text{ yr}^{-1}$, on average), the boosted optical and ultraviolet excess of the disk will easily outshine the central star, leading to the observed intense brightness variation. Furthermore, interactions of the infalling matter stream with either a magnetised disk or a strongly magnetised central star, launch a bipolar, high-velocity jet (cf. Königl & Pudritz, 2000; Shu et al., 2000) that also carries angular momentum outwards. A picture book example for such a disk-jet system has been imaged with the *Hubble Space Telescope* (Burrows et al., 1996), see Figure 1.13 (b). The physical processes of envelope infall, disk accretion and bipolar outstreams are schematically depicted in Figure 1.12.

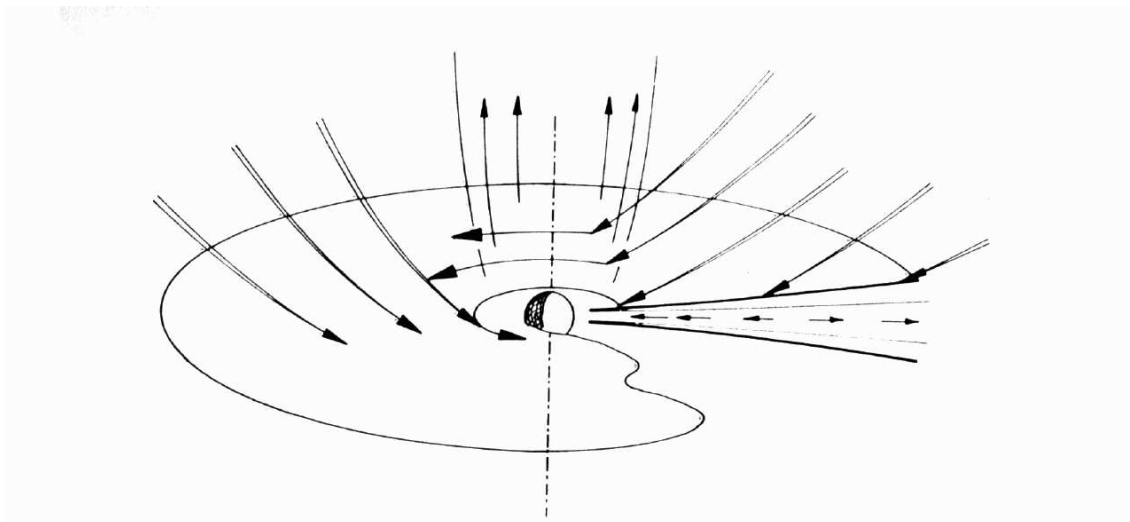


Figure 1.12. Schematic picture of stellar accretion processes. Angular momentum conservation results in a two-dimensional collapse solution. Infalling matter forms and constantly supplies a circumstellar disk; viscous processes transfer angular momentum outwards and mass is accreted onto the central star. At the same time, a considerable fraction of the accreted matter is ejected through as an energetic, bipolar wind or jet (cf. Königl & Pudritz, 2000; Shu et al., 2000, and references therein).

It is obvious that a full understanding of disk accretion requires a detailed knowledge of the dissipative processes at work. Unfortunately, the physics of the viscous transport processes is far from being completely apprehended. Up to now, any attempt to devise a general theory has proven to be elusive and inchoate.

Following an argument of Lynden-Bell & Pringle (1974), Hartmann (1998) considered two arbitrary, neighbouring rings in a Keplerian disk. In such a disk the inner annulus rotates faster than the adjacent, outer ring. Friction between the two annuli will try to bring them into corotation, i. e. to accelerate the outer ring and, obversely, decelerate the inner one. The net torque

results in a spin-up of the outer ring, that means angular momentum is transported outwards. The angular velocity of the inner annulus, on the other hand, is braked down, angular momentum is lost and material falls toward the centre. Accretion demands that the inward mass transfer has to be larger than the outward-bound. It has been demonstrated, however, that friction and shear in a gaseous disk are too slow to yield reasonable accretion rates (Frank et al., 1992). Several others mechanisms have been considered to save the day: turbulent convection in disks (Lin & Papaloizou, 1980), tidal forces induced by a companion star (Vishniac & Diamond, 1989), gravitational instabilities (Larson, 1984), and magnetic instabilities (Balbus & Hawley, 1991). At the moment, none of them fully satisfies observational findings and constraints. For the time being, viscous processes, and hence angular momentum transport, can only be parametrised.

1.3.2 Detection and observation

Evidence from our own solar system as well as theoretical considerations strongly argue for the existence of circumstellar disks around nascent stars. The observational verification of this picture, however, has not been delivered until recently. The advent of novel detector technology in conjunction with the commissioning of new telescope facilities, both on the ground and in space, has changed the situation, though. Today, the presence of disks around other stars is well confirmed by direct and indirect means. We will give a short account of those below.

Indirect identifications The first observationally-grounded evidences for the existence of circumstellar disks dates back to 1980. Optical jets and bipolar molecular outflows connected with young stellar objects suggested that the underlying geometry of star formation is axially symmetric (e. g. Mundt, 1985). Spectroscopic analysis of absorption and emission lines from YSO stellar winds reveal a systematic blueshift. It is interpreted as being the result of the existence of an opaque disk that occults the redshifted spectral feature of receding gas (Appenzeller et al., 1984; Hartmann & Calvet, 1995). Furthermore, polarisation measurements of young stellar objects point to a flattened circumstellar particle distribution (Elsässer & Staude, 1978). The powerful methods of optical/infrared photometry to discern excess emission and spectral energy distribution, have already been mentioned. While indirect methods remain very useful tools in obtaining statistical results and deriving general properties, direct observation is required to study individual disks in detail.

Direct observations On entering arcsecond or even subarcsec angular resolution, millimetre and submillimetre interferometry has become capable to detect the cool, dusty material that surrounds young stellar objects. Continuum-emission studies allow to trace the disks' density distributions as flattened structure of some tens to hundreds AU in size; line emission studies derive the corresponding velocity field, showing two separate, blue- and redshifted emission lobes (Wilner & Lay, 2000).

Strongest support and confirmation for the disk paradigm, however, comes from optical and near-infrared imaging. The first direct imaging of a circumstellar disk proved, later on, to be a mere stroke of luck: Smith & Terrile (1984) discovered an edge-on disk around the main-sequence star β Pictoris, see Figure 1.13 (a). It is a so-called debris disk; collision between and subsequent shattering of planetesimals provide a constant reservoir of circumstellar dust, that can be imaged in scattered light. Unfortunately, β Pictoris is an exceptional case; following surveys to find such disks around other nearby stars remained without any result (Kalas, 1996).

A breakthrough in direct imaging of circumstellar disks has been achieved after the *Hubble Space Telescope* became fully operational. Not hindered by the spoiling effects of the Earth's atmosphere, its angular resolution of 0.1 arcseconds or even below afforded unprecedented performances. Prime targets to look for circumstellar disks are, of course, nearby star formation regions like Taurus-Auriga (~ 150 pc), or the Orion Nebula at ~ 460 pc. Figures 1.13 (b) and (c) show two circumstellar disks found in the Taurus-Auriga region: The first, HH 30, represents a prototypical example of the disk-jet connection (Burrows et al., 1996). The disk, having an inclination of $\sim 7^\circ$ to the line of sight, is seen as the dark lane dividing the two concave reflection nebula as produced by the scattering of the light of the hidden central star. The vertical extension of the disk is increasing with radial distance, a fact known as flaring, and in agreement with theoretical models of the density distribution of circumstellar disks (Lynden-Bell & Pringle, 1974; Kenyon & Hartmann, 1987). Perpendicular to the disk a pulsed jet is emanating. The second circumstellar disk, IRAS 04302+2247, belongs to a very young source, still embedded in its natal molecular cloud (Padgett et al., 1999). Measuring the size of the disk is difficult because it is extending radially without any clear-cut edge until it finally merges with the dark background; however, the disk could be as large as 450 AU.

The ambiguity to define the disks' size is nicely suspended with those disks imaged in the Trapezium Cluster, the dense core of the Orion Nebula. Figures 1.13 (d)–(f) show three prominent examples of such disks (O'Dell & Wen, 1994; McCaughrean & O'Dell, 1996; Bally et al., 1998a). They come in two varieties: first, as dark, opaque features against the luminous background of the Orion H II region. Depending on their inclination to the line of sight, the central pre-main-sequence star is visible or not, cf. to (d) and (e), respectively. Second, circumstellar disks are found embedded in and surrounded by bright ionisation features, cf. (f). These objects, sometimes called “proplyds” attain their peculiar elongated, drop-like shape by the combined influence of both ultraviolet radiation and stellar wind coming from the hot, luminous stars at the centre of the cluster.⁶ The most satisfactory model for these objects involves photoionisation by stellar ultraviolet radiation, heating of the disk, and subsequent loss of disk material through evaporation (Henney & O'Dell, 1999); mass loss rates are of the order of 10^{-6} – $10^{-7} M_\odot \text{ yr}^{-1}$. A circumstellar disk comprising $0.01 M_\odot$, the so-called “minimum mass solar nebula”, is eaten up entirely after only a few thousands years. This small number sets firm constraints for the possible planetesimal/planet formation in the circumstellar disks. Any successful growth of circumstellar dust to larger bodies must be completed within that timescale before the circumstellar material will be dispersed. These severe conditions might be somewhat alleviated by the fact that some disk, viz. the ones seen in silhouette, are not exposed to strong ionisation because they lie far enough from the central OB stars and/or are shielded from dangerous ultraviolet flux. McCaughrean et al. (2000) discussed several possible mechanisms for the apparent truncation of the disks' outer edges: stellar UV flux and stellar winds, star/disk tidal interactions, and gas pressure effects.

1.3.3 Physical properties

Several interesting physical properties of circumstellar disks can be derived from observations and comparison with dedicated, theoretical models. The classic disk model of Shakura & Sunyaev (1973)—originally devised for black hole accretion disks—and reviewed by Pringle (1981) envis-

⁶In general, the curved cusps of the proplyds are facing toward θ^1 Ori C, an O7 main-sequence star (Conti & Alschuler, 1971), while the pointed tails are facing away from it; furthermore the proplyd surface brightness is decreasing with projected distance from θ^1 Ori C (McCullough et al., 1995).

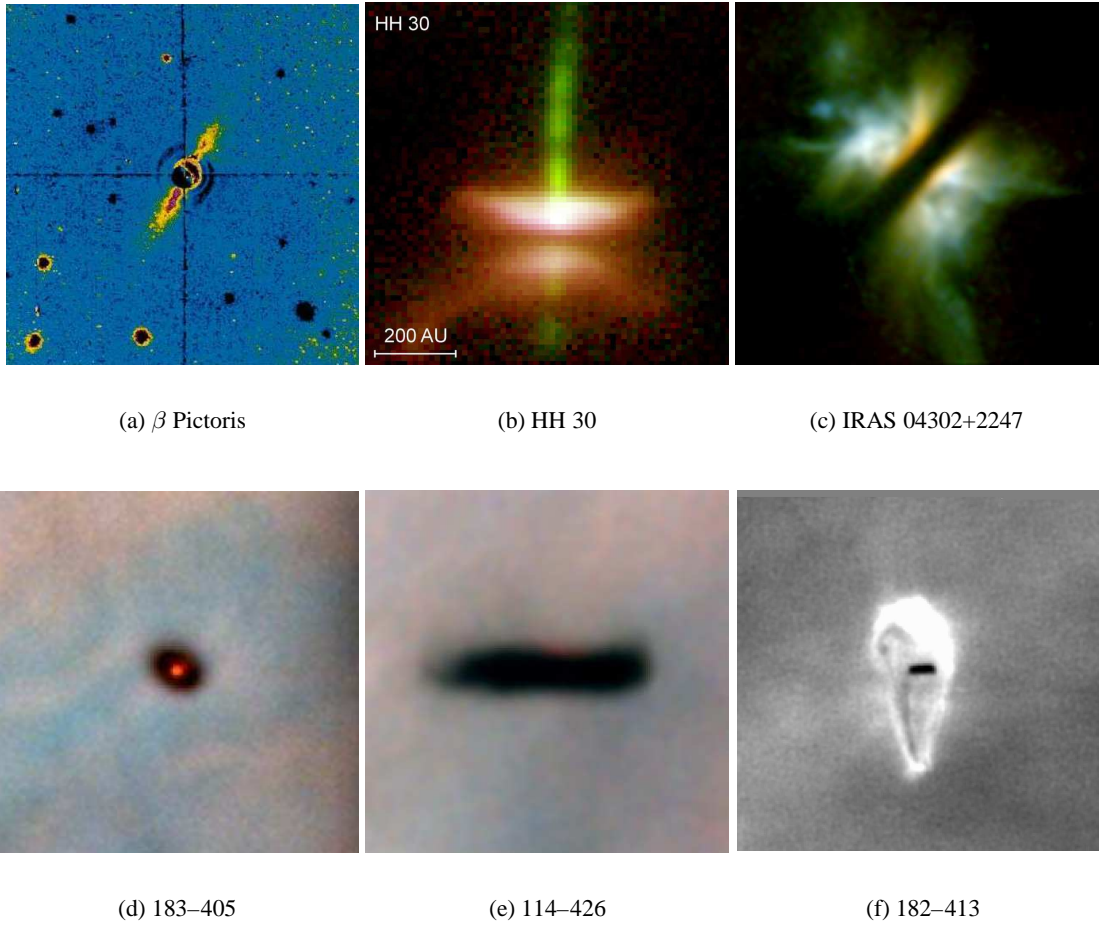


Figure 1.13. A gallery of circumstellar disks. Except for (a) all images have been taken by the *Hubble Space Telescope*, using the NICMOS instrument for (c), and the WFPC2 camera for (b) and (d)–(f). The corresponding disk diameters are approximately $\gtrsim 800$ AU, 450 AU, 900 AU, 250 AU, ~ 1000 AU (wavelength-dependent) and 150 AU, respectively. See text for a detailed description and the corresponding source.

ages a thin, massless disk in Keplerian rotation around the central star, hydrostatically supported and isothermal in the vertical direction. The derived axisymmetric density function in cylindrical coordinates, radius r and vertical height z , takes the form:

$$\rho(r, z) = \rho_0 \left(\frac{r}{r_0} \right)^\alpha \exp \left\{ -\frac{\pi}{4} \left[\frac{z}{H(r)} \right]^2 \right\}, \quad (1.12)$$

where ρ_0 is the midplane density at an arbitrary radius r_0 , and $H(r)$ the disk's scale height, that is its effective thickness. Basically, Equation 1.12 describes a radial decrease governed by a power-law, and a Gaussian density profile in the vertical direction. For the scale height a power-law ansatz is made:

$$H(r) = H_0 \left(\frac{r}{r_0} \right)^\beta. \quad (1.13)$$

For a flared disk we have $\beta > 0$, i. e. the disk's vertical dimension is increasing towards larger radii. As one always observes a two-dimensional projection of the intrinsically three-dimensional disk structure, it seems convenient and appropriate to introduce a surface density as follows:

$$\Sigma(r) = \int \rho(r, z) dz \propto \Sigma_0 \left(\frac{r}{r_0} \right)^p. \quad (1.14)$$

The three exponents α, β and p are not independent of one another, but connected by the relation $\alpha = p - \beta$. The set of standard values for these parameters is $\alpha = -15/8$, $\beta = 9/8$ and $p = -3/4$, respectively.

Together with the optical properties of the circumstellar dust, simple disk models can be generated by integrating along a grid of lines of sight (so-called ray-tracing) to obtain the effective light absorption. Including polarisation, multiple scattering, or dust particle size distributions complicates the calculations significantly. Comparing these with the actual observations permits, in principle, to derive the sought-after quantity.

Disk diameter It has already been demonstrated that the determination of disk sizes might have some difficulties. In fact, there might not be a definite size as such; rather it will depend on the wavelength range used for the observation. Accordingly, millimetre images of circumstellar disks are generally larger than their optical counterparts (Padgett & Stapelfeldt, 1999). Conversely McCaughrean et al. (1998) reported a small, but significant decrease in size between the optical and near-infrared images of the same circumstellar disk 114–426 as found in the Trapezium Cluster. Reduced extinction at longer wavelengths allows more background light to filter through the translucent edges of the disks; as a result the disk appears smaller when seen in near-infrared.

Inclination to the line of sight Random orientation of the disks in space will lead to different morphological appearances. A disk seen face-on will be circular in shape with the central star in the middle, one viewed edge-on as an elongated structure where the central star is blinded out; in general, circumstellar disk will be elliptical. The aspect ratio between the measured major and minor disk axis, a and b , can then be used to obtain the inclination of the disk to the line of sight via $\cos i = b/a$. However, there is a bias effect lurking, favouring edge-on systems because in many cases the bright central star will outshine the surrounding disk. Circumstellar disk without an illuminating emission nebula background, for example HH 30 or IRAS 04302+2247, probably would not have been discovered if they were to be less inclined. Another way to derive disk inclinations, especially for edge-on or near-edge systems, is to utilise the brightness asymmetry, if present, of the bipolar reflection nebulae above either side of the disk plane. The farside lobe will appear smaller and fainter than the nearside one; thus on comparing with a set of generated disk models one can accurately derive the disk inclination. A third method is applicable when the object in hand possesses a clearly visible jet. Starting from the assumption that the jet is perpendicular to the disk plane, one can fix the inclination independently.

Mass of the disk The determination of the mass of a circumstellar disk with decent precision is a subtle task. To estimate the mass of disk by the amount of circumstellar material absorbing the light of a central star or of a background illuminating source is thwarted by the huge optical depths of the disk at optical/near-infrared wavelengths. Already very little absorbing material can account for optical depths larger than unity, thereby rendering the disk opaque. Any mass estimate, therefore, sets only a lower limit, typically some $\sim 10^{-5} M_{\odot}$. Measuring dust continuum fluxes at millimetre wavelengths, however, allows to derive disk masses; the assumptions made are that the

emission comes from optically thin, isothermal dust (Natta et al., 2000).

Dust properties In the absence of more advanced information about the properties of circumstellar dust, many models use those of standard interstellar grains as templates. If all other parameters for the disk in question (mass, size, inclination etc.) have been determined by ancillary means, dust particle properties can also be taken into consideration. It is likely that dust undergoes significant alterations in circumstellar environments: changes in size, size distribution, geometrical shape and mineralogy. Some of these processes may leave traces in the scattered light. As an example, we consider the impact dust agglomeration⁷ to sizes much larger than the observation wavelengths might have on the extinction properties of the circumstellar material. If the grown aggregates are roughly spherical in shape, one would expect a flat extinction curve (Evans, 1994). More likely, however, dust grows to open, fluffy structures with fractal geometries (Ossenkopf, 1991). For these kind of aggregates “no dramatic changes in the optical properties due to coagulation can be expected” (Stognienko et al., 1995). To put it another way, what is seen are the building blocks of the aggregates, single dust grains; the larger entities as such do not betray their presence through modified optical properties (Wurm, 2001).

1.4 Planetesimal and planet formation

Often circumstellar disks are indiscriminately called protoplanetary disks. The idea behind that notion is the belief—and hope—that planetesimals, and from them planets, do form in dusty circumstellar environments; first by cohesive sticking of dust grains and later by gravitational attraction between larger bodies. One should bear in mind, however, that there are few stringent, direct evidences to endorse that hypothesis. To demonstrate or refute that growth of dust grains into larger aggregates and bodies is indeed taking place in circumstellar disks, is part of this thesis.

Luckily, there are indirect evidences: First, the testimony of own solar system, cf. Section 1.1. There is compelling observational knowledge to argue that other stars form in no other way than the Sun did, with disk formation as a perforce result of star formation process, see Section 1.2. Analogously to our solar system, planets will probably form in such circumstellar disks. Then, secondly, there are dust-rich debris disks produced by frequent collisions between fully-grown asteroids, whose orbits are probably being perturbed by massive planets (Grady et al., 2000).⁸ Last but not least, the many observed extrasolar planets proved that planet formation did indeed took place around other stars. Since the first discovery of an extrasolar planet around a solar-type star by Mayor & Queloz (1995), their number is ever increasing. As of the time of writing this thesis, around 100 such systems have been detected, most of them by the radial velocity technique. Other possible methods involve photometric monitoring of stars to detect transitory giant planets (Charbonneau et al., 2000), brightness amplifications due to microlensing events (Wambsganß, 1997; Sahu et al., 2001) or highly precise astrometric positioning; see Marcy & Butler (1998) for a detailed description.

To end this introductory chapter we will give a short, descriptive overview of planetesimal and planet formation theories. No attempt has been made to exhaust the subject matter.

⁷Some authors refer to the sticking of dust grains as coagulation. Strictly speaking, however, this term is only appropriate for processes that transform a liquid into a (semi-)solid mass, e. g. blood clotting.

⁸Interesting in this context is the detection of circumstellar dust disk around some stars with known planetary companions (Trilling et al., 2000).

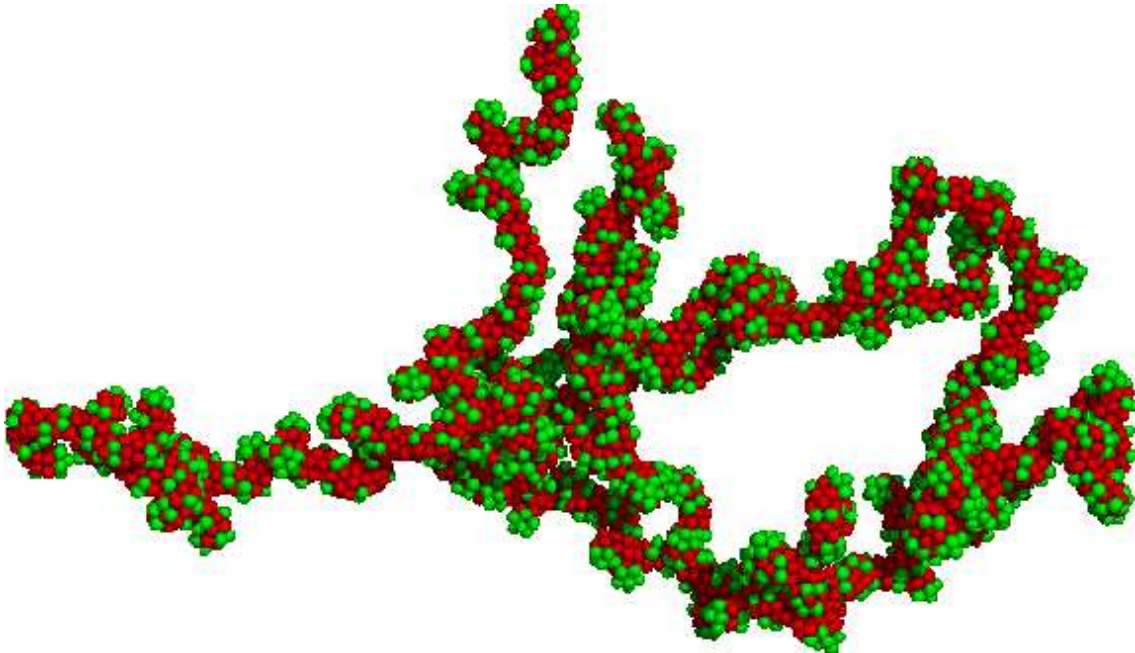


Figure 1.14. Computer-simulated fractal dust aggregate. The above picture shows the result of a fractal adhesion model for dust grains involving random conglomerates of spherical compounds of different properties, here artificially highlighted by different colours. Credit: E. L. Wright (UCLA, USA).

1.4.1 Assembly of large aggregates from dust grains

The recipe how to build up large bodies in a circumstellar disk is as yet beyond our ken. The ingredients, however, are well known: tiny, submicron-sized dust grains, condensed in the dense atmospheres of M giants during the late stages of their evolution (Jones, 1997). After formation the “stardust” is incorporated into the interstellar medium, and from there into molecular clouds; in Paragraph 1.2.1 we have seen how the collapse of cloud clumps is facilitated by the presence of dust. In the end, dust becomes a minor component of circumstellar material.

Dust sticking As the dust particles are suspended in the circumstellar gas, their motion is entirely controlled by the dynamics of the gas. Its velocity field, besides the overall Keplerian rotation, is probably to be highly turbulent (Stone et al., 2000). Therefore, dust particles will suffer frequent mutual collision. Provided that their relative velocity is not too high, the dust grain will stick together by cohesive (van der Waals) forces. Many repeated collision will, little by little, build up larger aggregates; computer simulations suggest that open, fractal geometries emerge (Ossenkopf, 1993). Fractal aggregates of dust grains are characterised by non-integer dimensions in the power-laws that relate mass and size, $m \propto r^{d_m}$, and cross-section and size, $\sigma \propto r^{d_\sigma}$, of the aggregates. Compact aggregates, on the other hand, have integer exponents with $d_m = 3$ and $d_\sigma = 2$, respectively. Figure 1.14 depicts a fractal dust aggregate as a result of modelled adhesion processes.

Settling and agglomeration Once the aggregates have grown to pebble sizes, they settle to the disk plane (Weidenschilling & Cuzzi, 1993). Larger particles settle faster than smaller, thereby sweeping up the slow stragglers. This leads to “run-away growth”: As the aggregates gain in

mass, it accelerates its descent towards the disk plane, thereby agglomerating more and more material. The resulting accumulation in the disk plane enhances mutual, inelastic collisions and further growth. In the end, the largest bodies grow to kilometre-sized object, so-called planetesimals. Of course, there also destructive processes at work. If the relative velocity of two colliding rocks exceeds a critical value, one or both of the objects disintegrates into a few pieces or is even shattered completely into a myriad of smaller fragments.

1.4.2 Planet formation

Formation of solid (terrestrial) planets Above a critical size of around 1–10 km the grown bodies decouple from the gas. At that stage, gravitational attraction between the planetesimals come into play (Safronov, 1969). As the most massive planetary embryos possess the largest gravitationally enhanced collisional cross-section, they provoke an intense bombardment of neighbouring objects. While their size and mass is steadily increasing disintegration becomes more and more unlikely; at the same time, the number of other growing objects in close vicinity is reduced by competitive accretion. The rapid increase in size of a few protoplanets is known as runaway accretion (Wetherill & Stewart, 1989; Kokubo & Ida, 1996). The result is a planetary oligarchy, where a few large objects represent almost all of the mass contained in solid bodies. The runaway phase of planet formation will abate by a shortage of accretable material leading to an isolated planet (Lissauer & Stewart, 1993). However, the duration of the runaway accretional stage might be significantly prolonged by inward migration of the protoplanet (Ward & Hahn, 1995). Figure 1.15 summarises what has been about the formation of solid planets.

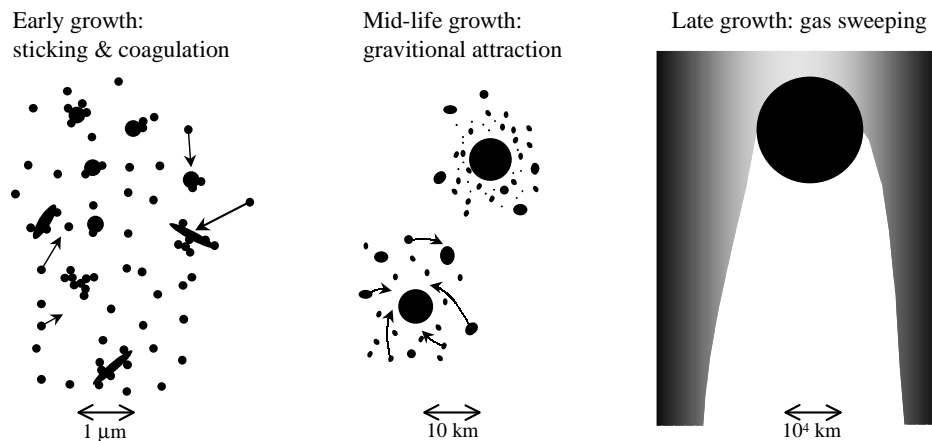


Figure 1.15. Sequence of events leading to the formation of a bona fide planet. *Left panel:* dust grain growth through cohesion and agglomeration. *Centre panel:* Growth of planetesimals by gravitationally induced collisions. *Right panel:* Collection of gas by sweeping and gravitational attraction. Taken from Beckwith et al. (2000).

Formation of giant planets Models of the interior of the solar system giant planets and observed gravitational potentials suggest the presence of a dense, rocky core at the centre of each of them, surrounded by vast atmosphere of mainly hydrogen and helium. There are currently two

different theoretical approaches to explain the formation of giant planets: First, nucleated instability, where the gas accretes onto a sufficiently heavy solid core, comprising roughly $10\text{--}20 M_{\text{E}}$. The second theory envisage a cold, massive circumstellar disk that becomes gravitationally unstable to collapse to planetary sizes (Boss, 1997). For a more elaborate description of giant planet formation and the physics involved the reader is referred to (Wuchterl et al., 2000).

Chapter 2

The Hubble Space Telescope

*T'as vu mes lunettes ? a demandé Clotaire à Agnan.
Maintenant, je vais être le premier en tout [...]*

SEMPÉ & GOSCINNY, *Le petit Nicolas et les copains*

The ground is a very unsuitable place for astronomical observations. The Earth's atmosphere obstructs essential parts of the electromagnetic spectrum: X-ray and ultraviolet radiation is blocked completely in the ionosphere and partly in the lower ozone layer. The infrared spectral range is heavily affected by water and carbon dioxide absorption in the stratosphere, and infrared observations can only take place in narrow spectral windows. Only visible light and radio waves pass the atmosphere unhindered. However, turbulence in the troposphere (the lowermost atmospheric layer) distorts incoming wavefronts, thus degrading the image of the astronomical target in question and limiting the performances attainable by ground-based telescopes.

The awareness of the degrading and limiting effects of the Earth's atmosphere led to the idea of putting a telescope in space to operate beyond that interference. The first concept for a satellite-borne observation facility were made in the 1940s. At that time, however, rocket technology was still in its infancy. Perhaps not surprisingly, it took many years to convince engineers of the feasibility of such a device, to gain support from the astronomical science community, and, of course, to get the necessary funding from government sources. Finally, a space telescope was designed and constructed in the 1970s and 80s. Originally planned to start operation in the mid-1980s, but delayed by the Challenger accident, the *Hubble Space Telescope* (HST) was deployed into orbit in April 1990. Unfortunately, a significant spherical aberration in the 2.4-m primary mirror was discovered shortly after the first observations. A corrective optics system was installed three years later, regaining the predicted performance of the telescope. As of June 2002, four servicing and refurbishment mission have been completed, installing new science instruments and maintaining the telescope as a whole. Figure 2.1 shows a cut-away view of the telescope indicating major science instruments and components. The *Hubble Space Telescope* is scheduled to be decommissioned around 2010. At the same time, the *Next Generation Space Telescope* (NGST) is expected to become its successor.

In the following sections we will briefly introduce the three science instruments that provided data for this project. We will limit ourselves to those facts and figures that have immediate relevance for our work. A full description of the instruments on-board the *Hubble Space Telescope* can

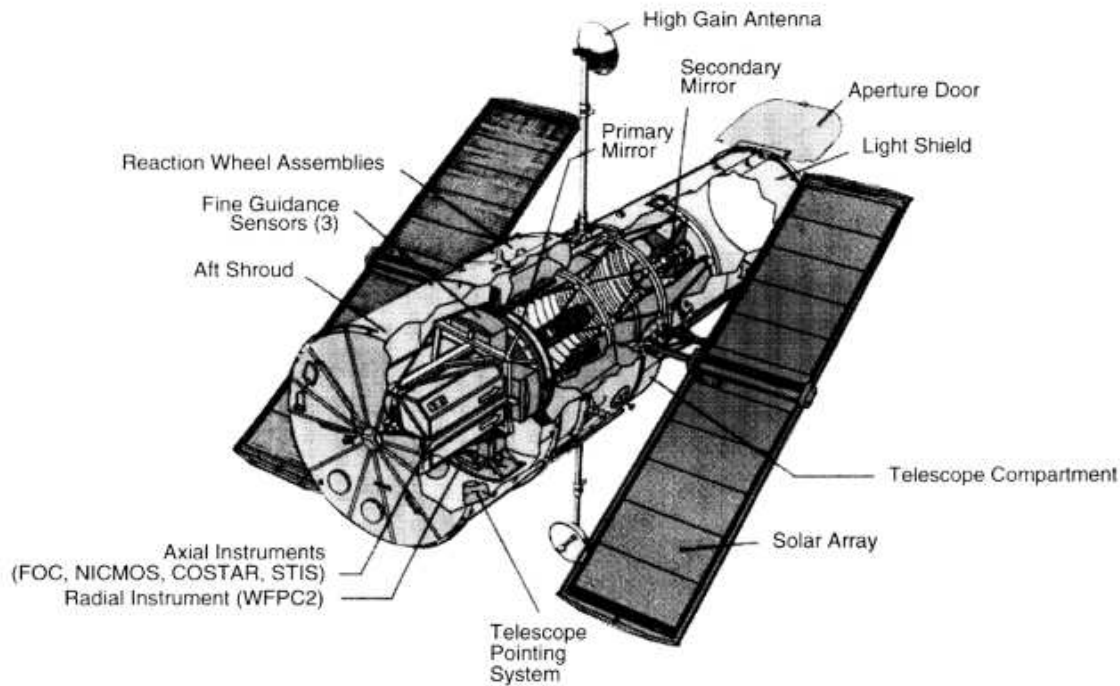


Figure 2.1. Technical overview of the *Hubble Space Telescope* prior to March 2002, when the Faint Object Camera (FOC) was replaced by the Advanced Camera for Surveys (ACS). All scientific instruments are mounted in axial or radial bays behind the 2.4-m primary mirror.

be found in the corresponding instrument handbooks (see Biretta et al. 2000; Leitherer et al. 2000; Schultz et al. 2001, and newer version thereof).

2.1 Wide Field and Planetary Camera 2

The Wide Field and Planetary Camera 2 (WFPC2) is a two-dimensional charge coupled imaging device that works in the wavelength range 120 to 1100 nm. It was installed during the first servicing mission in 1993 to replace the Wide Field Planetary Camera (WF/PC), that was affected by the flawed primary mirror. WFPC2 has a built-in corrective optics to counter the spherical aberration of the primary mirror. In a future servicing mission, WFPC2 will be replaced by the Wide Field Camera 3 (WFC3), equipped with two $2k \times 4k$ CCD detectors designed to operate from 200 nm to 1800 nm.

The WFPC2 field of view is located at the centre of the HST focal plane. A faceted mirror in the optical train splits the image of the sky in four parts to project each of them onto a charge coupled device (CCD). These detectors have 800×800 pixel each. While the three Wide Field (WF) camera channels are identical in design and produce a focal ratio of $f/12.9$, the Planetary Camera (PC) has a smaller field of view and a focal ratio of $f/28.3$. Table 2.1 summarises their characteristics. For a detailed assessment of the on-orbit and photometric performance of WFPC2, see the reports of Trauger et al. (1994) and Holtzman et al. (1995).

Table 2.1. Characteristics of the WFPC2 cameras

Camera	Pixels	Field of view [arcsec ²]	Pixel scale [arcsec]	<i>f</i> -ratio
PC	800 × 800	36 × 36	0.0455	28.3
WF2, WF3, WF4	800 × 800	80 × 80	0.0996	12.9

Undersampling The WFPC2 wide field cameras can not take full advantage of the diffraction-limited resolution because their pixels are too large in comparison to the point spread function (PSF) of the telescope optics. At 500 nm, for example, the PSF has a full-width at half-maximum of about 50 milliarcsec, half the size of a WF pixel. Detector pixels that are not small compared to the PSF sample the image insufficiently in the spatial domain. The result is a loss of spatial information. Although the pixels of the Planetary Camera are about a factor of two smaller than the WF pixels, they still do not sample the PSF optimally over the whole of its spectral range. The situation is somewhat alleviated at longer wavelengths because the width of the PSF increases linearly with wavelength.

It is possible to recover some of the lost spatial information by image dithering (Fruchter & Hook, 1997), i. e. taking several exposures of one and the same target with non-integer pixel offsets between them. Each of the pixels of a detector can be envisaged as sampling the “true” image of the object convolved with the telescope PSF and the pixel-response function of the detector. To approximate the “true” image as well as possible, the number of sampling points has to be increased. Taking different exposures at non-integer pixel offsets augments the number of sample points, and improves the spatial information. A dedicated method for the linear reconstruction of images from undersampled, dithered data has been developed by Fruchter & Hook (2002). The principle of the drizzle method is explained in Section 3.2.2.

2.2 Space Telescope Imaging Spectrograph

The Space Telescope Imaging Spectrograph (STIS) was installed during the second servicing mission to the *Hubble Space Telescope* in February 1997. It is a versatile instrument enabling both spectroscopy and imaging in the ultraviolet to near-infrared wavelength range. STIS is equipped with first-order gratings for low to medium resolution ($R \approx 400\text{--}14\,000$) long-slit spectroscopy, and with echelle gratings for medium to high spectral resolution ($R \approx 23\,500\text{--}100\,000$) in the ultraviolet. A detailed overview of the STIS imaging and spectroscopy performance is provided by Bowers et al. (1997) and Kimble et al. (1997).

STIS possesses three detectors, with 1024×1024 pixel each. Two of them are so-called Multi-Anode Microchannel Arrays (MAMA), photon-counting devices sensitive in the near-ultraviolet spectral range; the third is a CCD detector operating from the ultraviolet up to the near-infrared. Their principal parameters are listed in Table 2.2.

As for undersampling, the situation is comparable to what has been said about the Planetary Camera. With a scale of 50.7 milliarcsec/pixel STIS also undersamples the PSF slightly, especially in the ultraviolet where the PSF width is small. Again dithering techniques must be applied to increase image sampling and spatial resolution.

Table 2.2. Detector specifications for the STIS instrument

Detector	Pixels	Field of view [arcsec ²]	Pixel scale [arcsec]	Wavelength range [nm]
CCD	1024 × 1024	51 × 51	0.0507	~200–1100
NUV-MAMA	1024 × 1024	25 × 25	0.0246	165–310
FUV-MAMA	1024 × 1024	25 × 25	0.0246	115–170

2.3 Near Infrared Camera and Multi-Object Spectrograph

The Near Infrared Camera and Multi-Object Spectrograph (NICMOS) was installed along with STIS during the second servicing mission. After the initial coolant supply was prematurely exhausted in 1999, NICMOS was dormant for three years. It has been recently revived with the installation of a new cooling system.

NICMOS provides several imaging capabilities (narrow and broad-band imaging, imaging polarimetry, coronagraphic imaging), but also allows slitless grism spectroscopy from 0.8 to 2.5 μm . It possesses three adjacent cameras, each equipped with a 256×256 pixel array, that can work independently and simultaneously. Each camera has a different focal ratio, hence a different field of view, cf. Table 2.3.

Table 2.3. Basic imaging parameters of the NICMOS cameras

	Camera 1 (NIC 1)	Camera 2 (NIC 2)	Camera 3 (NIC 3)
Pixels	256×256	256×256	256×256
Field of view [arcsec ²]	11×11	19.2×19.2	51.2×51.2
Pixel scale [arcsec]	0.043	0.075	0.2
<i>f</i> -ratio	<i>f</i> /80	<i>f</i> /45.7	<i>f</i> /17.2
Diffraction limited wavelength [μm]	1.0	1.75	—

2.4 Filter elements used

The above instruments provide a multitude of possible filters and other optical elements: narrow band emission line filters, broad-band photometric filters, polarisation filters and coronographic masks. In the following Table 2.4 we list only those filters relevant for the data of this work.

Table 2.4. Set of filter elements used

Instrument	Filter name	Spectral feature or band	Central wavelength [\AA]	Width [\AA]
WFPC2	F502N	[O III]	5012	26.9
	F631N	[O I]	6306	30.9
	F656N	H α	6564	21.5
	F658N	[N II]	6591	28.5
	F673N	[S II]	6732	47.2
STIS	F28X50OII	[O II]	3740	80
	F28X50OIII	[O III]	5007	5
NICMOS	F187N	Pa α	18700	\sim 190

Chapter 3

Data: reduction and analysis

Measurement began our might [...]

W. B. YEATS, in ‘Under Ben Bulben’

3.1 Data stock

To perform a multi-wavelength analysis of the circumstellar disks in Orion’s Trapezium Cluster several different *Hubble Space Telescope* observation programmes have been compiled and processed to set up a dedicated, uniform set of data. All data is non-proprietary, i. e. accessible and ready for download from special data archives.¹ Upon retrieval of the data sets several calibration and reduction procedures were executed automatically by a so-called pipeline to facilitate subsequent analysis by the user. Table 3.1 shows the observation programmes that have been retrieved from the HST data archive.

Table 3.1. HST observation programmes analysed

Proposal number	Title	Principal Investigator	Prime instrument(s)
5085	Turbulence in H II regions	O’Dell	WFPC2
5469	Externally illuminated proto-stellar disks and naked jets	Bally	WFPC2
6603	Probing protoplanetary disks in the Orion Nebula	Bally	WFPC2
7367	Multi-wavelength imaging of circumstellar disks in the Orion Nebula	McCaughrean	STIS NICMOS

¹Based on observations made with the NASA/ESA Hubble Space Telescope, obtained from the data archive at the Space Telescope Institute. STScI is operated by the association of Universities for Research in Astronomy, Inc. under the NASA contract NAS 5-26555.

Several other HST observation programmes concerning circumstellar disk in the Orion Nebula could not be considered in this work. Either because the corresponding data is not yet publicly available, or the programmes are still in their implementation/scheduling phase and flight execution is pending.

In addition, photometric data of the Trapezium Cluster taken with VLT/ISAAC was included to determine the masses of central stars and to link them to the properties of their circumstellar disk.

3.2 Data reduction

3.2.1 Cosmic ray removal

CCD arrays are very sensitive to cosmic rays and protons coming from the Earth’s radiation belt or extraterrestrial sources. Cosmic ray fluxes vary due to a number of factors, e. g. solar activity, geomagnetic activity, and position with respect to the South Atlantic Anomaly. The average rate for HST detectors is about $1.2 \text{ cm}^{-2} \text{ s}^{-1}$, with peak-to-peak variations of around 60%. The impacts of such high-energy particles onto the CCD chip deposit large quantities of charge carriers in one or, more probable, several pixels. The induced charge is read out by the detector electronics and can spuriously mimic real astronomical objects.

This situation is aggravated by the fact that all CCD detectors on-board HST do undersample, to a larger or lesser extent, the telescope’s PSF. As a result, it is difficult to separate low-energy cosmic rays from faint stellar sources. Since cosmic rays accumulate with time, thereby increasingly contaminating the image, long observations have to be split into several co-aligned exposures to identify cosmic rays. The probability that one and the same pixel is struck repeatedly in subsequent exposures is decreasing with the number of exposures. Comparison between the co-aligned images can therefore identify and remove cosmic rays.

For most of the science images of this project cosmic ray removal was already performed by the automatic HST data reduction pipeline. For the remaining cosmic ray affected science images cosmic rays were removed using the IRAF² task `crrej` to ensure “clean” data for further analysis.

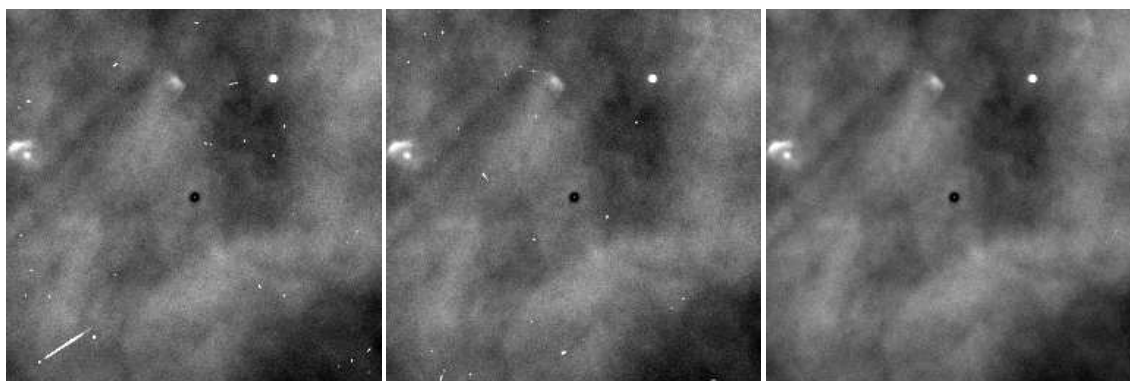


Figure 3.1. Example for cosmic ray removal. The images on the left and in the centre show two subsequent 160 s exposures taken with the $H\alpha$ narrow-band filter. Cosmic rays are discernible as bright points or streaks. The combined, cosmic ray removed image is shown on the right.

²IRAF is distributed by the National Optical Astronomy Observatories, which are operated by the Association of Universities for Research in Astronomy, Inc., under cooperative agreement with the National Science Foundation.

3.2.2 Image dithering

The concept of dithering and the drizzle algorithm have already been mentioned in Chapter 2 while discussing the problem of undersampling and a possible way to its relief. In many cases dithering provides considerable benefits to the observations. A higher-resolution image can be reconstructed from a set of exposures taken at non-integer offsets. Furthermore, small scale detector defects such as hot pixels and charge traps can be identified. However, the application of dithering has got some drawbacks which should be taken into account: First of all, more observation and spacecraft overhead time are necessary to get dithered imaging data. This might be unwanted as it reduces the number of targets or the area of sky observed. Second, the image processing becomes more intricate than for non-dithered data. Up to now there is no automatic pipeline that would process a final science image from a number of dithered exposures in an uncomplex manner.

Principle of the drizzle algorithm The principle of the drizzle algorithm is straightforward, cf. Figure 3.2. The pixels of the original, dithered images are mapped onto a finer grid of smaller pixels. The shifts between the dithered images and possible rotations³ as well as distortions across the detector camera are taken into account. To avoid that the input images “imprints” their pixel sampling onto the finer grid, the size of the original pixels is reduced. These then are mapped upon the subsampled final image. The flux value of each of the input pixels is redistributed to several other, smaller pixels as weighed by their corresponding overlap. For a detailed description the reader is referred to Fruchter & Hook (1997, 2002).

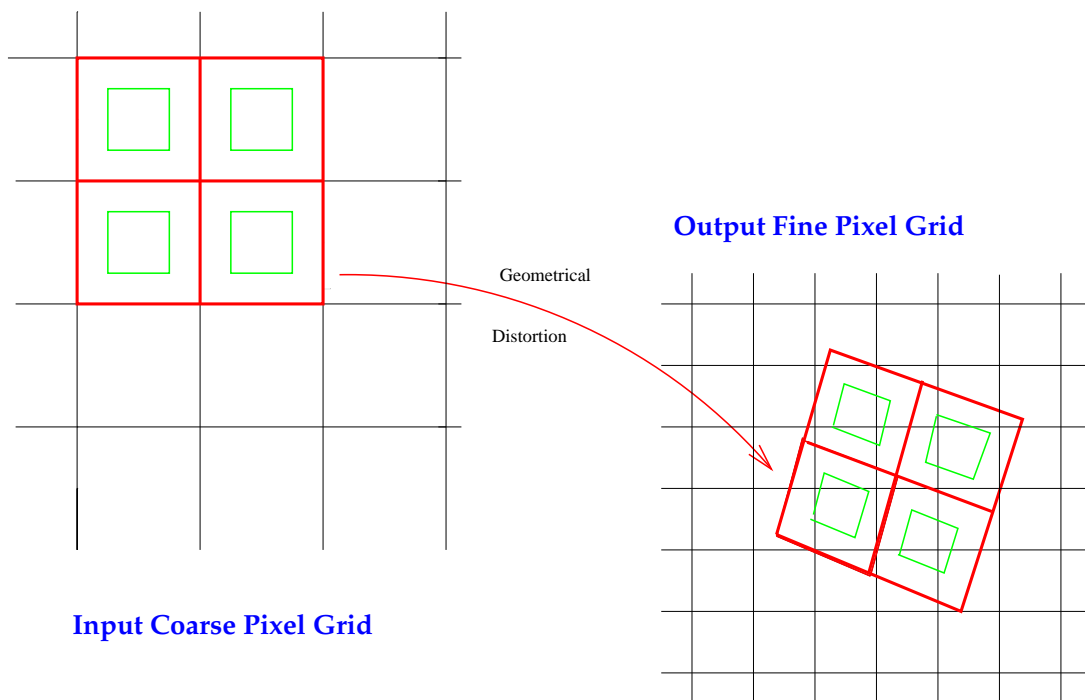


Figure 3.2. Schematic representation of the drizzle algorithm. Taken from Fruchter & Hook (1997).

³Rotations between subsequently taken images are normally small; only for very long exposure times rotations are introduced by the telescope’s motion along its 97-min orbit around the Earth.

The data of this project contains dithered images for the observation programmes 6603 and 7367, see Table 3.1. The pixel size of the subsampled output images was set to one half of the original pixel size throughout. Correspondingly, the pixel scales given in Tables 2.1 and 2.2 have to be halved. The improvement in spatial resolution of the final, subsampled images is about 20% (Bally et al., 2000).

3.2.3 PSF deconvolution

The limiting factors of obtaining high angular resolution images with a given instrument are mirror size, telescope optics, atmospheric turbulence and other effects that adversely influence the image quality. All together they determine the final point spread function of a telescope. The *Hubble Space Telescope* is placed high above all interfering atmospheric effects. Its PSF is determined by the telescope aperture, internal reflexions and scattering along the optical train, detector-specific obscuration patterns and filter throughputs. Since there is no atmosphere the PSF is very stable when compared to ground-based instruments (Holtzman et al., 1995).

Consider an ideal image with perfect point sources. The observed image will be a blending of the infinitely sharp input image with the finite PSF of the telescope including the detector response function. As a result, the flux contained in delta-peaks is redistributed over a larger area, reducing the contrast of the final images and leading to a loss of spatial resolution. The relation between the sought-after, ideal image I and the recorded one D can be expressed mathematically as a convolution of I with the PSF kernel:

$$D(x, y) = \int \text{PSF}(x', y'; x, y) I(x', y') dx' dy'. \quad (3.1)$$

Generally D is sampled at discrete points as for instance realised by a CCD array; one measures a flux $D_{ij} \equiv D(x_i, y_j)$ for each of the pixels (x_i, y_j) . In addition the measurements will be affected by detector noise $\varepsilon_{ij} \equiv \varepsilon(x_i, y_j)$. Equation 3.1 changes into a discretised convolution with an additional noise term:

$$D_{ij} = \int \text{PSF}_{ij}(x', y') I(x', y') dx' dy' + \varepsilon_{ij}. \quad (3.2)$$

Having knowledge of the exact PSF for all pixels (x_i, y_i) one can try to solve the integral equation 3.2 by numerical means. Since it is an inverse problem its solution will be not unique for most cases. However, a number of algorithms have been devised to do image restoration by PSF deconvolution. Well known examples are the so-called Richardson-Lucy deconvolution (Richardson, 1972; Lucy, 1974), and the maximum-entropy method (Narayan & Nityananda, 1986). All these methods have in common that they are nonlinear, i. e. they are rather sensitive to error, and iterative in the sense that the final solution is hopefully obtained after a number of runs.

What renders these algorithms especially inappropriate for PSF deconvolution of images of circumstellar disks is the fact that their performances is best for bright, high signal-to-noise objects and, in turn, poorer in regions of lower signal-to-noise. McCaughrean & O'Dell (1996) tested several standard deconvolution algorithms for images of circumstellar disks and found a strong dependence on the parameters chosen. The deconvoluted images obtained by application of these methods are therefore not very trustworthy and other possible ways have to be considered.

To achieve reliable PSF deconvolution results for the circumstellar disks a different approach was taken. The method of subtractive optimally localised averages (SOLA hereafter) was orig-

inally developed for helioseismological data (Pijpers & Thompson, 1992, 1994) but is also applicable for image reconstruction (Pijpers, 1999). The most striking advantages of the SOLA method are its linearity and non-iterativeness. PSF subtraction was therefore performed applying this method.

SOLA method Instead of operating on the recorded science image, the SOLA method uses only the PSF with which the image was taken. From there and a user-defined “target” PSF, a linear transformation between the actual science image and the corresponding deconvolved image is calculated. The final resolution that can be attained is limited by the sampling of the of the original, PSF convolved image. The algorithm ensures that photometric and astrometric information is preserved. For an in-depth description of the SOLA method, explaining the steps of the algorithm, see (Pijpers, 1999). The input PSFs have been generated by TinyTIM, an HST PSF simulator presented in Krist (1993, 1995). The used instrument, detector, filter, position of the object and, for NICMOS data, the observation date were taken into account to simulate a corresponding point spread function.

Reliability tests Several tests were made to check the reliability of the SOLA PSF deconvolution method. The algorithm proves to increase the spatial resolution of the images while maintaining their photometric information. An example test result is depicted in Figures 3.3 and 3.4. See caption for a description of the test procedures done.

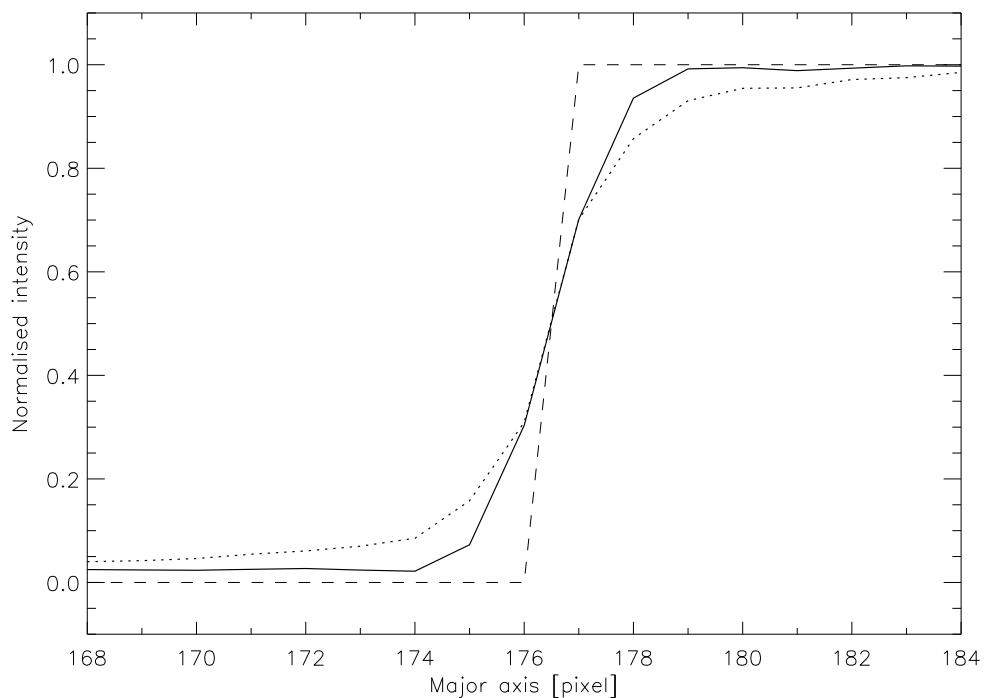


Figure 3.3. Enhancement of spatial resolution by PSF deconvolution. The curves show intensity profiles for cuts along the major axis of the images shown in Figure 3.4. The dashed curve shows the sharp, right-hand side edge of the original image. The dotted line shows the shallowing after PSF convolution and noise addition. The solid corresponds to the SOLA deconvolved image, clearly illustrating the increase in spatial resolution.

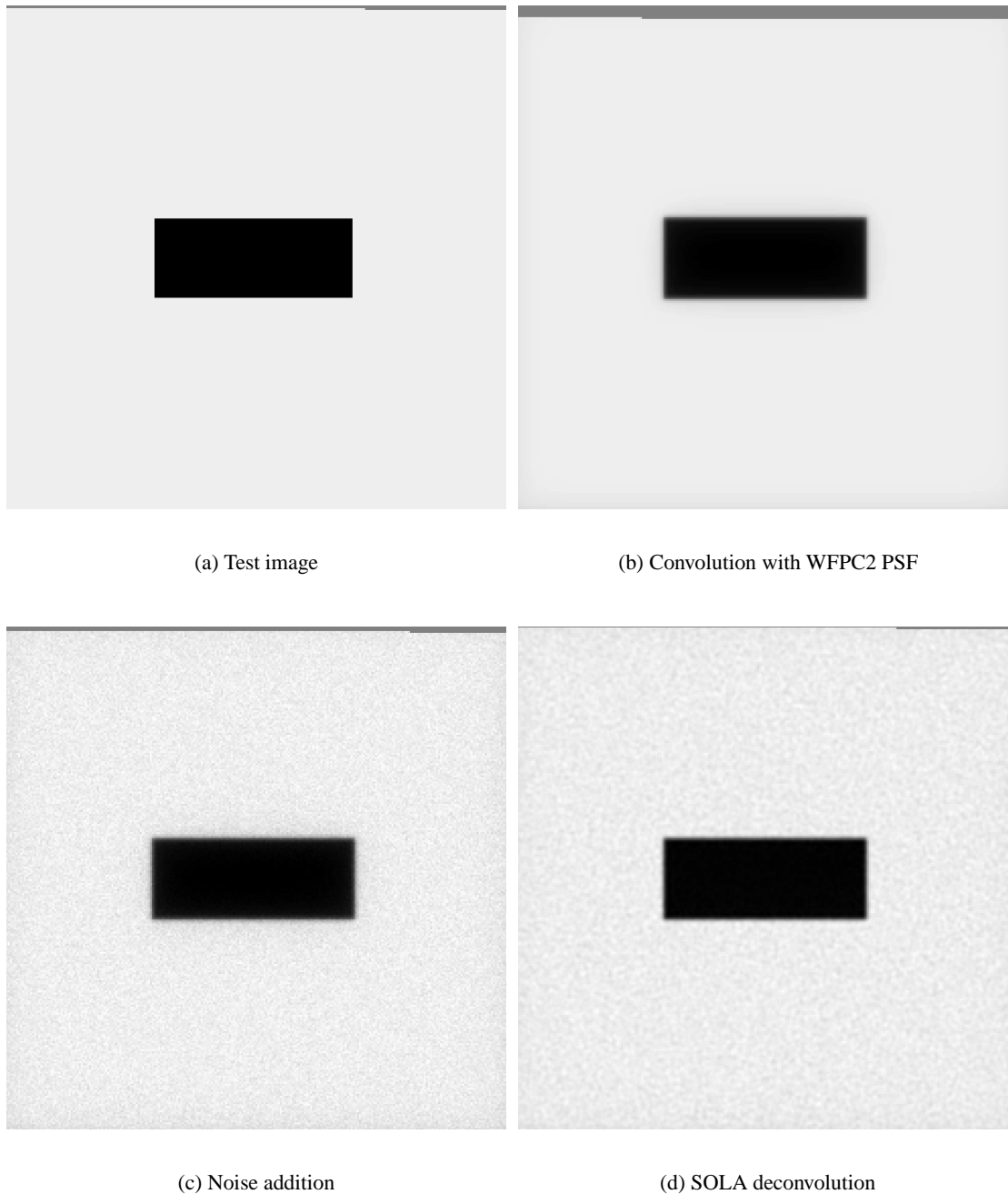


Figure 3.4. Representation of the effects of PSF convolution, noise addition, and PSF deconvolution using the SOLA algorithm. (a) Artificial image showing a 100×40 dark “disk” within a 256×256 region of uniform brightness. The edges of the dark region are infinitely sharp. (b) Convolution of the original image with a WFPC2 PSF. Spatial resolution is lost due to smoothing by the PSF. (c) Addition of Gaussian readout noise and Poissonian photon noise to the PSF convoluted image, resulting in a granulous appearance of the image. (d) Deconvolution of the noisy image using the SOLA algorithm. The edges of the dark region become sharper, i. e. spatial resolution was partially recovered. All images are displayed with the same intensity scaling.

3.3 Data analysis

3.3.1 Search for new silhouette disks

As a first step of the data analysis, all images were searched for new, uncatalogued circumstellar disk seen in silhouette against the bright background nebulosity. None was found serendipitously, so the sample of silhouette disks comprises 15 objects as given by Bally et al. (2000), cf. Table 3.2. There are several reasons for this failure. First of all, the entire data of this project is archival, that means it was already analysed and looked over by the Principal Investigators of the corresponding observation programmes, cf. Table 3.1. The first circumstellar disk seen against the bright nebular background of the Orion Nebula was discovered by O'Dell & Wen (1994). Subsequently, six new dark disks were found by O'Dell & Wong (1996). Bally et al. (2000) reported the discovery of 8 other silhouette disk.

To be seen, a silhouette disk has to be larger than about 50 AU, must have a sufficient contrast against the nebulosity, and must possess a faint central star. The image of a disk must extend over at least two or three pixels to be safely detected. This corresponds to approximately 40–60 AU at 460 pc when observed with the WFPC2 Planetary Camera. Indeed there is an obvious deficiency of objects smaller than 100 AU, cf. Table 3.4. To stand out distinctly against the intense nebular light, the optical depth of the circumstellar material must be larger than one. This condition is easily fulfilled by the presence of dust grains in the circumstellar material. Even for small amounts, their huge opacity efficiently blocks background nebulosity, and renders the disk opaque. The measured inclinations i to the line of sight of Table 3.2 demonstrate that the majority of the disks seen have inclination angles greater than 60° . This geometry favours the detection of a silhouette disk because much of the central star is obscured.

Table 3.2. Catalogue of disk seen in silhouette. Adapted from Bally et al. (2000).

Disk name	Right ascension			Declination			P.A. [°]	i [°]	Dimension [arcsec ²]
	h	m	s	°	'	"			
114-426	5	35	11.35	−5	24	26.4	29	> 85	2.7×0.7
121-1925	5	35	12.10	−5	19	25.0	118	51	0.8×0.5
132-1832	5	35	13.21	−5	18	32.3	55	75	1.5×0.3
163-026	5	35	16.29	−5	20	25.9	159	> 78	0.8×0.2
165-254	5	35	16.54	−5	22	53.8	4	> 71	0.3×0.1
167-231	5	35	16.73	−5	22	31.4	face-on	< 30	0.5×0.5
172-028	5	35	17.22	−5	20	28.1	140	55	0.7×0.4
182-332	5	35	18.18	−5	23	31.5	0	60	0.3×0.1
183-405	5	35	18.33	−5	24	04.9	43	39	0.7×0.5
191-232	5	35	19.13	−5	22	31.7	168	65	0.3×0.1
203-506	5	35	20.30	−5	25	05.7	16	67	0.4×0.2
218-354	5	35	21.79	−5	23	53.9	72	65	1.4×0.6
218-529	5	35	21.82	−5	25	28.7	176	60	0.4×0.2
239-334	5	35	23.86	−5	23	34.1	17	66	0.5×0.2
294-606	5	35	29.38	−5	26	06.3	86	> 85	1.0×0.25

Ionised disks In addition to silhouette disks that are dark in all emission line filters ($H\alpha$, [N II], [O III]), a greater number of disks are embedded within bright ionisation features. O’Dell et al. (1993) introduced the term “proplyds” for these objects. Figure 1.13 (f) shows an example of such an object. The visibility of a dark disk within a bright ionised envelope depends crucially on the location of the objects with respect to the star θ^1 Ori C, the main source of ionising radiation in the Trapezium Cluster. The known ionised disks are listed in Table 3.3

Table 3.3. Catalogue of ionised disks. Adapted from Bally et al. (2000).

Disk name	Right ascension			Declination			P.A. [°]
	h	m	s	°	'	"	
072-135	5	35	07.21	−5	21	34.5	108
109-327	5	35	10.94	−5	23	26.6	160
109-247	5	35	10.91	−5	22	46.5	
117-352	5	35	11.73	−5	23	51.8	50
135-220	5	35	13.51	−5	22	20.3	
141-301	5	35	14.14	−5	23	01.2	172
141-520	5	35	14.05	−5	25	20.4	face-on
143-522	5	35	14.33	−5	25	22.3	
147-323	5	35	14.73	−5	23	23.1	
154-240	5	35	15.38	−5	22	40.1	100
155-338	5	35	15.51	−5	23	37.5	face-on
158-326	5	35	15.78	−5	23	26.5	
158-327	5	35	15.83	−5	23	25.6	
159-418	5	35	15.90	−5	24	17.9	face-on
161-328	5	35	16.07	−5	23	27.9	
163-222	5	35	16.30	−5	22	21.7	
170-249	5	35	16.96	−5	22	48.8	
171-340	5	35	17.07	−5	23	39.8	
174-236	5	35	17.35	−5	22	36.2	57
175-355	5	35	17.54	−5	23	55.2	
176-543	5	35	17.55	−5	25	42.6	32
177-541	5	35	17.72	−5	25	40.6	
177-341	5	35	17.67	−5	23	40.9	105
179-353	5	35	17.94	−5	23	53.4	145
181-247	5	35	18.08	−5	22	47.3	165
182-413	5	35	18.21	−5	24	13.4	86
183-420	5	35	18.31	−5	24	20.0	70
197-427	5	35	19.66	−5	24	26.8	face-on
203-504	5	35	20.26	−5	25	04.2	20
205-421	5	35	20.52	−5	24	21.0	70
206-446	5	35	20.62	−5	24	46.5	80
244-440	5	35	24.42	−5	24	40.0	20
252-457	5	35	25.18	−5	24	57.44	160

3.3.2 Measurement of disk sizes

In total there are 48 objects where a circumstellar disk is clearly visible.⁴ Images with the highest spatial resolution and the best signal-to-noise were used to measure disk sizes, and to set up a size distribution of the circumstellar disk population in the Trapezium Cluster.

For this purpose, the linear extension along the disks' major axis was measured. The length of the disk was defined as the distance between the two opposite points where the background nebular light is attenuated to half of its original value (half-light diameter). The length in pixels was transformed into an angular diameter by multiplication with the appropriate pixel scale (cf. Tables 2.1 and 2.2), taking into account the two times smaller pixel scales of our dithered images (see 3.2.2). For most of the resolved disks the major axis diameter is smaller than 1'', unresolvable for most ground-based telescopes. To get the actual physical size of a circumstellar disk its angular diameter was multiplied by the distance to the Orion Nebula. A distance of 460 pc is assumed throughout (Bally et al., 2000, and references therein). The obtained disk diameters are summarised in Table 3.4.

Where available, Planetary Camera images were preferred over those taken with the Wide Field Cameras because they offer a better spatial resolution. Silhouette disks are dark in all emission line filters, i. e. their circumstellar material exhibit little or no ionisation. In principle, any of the emission line filters listed in Table 2.4 could be used to measure the linear dimension of the circumstellar disks. However, the signal-to-noise of H α images is generally higher than for other emission line filters, resulting in an enhanced contrast between dark disk and bright nebulosity. In the case of ionised disks contrast tends to better when seen in the [O III] emission line filter. Unfortunately, not all objects of Table 3.3 were imaged in this filter; in this case the H α filter was used. Location of the disks' outer edges was sometimes difficult because the disk was outshone by the bright, ionisation envelope.

3.3.3 Intensity profiles at different wavelengths

In the next analysis step full use of the multi-wavelength data was made. The existing observation programmes imaged many of the known circumstellar disks with different instruments and in various filters at different wavelengths. Through a combination of STIS, WFPC2 and NICMOS data, the spectral range from the near-ultraviolet to near-infrared is covered. The multi-wavelength information can be utilised to probe the properties of circumstellar dust in the disks' outer edges.

Only those disks were included into the analysis that were imaged in at least three of the following emission line filters: [O II] λ 3727 Å, [O III] λ 5007 Å, and H α λ 6563 Å. Thereby a minimal wavelength coverage was set up to capture reliably any wavelength dependencies. The two first filters belong to the STIS instrument, while H α is a WFPC2 filter. In addition, we concentrated on larger disks, where sufficient spatial structure was resolved, and on data with excellent signal-to-noise. The such restricted sample contains 5 circumstellar disks. Only one of them is an ionised disk (182-413), reflecting the fact that they are generally smaller in size (cf. Table 3.4). Furthermore, the measurement of their size is affected by the bright envelope. Only two disks were imaged in the Pa α λ 1.876 μ m filter using NICMOS (114-426, 218-354).

⁴Recently, O'Dell (2001) discovered two more such objects in the outer parts of the Orion Nebula. One silhouette disk (321-602) with an apparent size of around $0.5'' \times 0.1''$, and one ionised disk (093-822) having a diameter of $2.0''$.

Table 3.4. Diameters of silhouette and ionised disks

Disk	Detector	Filter	Dithered image	Size [pixel]	Diameter [AU]
114-426	PC	H α	yes	95	990
121-1925	PC	H α	yes	20	210
132-1832	WF	H α	yes	14	320
163-026	PC	H α	no	7	150
165-254	PC	H α	yes	10	100
167-231	PC	H α	yes	13	140
172-028	PC	H α	no	6	130
182-332	STIS/CCD	[O III]	yes	6	70
183-405	PC	H α	yes	25	260
191-232	WF	H α	yes	5	110
203-506	WF	H α	yes	10	230
218-354	PC	H α	yes	50	520
218-529	WF	H α	yes	6	140
239-334	WF	H α	yes	6	140
294-606	WF	H α	no	6	270
072-135	WF	[O III]	no	5	230
109-247	WF	H α	yes	< 3	< 70
109-327	PC	[O III]	no	3	70
117-352	WF	[O III]	no	3	140
135-220	WF	[O III]	no	2	90
141-520	WF	H α	yes	6	140
143-522	WF	NII	no	2	90
147-323	WF	[O III]	no	2	90
154-240	PC	H α	yes	7	70
155-338	WF	[O III]	no	2	90
158-326	WF	[O III]	no	2	90
159-418	WF	[O III]	no	1	50
163-222	STIS/CCD	[O III]	yes	4	50
170-249	STIS/CCD	[O III]	yes	~11	~130
171-340	STIS/CCD	[O III]	yes	7	80
174-236	STIS/CCD	[O III]	yes	10	120
175-355	PC	H α	yes	4	40
176-543	WF	H α	yes	8	180
181-247	STIS/CCD	[O III]	yes	5	60
182-413	PC	H α	yes	14	150
183-419	PC	H α	yes	7	70
197-427	STIS/CCD	[O III]	yes	10	120
203-504	WF	H α	no	~2	~90
205-421	PC	[O III]	no	5	100
206-446	PC	[O III]	no	6	130
244-440	WF	H α	yes	15	300

The central star of the object 218-354 becomes excessively bright at near-infrared wavelengths and outshines the circumstellar disk. Accordingly, only one disk size could be measured at near-infrared wavelength.

For each of the 5 circumstellar disks that have been analysed using multi-wavelength data, the corresponding narrow-band filter images, as well as the intensity profiles along the disk's major axis are displayed below. The objects are shown in descending order, starting with the largest circumstellar disk known in the Orion Nebula (114-426), and ending at a size where precise measurements were still possible. Disk parameters like inclination, position angle, and size can be found in Tables 3.2, 3.3 and 3.4, respectively. With the exception of 114-426 where Pa α images were available, all other disks are shown in the three emission line filters [O II], [O III] and H α at 3727 Å, 5007 Å and 6563 Å, respectively.

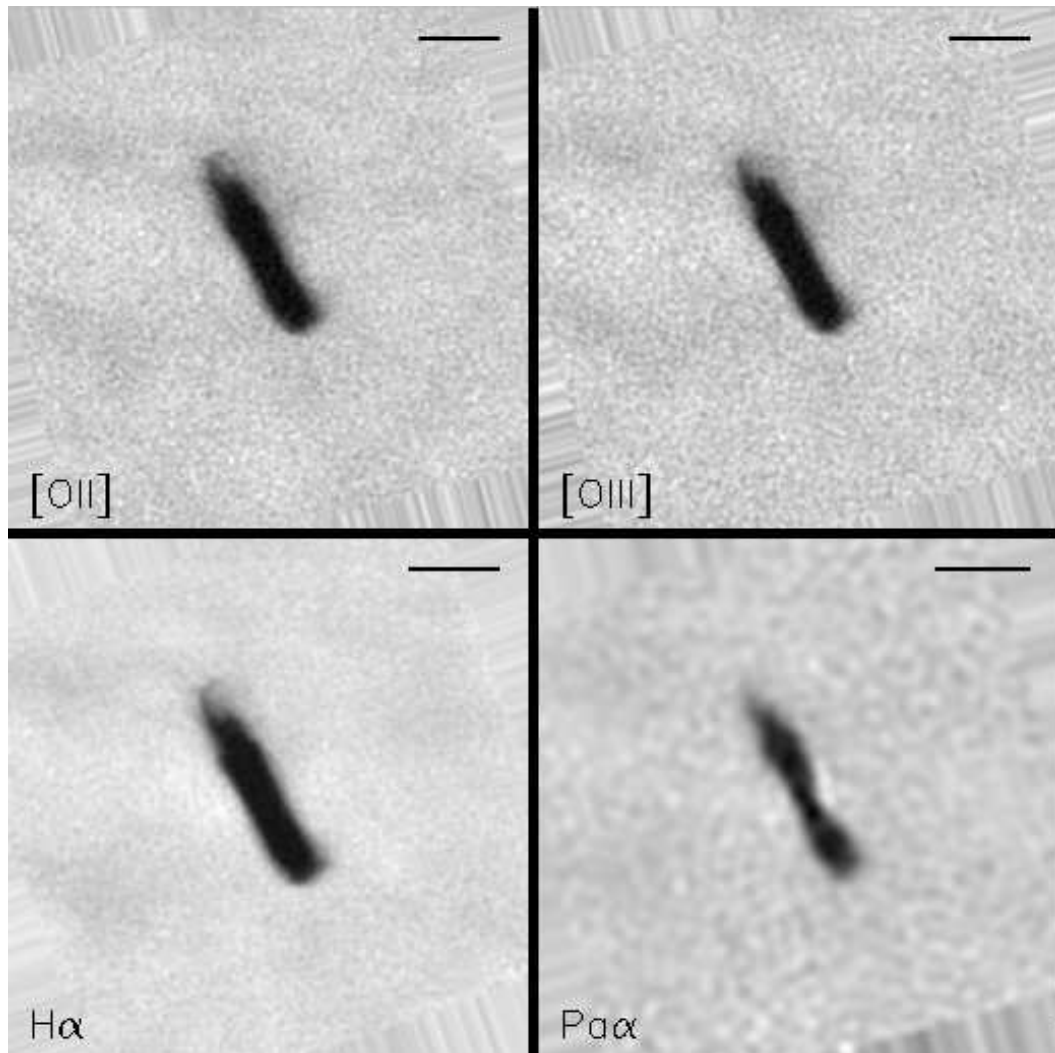


Figure 3.5. Circumstellar disk 114-426 as seen in different filters as given in the lower left corner of each panel. The bar drawn in the upper right corner corresponds to 1'', approximately 460 AU at the distance of the Orion Nebula. All images were aligned such that north is towards the top, and east towards the left. The streaky pattern of the image borders is a result of the rotation procedure.

The actual size measurement was done using the intensity profiles along the disks' major axis. Differing from 3.3.2, the half-light diameter is measured where the nebular intensity drops to one half of its original value measured from the non-zero disk minimum intensity. The flux detected from the central portions of the dark disk is typically 10–30% of the local background intensity.

Even small amount of dust grains, however, should render the disk completely opaque when illuminated from behind. There are several possible explanations to account for the apparent illumination of the disk. First, a fraction of the radiation coming from the central star will be scattered off the outer disk layers, thereby illuminating the disk (Whitney & Hartmann, 1992, 1993). Second, some flux might come from the H II region lying in front of the dark disk, i. e. from ionised material between the disk and the observer (Wen & O'Dell, 1995). Third, the telescope PSF which blends flux of the central star into the dark, surrounding disk. PSF deconvolution using the SOLA algorithm (cf. Section 3.2.3) was not entirely capable of suppressing the non-zero central flux; see the corresponding intensity profiles. Insufficient subtraction of the central star contribution led to uncertainties as to where to define the minimum intensities. These uncertainties, in turn, affected the size measurement for all object save 114-426. One possible solution to this problem is disk modelling, as described in Section 1.3.3. This task, however, is beyond the scope of this thesis.

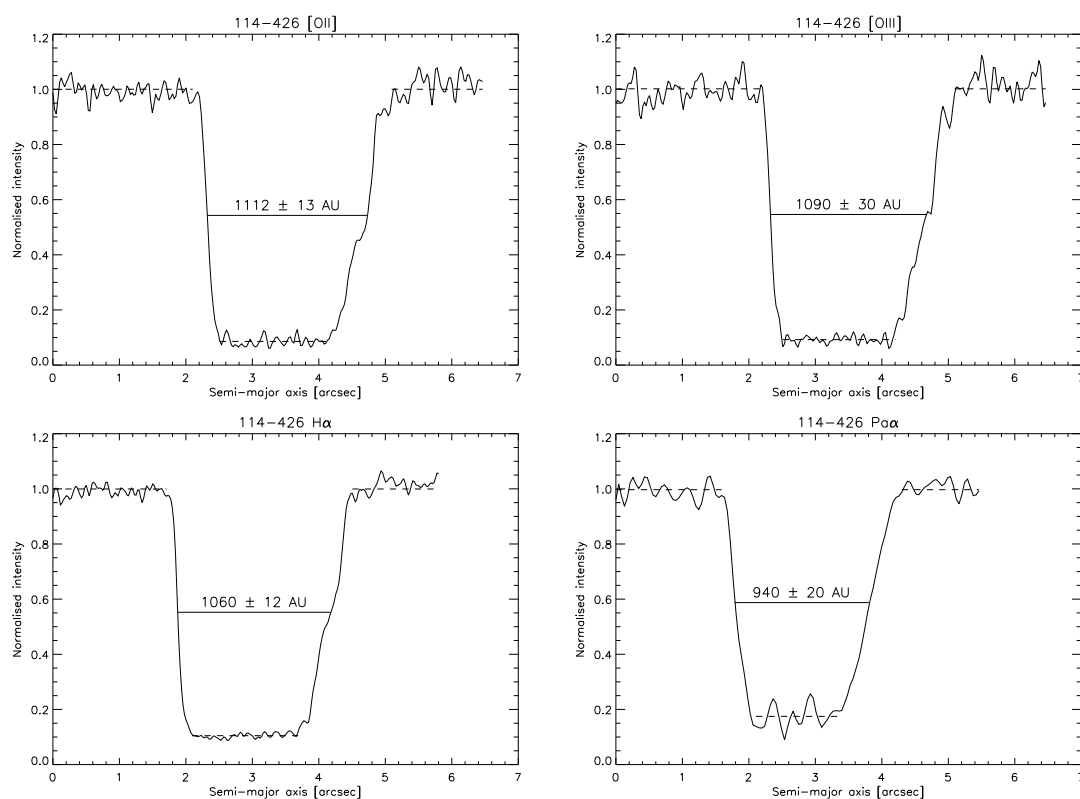


Figure 3.6. Intensity profiles along the major axis of 114-426. The arrangement is the same as in Figure 3.5, i. e. from upper left to lower right the profiles for [O II], [O III], H α and Pa α respectively; see also headline for each plot. The intensity of the background nebulosity has been normalised to one. The dashed line shows the fit to the local value. A constant, non-zero intensity has been fitted to the remaining flux in the disk region, drawn as a broken line. The size measured is given in the plot.

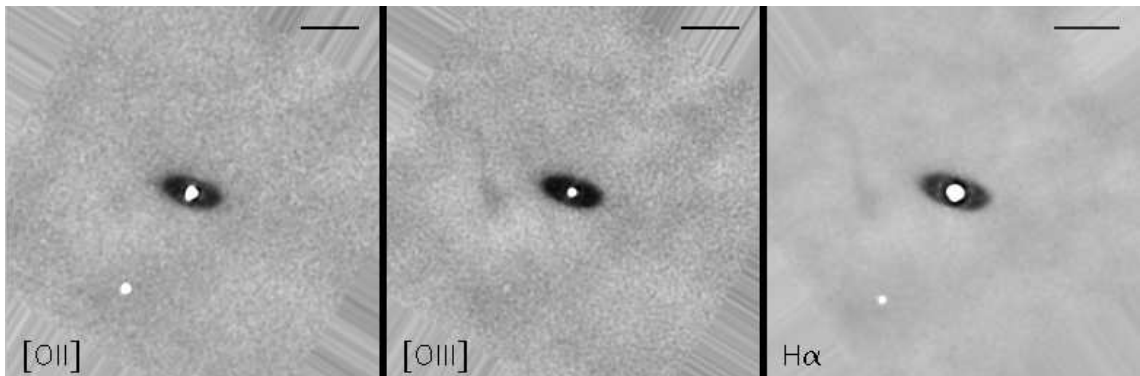


Figure 3.7. Circumstellar disk 218-354 seen in the light of the emission line filters [O II], [O III] and $H\alpha$, respectively. The existing $\text{Pa}\alpha$ $\lambda 1.876 \mu\text{m}$ images were not used because the central star is too bright at near-infrared wavelengths, and renders an accurate measurement impossible. The bar shows $1''$, corresponding to approximately 460 AU at the distance of the Orion Nebula. All images were aligned such that north is towards the top, and east towards the left.

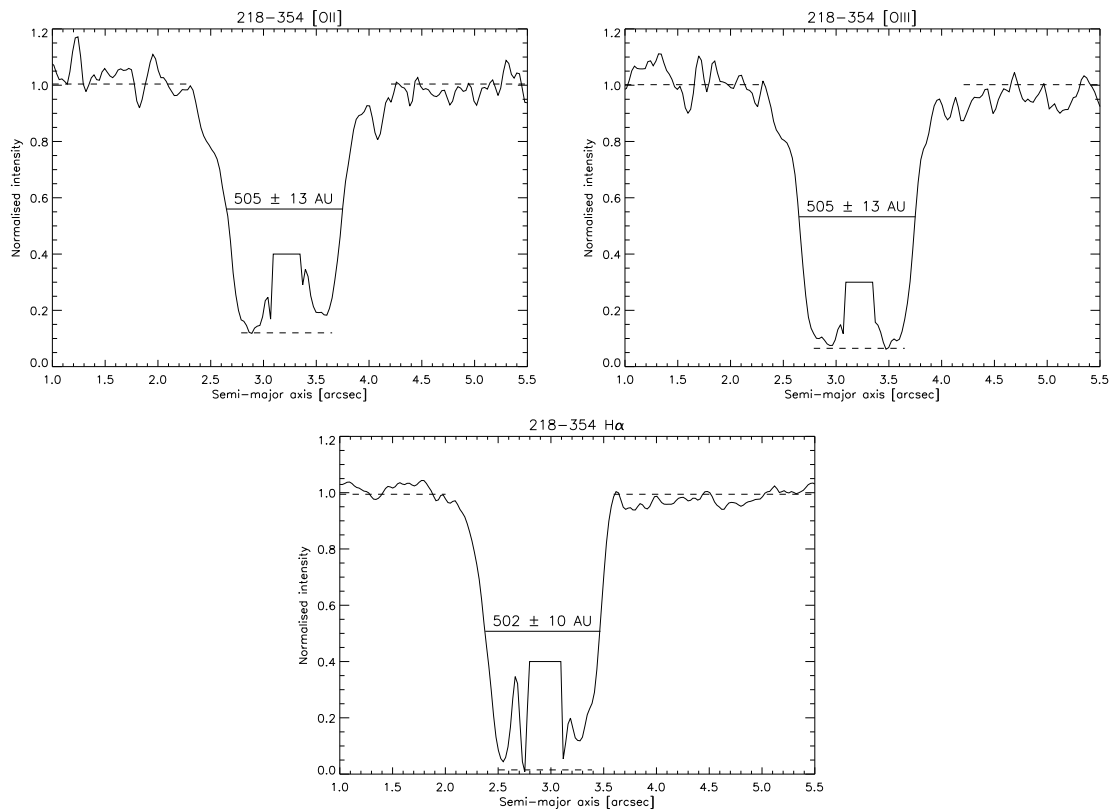


Figure 3.8. Intensity profiles along the major axis of 218-354. The top left diagram shows the [O II] profile, the top right plot the [O III] profile, while $H\alpha$ is shown in the bottom line. The central star has been masked. The flux contribution of the disk has been set to the minimal intensity.

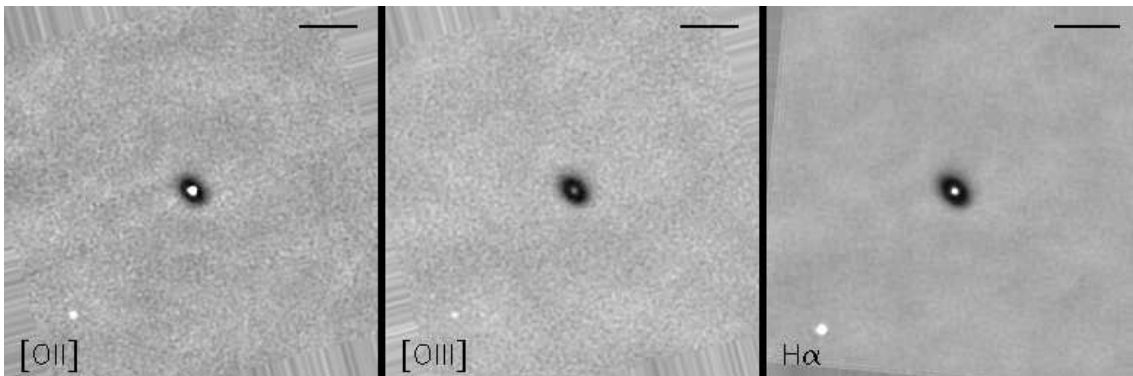


Figure 3.9. Circumstellar disk 183-405 seen in the filters [O II], [O III] and $H\alpha$, respectively. The bar shows $1''$, corresponding to approximately 460 AU at the distance of the Orion Nebula.

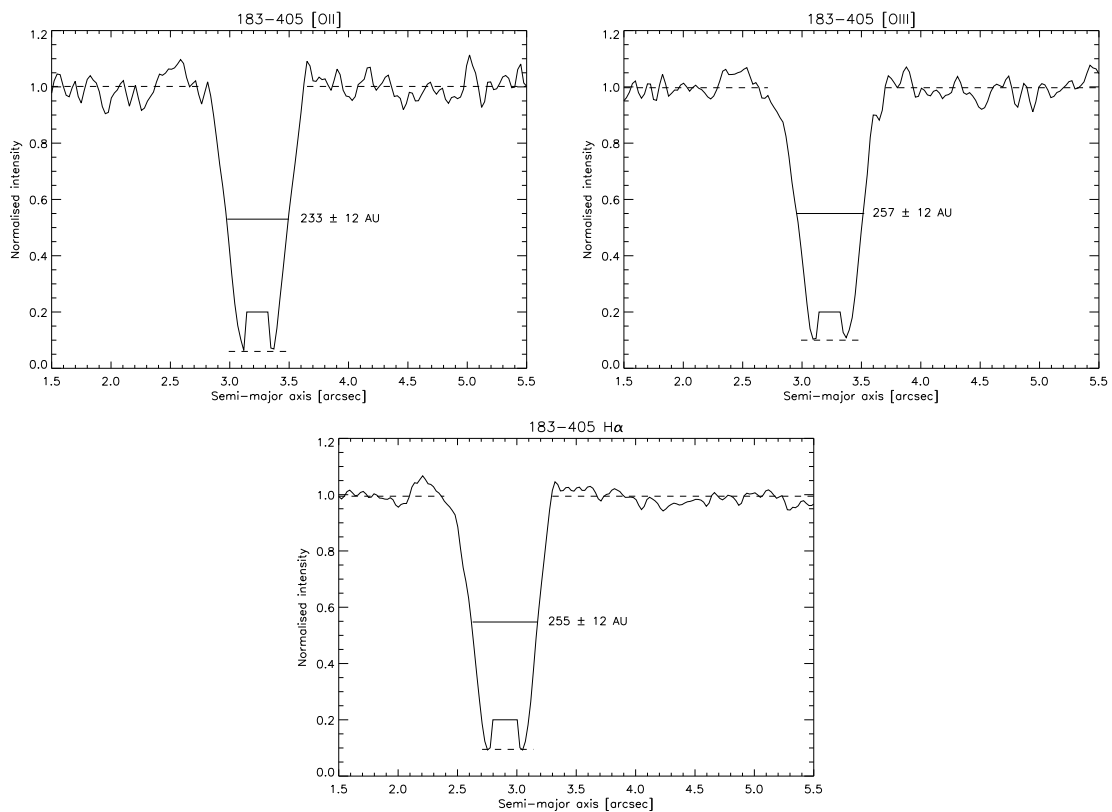


Figure 3.10. Intensity profiles along the major axis of 183-405. The arrangement of the plots is identical to Figure 3.8. The central star has been masked. The flux contribution of the disk has been set to the minimal intensity.

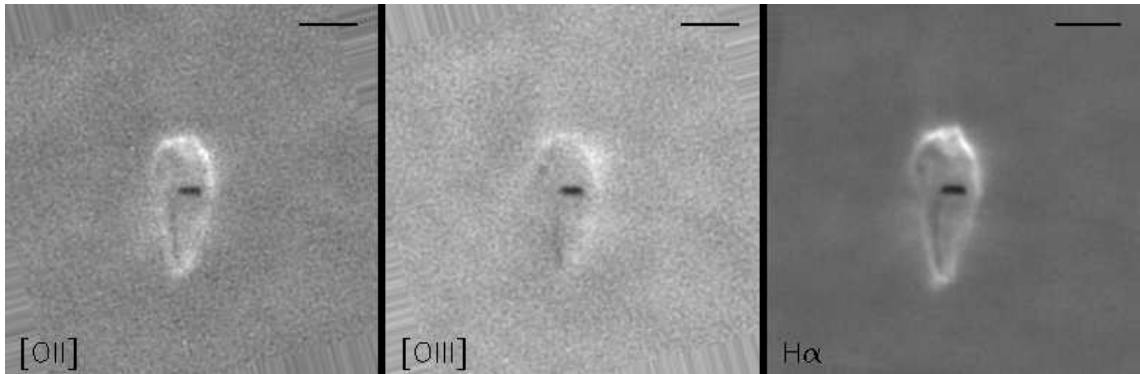


Figure 3.11. Multi-wavelength images of the ionised disk 182-413. From left to right: [O II], [O III] and $H\alpha$, respectively. The bar shows $1''$, corresponding to approximately 460 AU at the distance of the Orion Nebula.

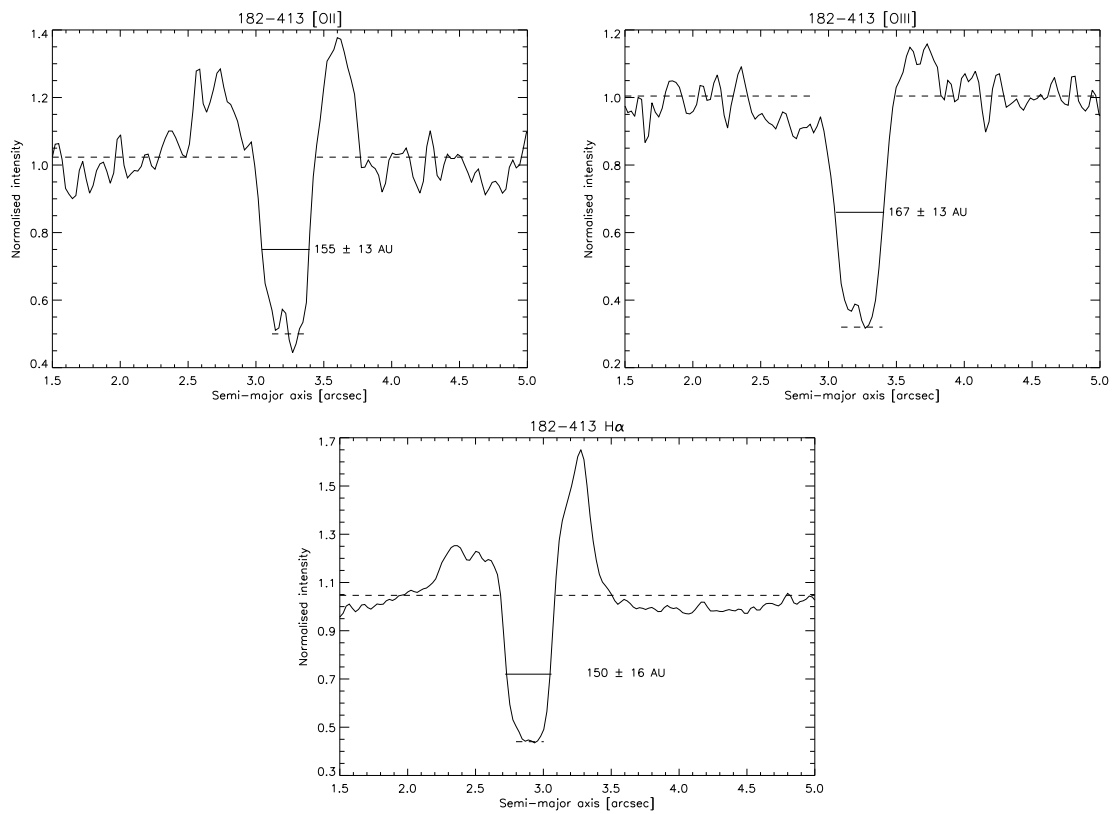


Figure 3.12. Intensity profiles along the major axis of the ionised disk 182-413. The flux contribution of the disk has been set to the minimal intensity.

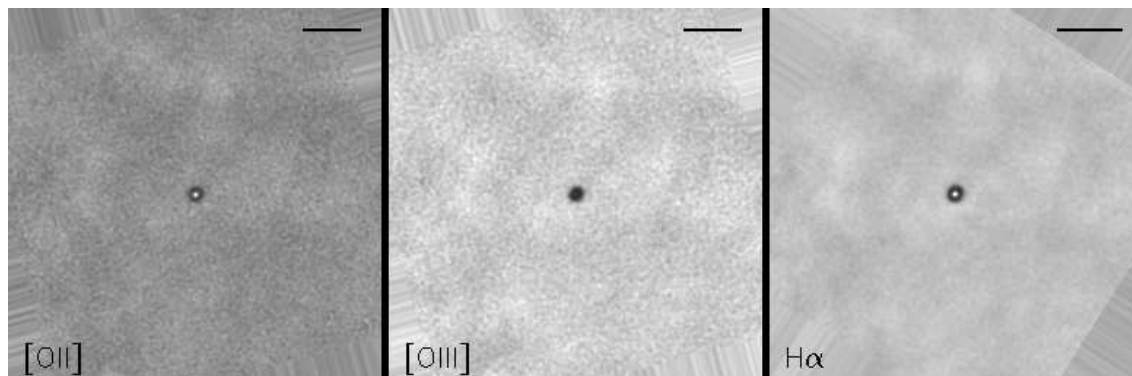


Figure 3.13. Circumstellar disk 167-231 seen in the light of the emission line filters [OII], [OIII] and $H\alpha$, respectively. The bar shows $1''$, corresponding to approximately 460 AU at the distance of the Orion Nebula.

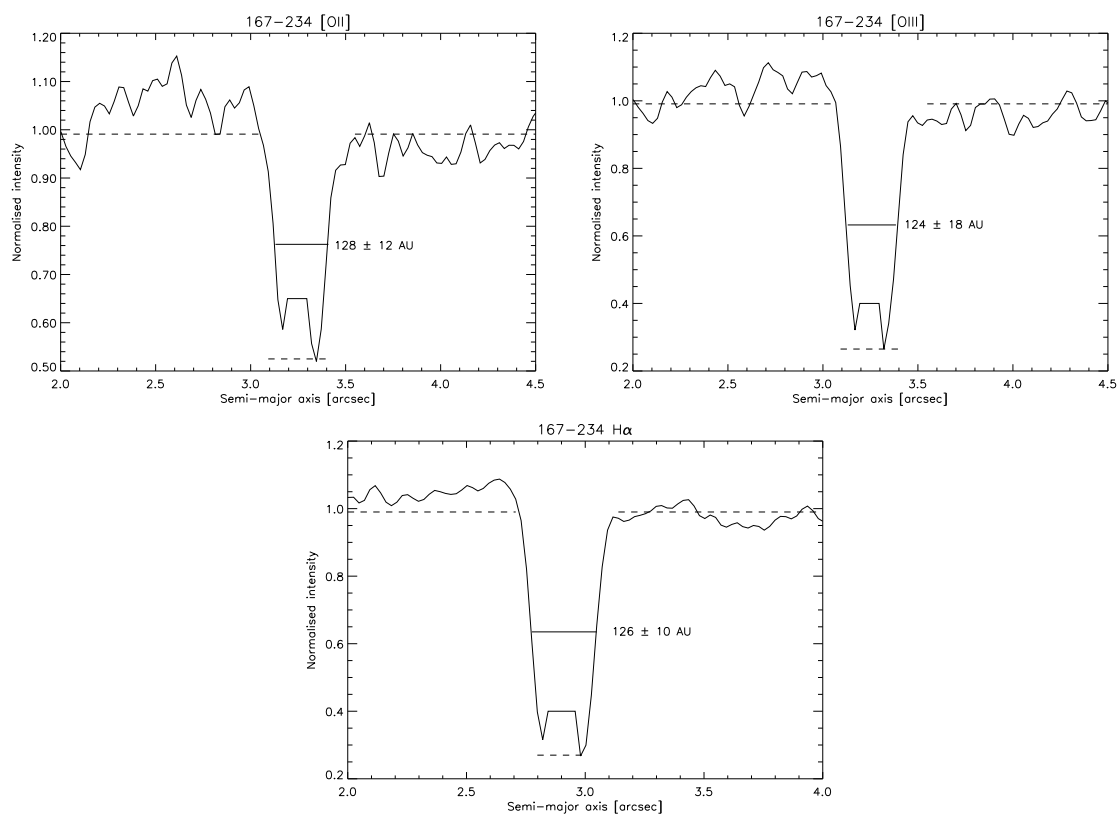


Figure 3.14. Intensity profiles along the major axis of 167-231. The central star has been masked. The flux contribution of the disk has been set to the minimal intensity.

3.3.4 *JHK* photometry

In addition to *Hubble Space Telescope* data, *JHK* photometric data from Meeus (2002) taken with the ISAAC instrument on the VLT was used to determine the masses of the central stars of the known circumstellar disks. The idea was to link the masses obtained to the properties of their corresponding circumstellar disk. An empiric relation between the mass of the central star and the disk size is still lacking.

Unfortunately, only for a minority of the objects listed in Table 3.4 *JHK* photometry was available. They were either outside of the region covered, or only insufficient photometric data was available. The linking of stellar masses and disk properties for the population of circumstellar disks in the Trapezium Cluster has to await the arrival of a sufficiently deep and wide near-infrared photometric database.

Chapter 4

Results

Доверяй, но проверяй.
(*Trust is good, control is better.*)

V. I. LENIN

4.1 Disk size distributions

We will now discuss the results of the size measurements of circumstellar disks as described in Section 3.3. For 41 of 48 known objects where a disk is visible, physical diameters were determined, cf. Table 3.4. Figure 4.1 shows the size distribution histograms for silhouette and ionised disks separately, as well as for the combined population.

The diameters of silhouette disks cover a range from <70 AU to ~ 1000 AU, cf. Figure 4.1 (top panel). The number of objects is increasing towards smaller sizes, the median disk diameter being 150 AU. The apparent lack of objects having sizes below ~ 100 AU is due to the angular resolution limit of the instruments used. At the distance of the Orion Nebula (~ 460 pc, Bally et al., 2000), a 100-AU disk extends over ~ 4 pixels when imaged with the Planetary Camera or the STIS/CCD. Using the Wide Field Cameras with a pixel scale of approximately 0.1 arcsec/pixel such a disk would extend over only ~ 2 pixels. Image dithering improves the situation somewhat, producing an increase in angular resolution of about 20%. The asymmetric shape of the distribution suggests a steady increase in the number of disks towards smaller sizes. The number of detected silhouette disks smaller than ~ 100 AU, therefore, is considerably underestimated.

Already a first inspection of the values listed in Table 3.4 reveals that ionised disks embedded within bright proplyds are generally smaller than silhouette disks. The median disk diameter is 90 AU for the ionised disks, cf. Figure 4.1 (middle panel). Although being more numerous than silhouette disks, the range of possible diameters of the ionised disks is confined to values <400 AU. More than 90% of the ionised disks (24 of 26) have sizes below 200 AU. In fact, almost 60% are smaller than 100 AU.¹ There is also an angular resolution limit for the detection of ionised disks; due to the given bin size of 100 AU, it is not immediately obvious. The angular resolution detection limit in the case of ionised disks is around 50 AU. It is about a factor of two smaller than for silhouette disks because they are surrounded by bright proplyds that indicate the existence of a circumstellar disk already (Henney & O'Dell, 1999).

¹To be compared with the size of the planetary region of the solar system. Including the Kuiper Belt that region extends to approximately 50 AU in radius, or 100 AU in diameter.

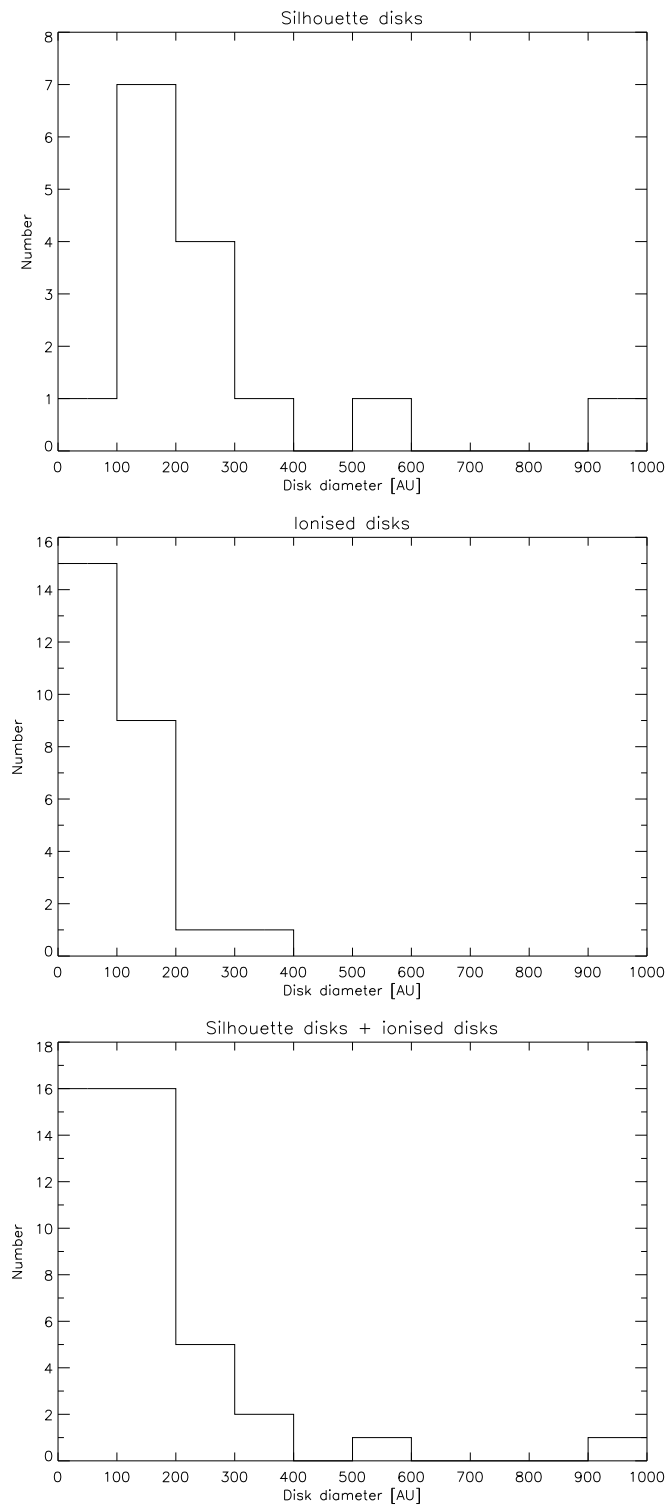


Figure 4.1. Disk size distribution for silhouette disks (top panel), ionised disks (middle panel), and combined population (bottom panel). In total 41 circumstellar disk were measured, thereof 15 disks purely seen as dark silhouettes against the bright background of the Orion Nebula H II region, and 26 disk ionised disks embedded within bright ionisation fronts. Note the scale change of the abscissae.

The bottom panel of Figure 4.1 displays the disk size distribution for the complete population of known circumstellar disks. Almost 80% of the circumstellar disks, being silhouette or ionised, are smaller than 200 AU. The median value for the disk diameter is 120 AU, i. e. slightly larger than the size of the solar system planetary region. The flat top of the histograms is a result of two combined angular resolution limits, with silhouette disks below ~ 100 AU, and ionised disks smaller than ~ 50 AU missing. We argue that the majority of (smaller) circumstellar disk remains undetected with the angular resolution achieved by current observational facilities.

Kolmogorov-Smirnov test The dissimilarity between the size distribution of silhouette disks on the one hand, and ionised disks on the other hand, can be quantified in terms of the so-called Kolmogorov-Smirnov test (Press et al., 1986).

The Kolmogorov-Smirnov test (or K–S test for short) provides a measure to determine whether two distributions differ significantly. These two distributions can be either measured and theoretical distributions, or two measured distributions of the same kind. Each data set is converted into a corresponding cumulative distribution. The K–S statistic d to measure the overall difference between two cumulative distribution functions is defined as the maximum value of the absolute difference between the two functions. The K–S statistic is then used to calculate the null hypothesis probability p , i. e. the likelihood that the two data sets have the same distribution.

The Kolmogorov-Smirnov test was applied to calculate the probability that the disk size distributions for silhouette and ionised disk, respectively, are the same. The results are shown in Figure 4.2. The K–S statistic was $d = 0.51$; the null hypothesis probability was calculated to be $p = 0.0085$. We state, therefore, within a statistical significance of approximately 2.6σ that the two data sets were not drawn from the same distribution. Less technically speaking, we can say that silhouette disk and ionised disks belong to two distinctly separated class of circumstellar objects.

Distance from θ^1 Ori C While silhouette disks show no or little ionisation, ionised disks appear to be strongly perturbed by the ambient radiation field. The main source of ionising ultraviolet photons (energies above 13.6 eV) is θ^1 Ori C, the brightest and hottest star in the Orion Nebula. θ^1 Ori C is a member of the central Trapezium group, and is located in the centre of the eponymous Trapezium Cluster. Circumstellar disks receiving sufficient flux of ionising radiation suffer photoevaporation-driven mass loss of the order of 10^{-6} – $10^{-7} M_{\odot} \text{ yr}^{-1}$ (Churchwell et al., 1987; Henney & O’Dell, 1999). It is arguable that the mass loss rate increases towards the θ^1 Ori C.

Using the values of Table 3.4, one can plot disk sizes as a function of the projected separation from θ^1 Ori C, see Figure 4.3. As a result of the two-dimensional projection, all distances are systematically underestimated. There is no clear segregation between silhouette and ionised disks in terms of projected separation from θ^1 Ori C. It is not immediately clear how to interpret this result. Naively one would expect to find the ionised disk closer to the source of ionising ultraviolet radiation. The circumstellar disks seen in silhouette, on the other hand, escape ionisation by being located far enough from the ionisation source. Unfortunately, the number of objects is too small to disentangle the actual distribution of circumstellar disk with distance from the cluster centre, and artificial distributions due to projection effects. There is an obvious “zone of avoidance” within 1’ projected distance to θ^1 Ori C. In this region no disk larger than ~ 150 AU is found. The number density of objects, otherwise increasing towards the centre, is also lower. The outer radius of this zone (~ 0.15 pc) corresponds to the cluster core radius of 0.05–0.2 pc (Hillenbrand & Hartmann, 1998).

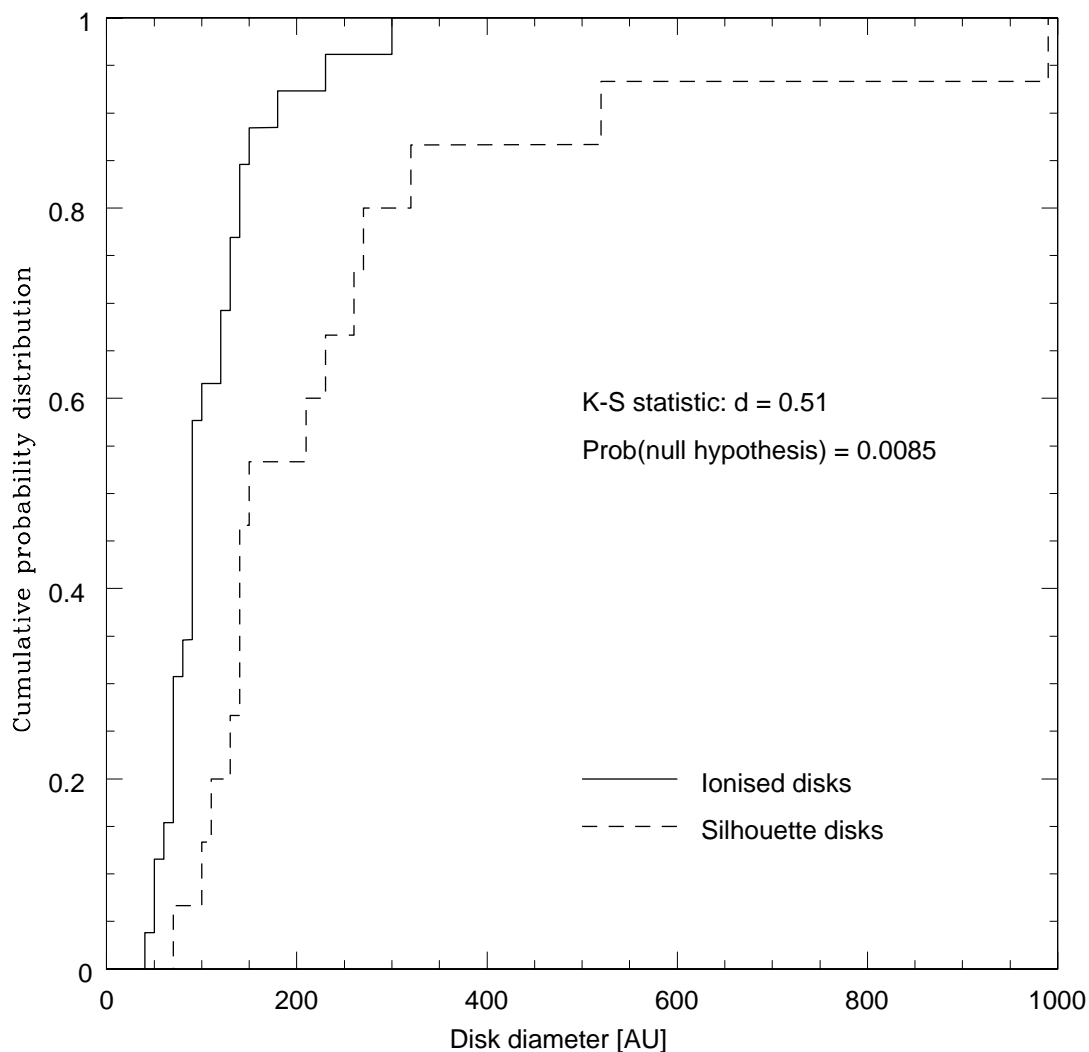


Figure 4.2. Kolmogorov-Smirnov test for disk size distributions of silhouette and ionised disk. The cumulative distribution functions of the ionised and silhouette disks are shown as solid and dashed line, respectively. The K–S statistic, simply the maximal vertical distance between the two functions, yields $d = 0.51$. Using that value the null hypothesis probability is calculated to be less than 1%.

Interestingly, there is a loose relation between disk diameter and projected distance from θ^1 Ori C outside this radius. The disk sizes appear to scale roughly with the square of the projected distance, cf. Figure 4.3. This relation remains unaffected by projection effects because the physical disk sizes are intrinsic properties not altered by projection onto the sky. This indicative result suggests that disks closer to θ^1 Ori C are generally smaller in size, probably due to increased photoevaporation-powered mass loss. This argument, however, is not stringent and needs a larger statistical base for further study. Figure 4.3

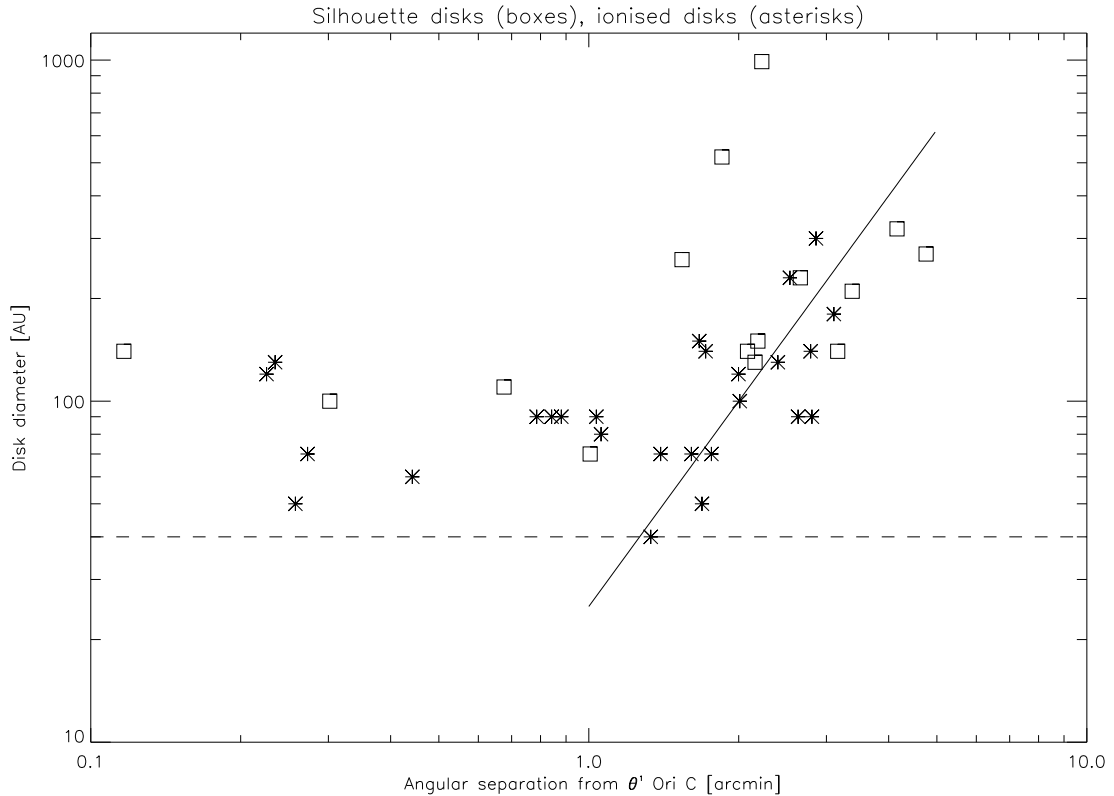


Figure 4.3. Disk diameter as a function of the projected angular separation from θ^1 Ori C. Boxes denote disks seen in silhouette, asterisks those that are embedded within ionisation features. The dashed line at 40 AU corresponds roughly to the resolution limit of the Planetary Camera or the STIS/CCD. The solid line with slope 2 indicates an apparent increase in the average disk size outside of $1'$ to θ^1 Ori C. As a result of the two-dimensional projection, the actual distances may be highly underestimated.

4.2 Wavelength-dependence of disk size

Multi-wavelength images of circumstellar disks can, in principle, be used to assess the properties of dust grain particles. Given submicrometre-sized, ISM dust particles, the extinction of dust is inversely proportional to the wavelength used (Mathis, 1990). That means that the transmission of light with near-infrared wavelengths is higher than at shorter wavelengths. A circumstellar disk with translucent outer edges will, therefore, appear smaller at longer wavelengths when illuminated from behind. If, on the other hand, dust particles have grown to sizes significantly larger than the wavelength used, the extinction curve becomes achromatic, i. e. independent of wavelength (Evans, 1994).

114-426 Figure 4.4 shows the results of the measurements as described in Section 3.3.3. In the case of 114-426 (top panel), the largest circumstellar disk in the Orion Nebula, the apparent disk diameter decreases from ~ 1100 AU when seen in the $[\text{O II}] \lambda 3727 \text{ \AA}$ emission line, to ~ 950 AU in the $\text{Pa}\alpha \lambda 1.876 \mu\text{m}$ narrow-band filter. Comparing $\text{H}\alpha$ and $\text{Pa}\alpha$ images of 114-426 at $0.6 \mu\text{m}$ and $1.87 \mu\text{m}$, respectively, McCaughrean et al. (1998) reported a $\sim 20\%$ smaller major axis in the latter filter. We find $\sim 11\%$, a factor of two smaller.

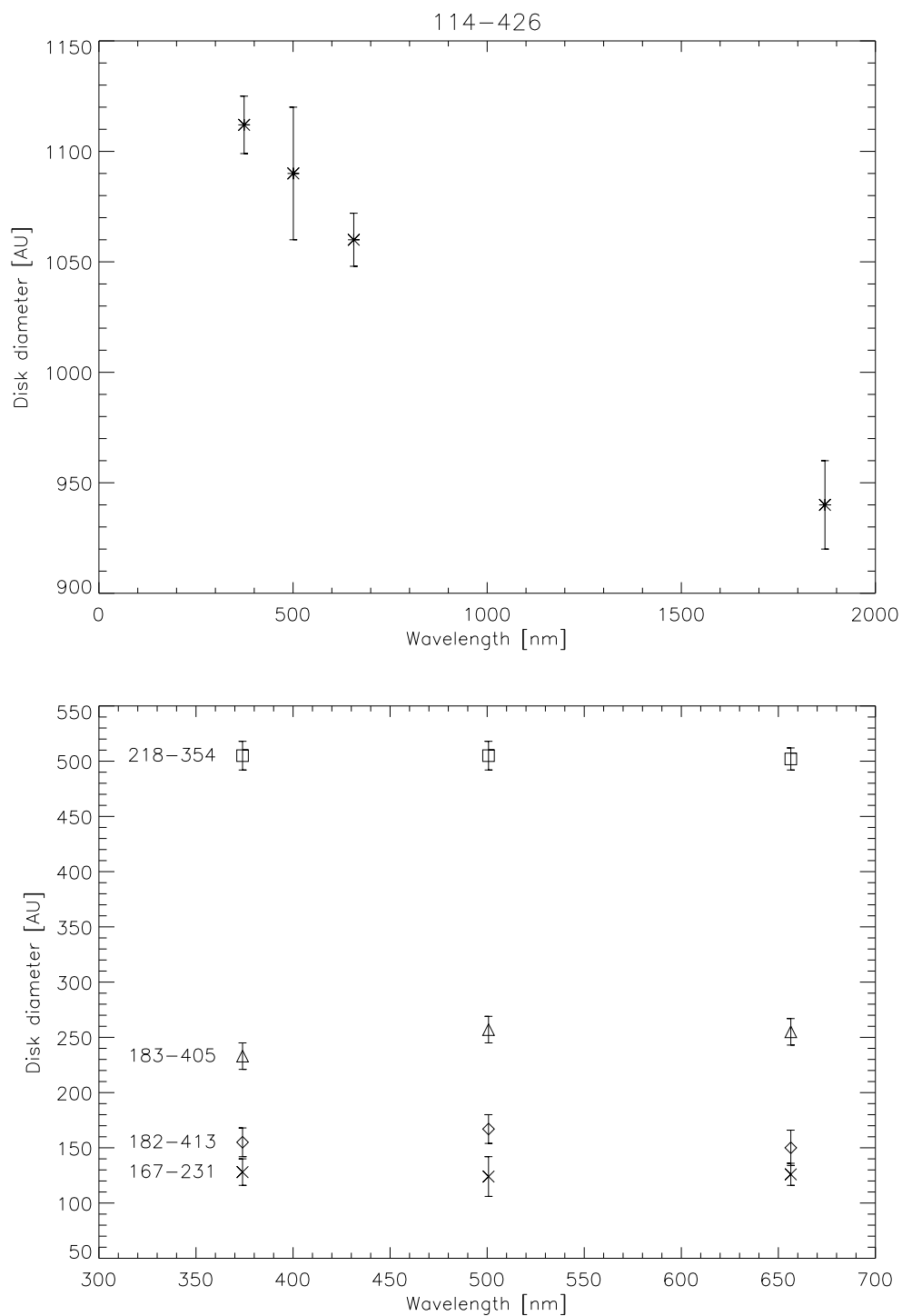


Figure 4.4. Apparent diameter of selected circumstellar disks as a function of wavelength. *Top panel:* Disk size measurements for the edge-on disk 114-426 as a function of wavelength. The used emission line filter are (with increasing wavelength): [O II], [O III], H α and Pa α . *Bottom panel:* Disk size measurements for four other disks. The wavelength baseline is much smaller because no Pa α images were available.

Throop et al. (2001) claimed indistinguishable $H\alpha$ and $Pa\alpha$ intensity profiles for 114-426, i.e. an achromatic extinction curve. They argued that this result points to the existence of circumstellar dust grains larger than $10 \mu\text{m}$ in size, 25–50 times larger than normal interstellar dust grains with sizes of about $\sim 0.3 \mu\text{m}$. The lack of millimetre continuum emission at $\lambda = 1.3 \text{ mm}$ and $\lambda = 3.5 \text{ mm}$ (Mundy et al., 1995; Bally et al., 1998b) was interpreted as a possible evidence for dust grain agglomeration to even millimetre-sized aggregates. Our results clearly demonstrate that the extinction is smaller at near-infrared wavelengths. Since the corresponding extinction curve is chromatic, one cannot assume an appreciable amount of micrometre-sized dust grains.

218-354, 183-405, 182-413, 167-231 The bottom panel of Figure 4.4 displays the results of the multi-wavelength images analysis for the circumstellar disks 218-354, 183-405, 182-413 and 167-231. With the exception of 182-413, all disks are seen only in silhouette. Intensity profiles along the disk major axis have been taken using the following emission line filters: [O II] $\lambda 3727 \text{ \AA}$, [O III] $\lambda 5007 \text{ \AA}$, and $H\alpha \lambda 6563 \text{ \AA}$.

All measured disk diameters are independent of the wavelength. There are two possible explanations to account for this achromatic extinction. First, agglomeration of dust grains to aggregates several micrometre in size would produce wavelength-independent extinction features. As the near-ultraviolet and visual observation wavelengths would be now much smaller than the dust aggregates, light is blocked and attenuated by geometric screening. The optical depth would be then a function of particle density alone. However, the measurements are insufficient, and do not endorse this conclusion. Since only a relatively narrow wavelength range of $\sim 150 \text{ nm}$, ten times smaller than for the measurement of 114-426, was covered, the measurements are insufficient, and do not endorse this conclusion. Furthermore, the analysis of non-edge-on system is negatively affected by the presence of the bright central star. Its flux spreads into the neighbouring disk, filling in the dark region, thereby deteriorating the star/disk contrast. The PSF deconvolution performed is not completely able to remove the light contribution of the central star.

A second possible explanation for wavelength-independence disk size measurements is edge truncation caused by tidal interaction between the disk and an interloper star, and/or by radiation-powered ablation of circumstellar material combined with strong stellar winds from the central OB stars; see McCaughrean et al. (2000) for further mechanisms. Across the edge of a silhouette disk, the optical depth changes from $\tau = 0$ outside, to $\tau \gg 1$ within the disk. The sharpness of the edge defines the spatial extent of the translucent region, where $0 < \tau < 1$. The method described to probe the dust grain properties only works within that finite region. Edge truncation processes may reduce the size of the translucent outer region below resolution values.

Bibliography

- Adams, F. C., Lada, C. J., & Shu, F. H. 1987, *ApJ*, 312, 788
- Allègre, C. J., Manhès, G., & Göpel, C. 1995, *Geochim. Cosmochim. Acta*, 59, 1445
- André, P., Ward-Thompson, D., & Barsony, M. 1993, *ApJ*, 406, 122
- André, P., Ward-Thompson, D., & Barsony, M. 2000, in *Protostars and Planets IV*, ed. V. Mannings, A. P. Boss, & S. S. Russell (Tucson: The University of Arizona Press), pp. 59–96
- Appenzeller, I., Oestreicher, R., & Jankovics, I. 1984, *A&A*, 141, 108
- Bachiller, R. & Tafalla, M. 1999, in *The Origin of Stars and Planetary Systems*, ed. C. J. Lada & N. D. Kylafis (Dordrecht: Kluwer Academic Publishers), 287
- Balbus, S. A. & Hawley, J. F. 1991, *ApJ*, 376, 214
- Bally, J., O’Dell, C. R., & McCaughrean, M. J. 2000, *AJ*, 119, 2919
- Bally, J., Sutherland, R. S., Devine, D., & Johnstone, D. 1998a, *AJ*, 116, 293
- Bally, J., Testi, L., Sargent, A., & Carlstrom, J. 1998b, *AJ*, 116, 854
- Beckwith, S. V. W., Henning, T., & Nakagawa, Y. 2000, in *Protostars and Planets IV*, ed. V. Mannings, A. P. Boss, & S. S. Russell (Tucson: The University of Arizona Press), pp. 533–558
- Biretta, J. A. & al. 2000, *WFPC2 Instrument Handbook*, Version 5.0 (Baltimore: STScI)
- Blitz, L. 1993, in *Protostars and Planets III*, ed. E. H. Levy & J. I. Lunine (Tucson: The University of Arizona Press), pp. 125–161
- Bodenheimer, P. 1965, *ApJ*, 142, 451
- . 1995, *ARA&A*, 33, 199
- Bodenheimer, P., Burkert, A., Klein, R. I., & Boss, A. P. 2000, in *Protostars and Planets IV*, ed. V. Mannings, A. P. Boss, & S. S. Russell (Tucson: The University of Arizona Press), pp. 675–701
- Boss, A. P. 1997, *Science*, 276, 1836

- Bowers, C., Hartig, G., Kaiser, M., Kraemer, S., Gull, T., Kimble, R., Woodgate, B., Bohlin, R., Plait, P., Lindler, D., Ebbets, D., Sullivan, J., Hill, R. S., Kinney, E., Sahu, K., Crenshaw, M., Collins, N., Danks, A., Robinson, R., Cornett, R., & Gruzysak, A. 1997, *American Astronomical Society Meeting*, 29, 836
- Burrows, C. J., Stapelfeldt, K. R., Watson, A. M., Krist, J. E., Ballester, G. E., Clarke, J. T., Crisp, D., Gallagher, J. S., Griffiths, R. E., Hester, J. J., Hoessel, J. G., Holtzman, J. A., Mould, J. R., Scowen, P. A., Trauger, J. T., & Westphal, J. A. 1996, *ApJ*, 473, 437
- Cernicharo, J. 1991, in *The Physics of Star Formation and Early Stellar Evolution*, ed. C. J. Lada & N. D. Kylafis (Dordrecht: Kluwer Academic Publishers), 287
- Charbonneau, D., Brown, T. M., Latham, D. W., & Mayor, M. 2000, *ApJL*, 529, L45
- Chiang, E. I., Joungh, M. K., Creech-Eakman, M. J., Qi, C., Kessler, J. E., Blake, G. A., & van Dishoeck, E. F. 2001, *ApJ*, 547, 1077
- Churchwell, E., Wood, D. O. S., Felli, M., & Massi, M. 1987, *ApJ*, 321, 516
- Conti, P. S. & Alschuler, W. R. 1971, *ApJ*, 170, 325
- Cox, A. N., ed. 2000, *Allen's Astrophysical Quantities* (New York: Springer-Verlag New York, Inc.)
- Crutcher, R. M. 1999, *ApJ*, 520, 706
- Dziembowski, W. A., Fiorentini, G., Ricci, B., & Sienkiewicz, R. 1999, *A&A*, 343, 990
- Elsässer, H. & Staude, H. J. 1978, *A&A*, 70, L3
- Encrenaz, T., Bibring, J.-P., & Blanc, M. 1995, *The Solar System* (Berlin: Springer-Verlag)
- Evans, A. 1994, *The Dusty Universe* (Chichester: Praxis Publishing Ltd)
- Frank, J., King, A., & Raine, D. 1992, *Accretion Power in Astrophysics* (Cambridge: Cambridge University Press)
- Fruchter, A. S. & Hook, R. N. 1997, in *Proc. SPIE: Applications of Digital Image Processing XX*, ed. A. G. Tescher, Vol. 3164, 120–125
- Fruchter, A. S. & Hook, R. N. 2002, *PASP*, 114, 144
- Goswami, J. N. & Vanhala, H. A. T. 2000, in *Protostars and Planets IV*, ed. V. Mannings, A. P. Boss, & S. S. Russell (Tucson: The University of Arizona Press), pp. 963–994
- Grady, C. A., Sitko, M. L., Russell, R. W., Lynch, D. K., Hanner, M. S., Perez, M. R., Bjorkman, K. S., & de Winter, D. 2000, *Protostars and Planets IV*, pp. 613
- Graner, F. & Dubrulle, B. 1994a, *A&A*, 282, 262
- . 1994b, *A&A*, 282, 269

- Hartmann, L. 1998, *Accretion Processes in Star Formation* (Cambridge: Cambridge University Press)
- Hartmann, L. & Calvet, N. 1995, *AJ*, 109, 1846
- Harwit, M. 1998, *Astrophysical Concepts* (New York: Springer-Verlag New York, Inc.)
- Henney, W. J. & O'Dell, C. R. 1999, *AJ*, 118, 2350
- Hénon, M. 1969, *Icarus*, 11, 93
- Herbig, G. H. 1977, *ApJ*, 217, 693
- Hillenbrand, L. A. & Hartmann, L. W. 1998, *ApJ*, 492, 540+
- Holtzman, J. A., Burrows, C. J., Casertano, S., Hester, J. J., Trauger, J. T., Watson, A. M., & Worthey, G. 1995, *PASP*, 107, 1065
- Jeans, J. H. 1928, *Astronomy and Cosmogony* (Cambridge: The University Press)
- Jewitt, D. C. & Luu, J. X. 2000, in *Protostars and Planets IV*, ed. V. Mannings, A. P. Boss, & S. S. Russell (Tucson: The University of Arizona Press), pp. 1201–1229
- Jones, A. P. 1997, in *From Stardust to Planetesimals*, ed. Y. J. Pendleton & A. G. G. M. Tielens (San Francisco: Astronomical Society of the Pacific), pp. 97–106
- Kalas, P. G. 1996, PhD thesis, University of Hawaii
- Keller, C. U., Deubner, F.-L., Egger, U., Fleck, B., & Povel, H. P. 1994, *A&A*, 286, 626
- Kenyon, S. J. & Hartmann, L. 1987, *ApJ*, 323, 714
- Kimble, R., Argabright, V., van Houten, C., Dorn, D., Blouke, M., Kraemer, S., Danks, A., Goudfrooij, P., Clampin, M., Beck, T., Malumuth, E., Landsman, W., Hill, R. J., Kaiser, M., Bowers, C., Hartig, G., Hayes, J., Baum, S., Bohlin, R., Ferguson, H., Leitherer, C., Feggans, J., & Sandoval, J. 1997, *American Astronomical Society Meeting*, 29, 836
- Kokubo, E. & Ida, S. 1996, *Icarus*, 123, 180
- Königl, A. & Pudritz, R. E. 2000, in *Protostars and Planets IV*, ed. V. Mannings, A. P. Boss, & S. S. Russell (Tucson: The University of Arizona Press), pp. 759–787
- Krist, J. 1993, in *ASP Conf. Ser. 52: Astronomical Data Analysis Software and Systems II*, Vol. 2, 536
- Krist, J. 1995, in *ASP Conf. Ser. 77: Astronomical Data Analysis Software and Systems IV*, Vol. 4, 349
- Lada, C. J. & Kylafis, N. D., eds. 1999, *The Origin of Stars and Planetary Systems* (Dordrecht: Kluwer Academic Publishers)
- Lada, C. J. & Wilking, B. A. 1984, *ApJ*, 287, 610

- Larson, R. B. 1984, MNRAS, 206, 197
- Laskar, J. 1996, in *Dynamics, Ephemerides and Astrometry of the Solar System*, IAU Symp. 172, ed. S. Ferraz-Mello, B. Morando, & J.-E. Arlot (Dordrecht: Kluwer Academic Publishers), pp. 75–88
- Lecar, M. 1973, Nature, 242, 318
- Léger, A., Gauthier, S., Défourneau, D., & Rouan, D. 1983, A&A, 117, 164
- Leitherer, C. & al. 2000, *STIS Instrument Handbook*, Version 4.1 (Baltimore: STScI)
- Lin, D. N. C. & Papaloizou, J. 1980, MNRAS, 191, 37
- Lin, D. N. C. & Papaloizou, J. 1985, in *Protostars and Planets II*, ed. D. C. Black & M. C. Matthews (Tucson: The University of Arizona Press), pp. 981–1072
- Lissauer, G. G. & Stewart, G. R. 1993, in *Protostars and Planets III*, ed. E. H. Levy & J. I. Lunine (Tucson: The University of Arizona Press), pp. 1061–1088
- Lucy, L. B. 1974, AJ, 79, 745
- Lynden-Bell, D. & Pringle, J. E. 1974, MNRAS, 168, 603
- Marcy, G. W. & Butler, R. P. 1998, ARA&A, 36, 57
- Mathis, J. S. 1990, ARA&A, 28, 37
- Mayor, M. & Queloz, D. 1995, Nature, 378, 355
- McCaughrean, M. J., Chen, H., Bally, J., Erickson, E., Thompson, R., Rieke, M., Schneider, G., Stolovy, S., & Young, E. 1998, ApJL, 492, L157
- McCaughrean, M. J. & O’Dell, C. R. 1996, AJ, 111, 1977
- McCaughrean, M. J., Stapelfeldt, K. R., & Close, L. M. 2000, in *Protostars and Planets IV*, ed. V. Mannings, A. P. Boss, & S. S. Russell (Tucson: The University of Arizona Press), pp. 485–507
- McCullough, P. R., Fugate, R. Q., Christou, J. C., Ellerbroek, B. L., Higgins, C. H., Spinhirne, J. M., Cleis, R. A., & Moroney, J. F. 1995, ApJ, 438, 394
- Meeus, G. 2002, *in preparation*
- Montmerle, T., Grosso, N., Tsuboi, Y., & Koyama, K. 2000, ApJ, 532, 1097
- Mundt, R. 1985, in *Protostars and Planets II*, ed. D. C. Black & M. C. Matthews (Tucson: The University of Arizona Press), pp. 414–433
- Mundy, L. G., Looney, L. W., & Lada, E. A. 1995, ApJ, 452, L137
- Narayan, R. & Nityananda, R. 1986, ARA&A, 24, 127

- Natta, A., Grinin, V. P., & Mannings, V. 2000, in *Protostars and Planets IV*, ed. V. Mannings, A. P. Boss, & S. S. Russell (Tucson: The University of Arizona Press), pp. 559–587
- O’Dell, C. R. 2001, *AJ*, 122, 2662
- O’Dell, C. R. & Wen, Z. 1994, *ApJ*, 436, 194
- O’Dell, C. R., Wen, Z., & Hu, X. 1993, *ApJ*, 410, 696
- O’Dell, C. R. & Wong, S. K. 1996, *AJ*, 111, 846
- Ossenkopf, V. 1991, *A&A*, 251, 210
- . 1993, *A&A*, 280, 617
- Padgett, D. L., Brandner, W., Stapelfeldt, K. R., Strom, S. E., Terebey, S., & Koerner, D. 1999, *AJ*, 117, 1490
- Padgett, D. L. & Stapelfeldt, K. R. 1999, in *Science with the Atacama Large Millimeter Array (ALMA)*, 47
- Palla, F. & Stahler, S. W. 1999, *ApJ*, 525, 772
- Pijpers, F. P. 1998, *MNRAS*, 297, L76
- . 1999, *MNRAS*, 307, 659
- Pijpers, F. P. & Thompson, M. J. 1992, *A&A*, 262, L33
- . 1994, *A&A*, 281, 231
- Press, W. H., Flannery, B. P., Teukolsky, S. A., & Vetterling, W. T. 1986, *Numerical Recipes: The Art of Scientific Computing* (Cambridge: University Press, 1986)
- Pringle, J. E. 1981, *ARA&A*, 19, 137
- Richardson, W. H. 1972, *J. Opt. Soc. Am.*, 62, 55
- Richer, J. S., Shepherd, D. S., Cabrit, S., Bachiller, R., & Churchwell, E. 2000, in *Protostars and Planets IV*, ed. V. Mannings, A. P. Boss, & S. S. Russell (Tucson: The University of Arizona Press), pp. 867–894
- Roberge, W. G., Hanany, S., & Messinger, D. W. 1995, *ApJ*, 453, 238
- Safronov, V. S. 1969, *Evolution of the Protoplanetary Cloud* (in Russian) (Moscow: Nauka)
- Sahu, K. C., Casertano, S., Livio, M., Gilliland, R. L., Panagia, N., Albrow, M. D., & Potter, M. 2001, *Nature*, 411, 1022
- Schultz, A. & al. 2001, *NICMOS Instrument Handbook*, Version 4.1 (Baltimore: STScI)
- Shakura, N. I. & Sunyaev, R. A. 1973, *A&A*, 24, 337

- Shu, F. H., Najita, J. R., Shang, H., & Li, Z. 2000, in *Protostars and Planets IV*, ed. V. Mannings, A. P. Boss, & S. S. Russell (Tucson: The University of Arizona Press), pp. 789–813
- Smith, B. A. & Terrile, R. J. 1984, *Science*, 226, 1421
- Stahler, S. W., Palla, F., & Ho, P. T. P. 2000, in *Protostars and Planets IV*, ed. V. Mannings, A. P. Boss, & S. S. Russell (Tucson: The University of Arizona Press), pp. 327–351
- Stognienko, R., Henning, T., & Ossenkopf, V. 1995, *A&A*, 296, 797
- Stone, J. M., Gammie, C. F., Balbus, S. A., & Hawley, J. F. 2000, in *Protostars and Planets IV*, ed. V. Mannings, A. P. Boss, & S. S. Russell (Tucson: The University of Arizona Press), pp. 589–611
- Tholen, D. J. & Buie, M. W. 1997, *Icarus*, 125, 245
- Throop, H. B., Bally, J., Esposito, L. W., & McCaughrean, M. J. 2001, *Science*, 292, 1686
- Trauger, J. T., Ballester, G. E., Burrows, C. J., Casertano, S., Clarke, J. T., Crisp, D., Evans, R. W., Gallagher, J. S., Griffiths, R. E., Hester, J. J., Hoessel, J. G., Holtzman, J. A., Krist, J. E., Mould, J. R., Scowen, P. A., Stapelfeldt, K. R., Watson, A. M., & Westphal, J. A. 1994, *ApJL*, 435, L3
- Trilling, D. E., Brown, R. H., & Rivkin, A. S. 2000, *ApJ*, 529, 499
- Vishniac, E. T. & Diamond, P. 1989, *ApJ*, 347, 435
- Walter, F. M. 1986, *ApJ*, 306, 573
- Wambsganß, J. 1997, *MNRAS*, 284, 172
- Ward, W. R. & Hahn, J. M. 1995, *ApJL*, 440, L25
- Weidenschilling, S. J. & Cuzzi, J. N. 1993, in *Protostars and Planets III*, ed. E. H. Levy & J. I. Lunine (Tucson: The University of Arizona Press), pp. 1031–1060
- Wen, Z. & O’Dell, C. R. 1995, *ApJ*, 438, 784
- Wetherill, G. W. & Stewart, G. R. 1989, *Icarus*, 77, 330
- Whitney, B. A. & Hartmann, L. 1992, *ApJ*, 395, 529
- . 1993, *ApJ*, 402, 605
- Whittet, D. C. B. 1992, *Dust in the Galactic Environment* (Bristol: Institute of Physics Publishing)
- Wilner, D. J. & Lay, O. P. 2000, in *Protostars and Planets IV*, ed. V. Mannings, A. P. Boss, & S. S. Russell (Tucson: The University of Arizona Press), pp. 509–532
- Wuchterl, G., Guillot, T., & Lissauer, J. J. 2000, in *Protostars and Planets IV*, ed. V. Mannings, A. P. Boss, & S. S. Russell (Tucson: The University of Arizona Press), pp. 1081–1109
- Wurm, G. 2001, *private communication*
- Zinnecker, H., McCaughrean, M. J., & Rayner, J. T. 1998, *Nature*, 394, 862
- Zinnecker, H., McCaughrean, M. J., & Wilking, B. A. 1993, in *Protostars and Planets III*, ed. E. H. Levy & J. I. Lunine (Tucson: The University of Arizona Press), pp. 429–495

List of Figures

1.1	Spacing of the planets and Titius-Bode law	5
1.2	Illustration of the Kant-Laplace nebular hypothesis	7
1.3	Carbonaceous chondrite sample	9
1.4	Correlation of solar and meteoritic element abundance	10
1.5	Dust continuum mosaic of the ρ Oph cloud	13
1.6	Cooling processes in protostellar clouds	15
1.7	Magnetic field gradients and ambipolar diffusion	16
1.8	Spectral energy distributions of young stellar objects	17
1.9	Pulsed jet from an embedded protostar	18
1.10	Circumstellar disks around young stars	19
1.11	Theoretical evolutionary tracks for pre-main-sequence stars	20
1.12	Schematic picture of stellar accretion processes	22
1.13	A gallery of circumstellar disks	25
1.14	Simulated fractal dust aggregate	28
1.15	Sequence of events of solid planet formation	29
2.1	Technical overview of the <i>Hubble Space Telescope</i>	32
3.1	Example for cosmic ray removal	38
3.2	Schematic representation of the drizzle algorithm	39
3.3	Enhancement of spatial resolution by PSF deconvolution	41
3.4	Representation of the effects of image deconvolution	42
3.5	Multi-wavelength images of 114-426	47
3.6	Intensity profiles along major axis of 114-426	48
3.7	Multi-wavelength images of 218-354	49
3.8	Intensity profiles along major axis of 218-354	49
3.9	Multi-wavelengths images of 183-405	50
3.10	Intensity profiles along major axis of 183-405	50
3.11	Multi-wavelengths images of 182-413	51
3.12	Intensity profiles along major axis of 182-413	51
3.13	Multi-wavelengths images of 167-231	52
3.14	Intensity profiles along major axis of 167-231	52
4.1	Disk size distributions	56
4.2	Kolmogorov-Smirnov test for disk size distributions	58
4.3	Projected separation from θ^1 Ori C vs. disk diameter	59

4.4 Wavelength-dependence of disk size 60

List of Tables

1.1	Orbital parameters and physical characteristics of the planets	4
1.2	Radioactive decays used for radioisotope dating	11
1.3	Characteristic values of specific angular momentum	21
2.1	Characteristics of the WFPC2 cameras	33
2.2	Detector specifications for the STIS instrument	34
2.3	Basic imaging parameters of the NICMOS cameras	34
2.4	Set of filter elements used	35
3.1	HST observation programmes analysed	37
3.2	Catalogue of disks seen in silhouette	43
3.3	Catalogue of ionised disks	44
3.4	Diameters of silhouette and ionised disks	46